

9-13-2019

## Decoding Geometric Origin of Geomechanical Properties

Sumana Bhattacharya

Florida International University, sbhat014@fiu.edu

Follow this and additional works at: <https://digitalcommons.fiu.edu/etd>



Part of the [Geotechnical Engineering Commons](#)

---

### Recommended Citation

Bhattacharya, Sumana, "Decoding Geometric Origin of Geomechanical Properties" (2019). *FIU Electronic Theses and Dissertations*. 4295.

<https://digitalcommons.fiu.edu/etd/4295>

This work is brought to you for free and open access by the University Graduate School at FIU Digital Commons. It has been accepted for inclusion in FIU Electronic Theses and Dissertations by an authorized administrator of FIU Digital Commons. For more information, please contact [dcc@fiu.edu](mailto:dcc@fiu.edu).

FLORIDA INTERNATIONAL UNIVERSITY

Miami, Florida

DECODING GEOMETRIC ORIGIN OF GEOMECHANICAL PROPERTIES

A dissertation submitted in partial fulfillment of the  
requirements for the degree of

DOCTOR OF PHILOSOPHY

in

CIVIL ENGINEERING

by

Sumana Bhattacharya

2019

To: Dean John L. Volakis  
College of Engineering and Computing

This dissertation, written by Sumana Bhattacharya, and entitled Decoding Geometric Origin of Geomechanical Properties, having been approved in respect to style and intellectual content, is referred to you for judgement.

We have read this dissertation and recommend that it be approved.

---

Abdelhamid Meziani

---

Hector R. Fuentes

---

Atorod Azizinamini

---

Seung Jae Lee, Major Professor

Date of Defense: September 13, 2019

The dissertation of Sumana Bhattacharya is approved.

---

Dean John L. Volakis  
College of Engineering and Computing

---

Andres G. Gil  
Vice President for Research and Economic Development  
and Dean of the University Graduate School

Florida International University, 2019

## ACKNOWLEDGMENT

I thank my dissertation advisor Dr. Seung Jae Lee for guiding me throughout the journey and introducing me to the world of cutting-edge research in geomechanics. I thank him for his generous support during various phases of this work and for inspiring me to reach my full potential.

I am thankful to Dr. Hector R. Fuentes, Dr. Abdelhamid Meziani and Dr. Atorod Azizinamini for their time and generous support to serve in my dissertation committee. I thank Dr. Hector R. Fuentes for always encouraging and motivating me, and for taking time to carefully review my dissertation to provide extremely valuable feedback for improvement. I thank Dr. Abdelhamid Meziani for his encouragement and constructive feedback. I am thankful for the generosity of Dr. Atorod Azizinamini and FIU department of Civil and Environmental Engineering for motivating me and providing support in various forms.

I thank Mr. Yu-Feng Su for inspiring and motivating me with his work. I also thank various mentors and collaborators with whom I had the auspicious opportunity to work with: Profs. Moochul Shin and Chang Hoon Lee at Western New England University, Mr. Sudip Subedi and Dr. Nipesh Pradhananga at Moss School of Construction, Infrastructure and Sustainability at FIU, Mr. Julian Ramirez from Robotics and Digital Fabrication (RDF) lab at FIU Department of Architecture, Mr. Michael Kim at Florida Department of Transportation. I deeply acknowledge their support and generosity. It was an honor working with them.

I acknowledge the support of University Graduate School at FIU in the form of Dissertation Year Fellowship (DYF) award.

I thank my dear friend Dr. Sumanta Das at University of Rhode Island who is a guide to me for a very long time. I thank Brahma Kumari meditation center in Miami for providing me critical support and teaching me spirituality during moments of personal crisis. Lastly and most importantly, I thank all my dear friends whom I met along the journey and created unforgettable memories with. They have been a huge support system for me, and I could not have done this without them.

## ABSTRACT OF THE DISSERTATION

### DECODING GEOMETRIC ORIGIN OF GEOMECHANICAL PROPERTIES

by

Sumana Bhattacharya

Florida International University, 2019

Miami, Florida

Professor Seung Jae Lee, Major Professor

Granular materials such as soil and aggregate, are ubiquitous in nature and the understanding of their mechanical behavior is of great importance to better predict and design the civil infrastructure. The particle geometry is a key information to robustly establish the link between the underlying grain-scale mechanisms and the macroscopic behavior of granular materials. However, the characteristics of the particle geometry remain to be better understood. For example, we do not know how the volume is related to the surface area for irregularly shaped particles in general. Their relation clearly depends on the morphology, dictating that volume, surface area, and morphology are interrelated. Then, the remaining question is how the size of a particle would be related to those three geometric properties. The interrelation of these four geometry parameters is the key information to fundamentally understand their concerted influence on the complex behavior of granular materials, but we do not have the answer in the body of knowledge yet.

The research in this dissertation advances the understanding of grain-scale origin of the complex macroscale behavior of granular materials and creates a set of new knowledge as follows: (i) This study systematically addresses the influence of coarse aggregate

angularity on cemented granular materials. It shows that cemented granular materials with round aggregates have superior small-strain performance, while the materials with angular aggregates have superior large-strain performance; (ii) This study develops a new theory for comprehensive 3D particle geometry characterization by proposing a formulation  $M = A/V \times L/6$ , which translates the 3D particle morphology  $M$  as a function of surface area  $A$ , volume  $V$ , and size  $L$ ; (iii) This dissertation is benefited by the early adoption of 3D-printing for geomechanical testing. Laboratory direct shear tests have been conducted on 3D-printed synthetic particles with different geometry, to robustly correlate the geometric properties of particles to geomechanical properties of the granular materials. (iv) This study unravels, for the first time, the power law relationship between  $A/V$  ratio and  $V$  for coarse aggregate in nature. This relationship is the key to predict morphology using volume measurement only, thus significantly reducing the effort of particle geometry characterization.

## TABLE OF CONTENTS

CHAPTER	PAGE
1 INTRODUCTION .....	1
1.1 Granular Materials and Multiscale Mechanics.....	1
1.2 Importance of Particle Morphology in Multiscale Mechanics.....	3
1.3 Existing Methods of Particle Morphology Characterization and Measurement ...	5
1.4 Research Objective and Scope .....	8
1.5 Overview .....	9
2 INFLUENCE OF COARSE AGGREGATE ANGULARITY ON THE MECHANICAL PERFORMANCE OF CEMENT-BASED MATERIALS .....	12
2.1 Introduction .....	12
2.1.1 Background .....	12
2.1.2 Objective and Scope .....	15
2.2 Hypothesized Morphology-driven Particle Scale Mechanisms .....	17
2.3 Aggregate Morphology Characterization.....	20
2.3.1 Preparation of Coarse Aggregate Samples .....	21
2.3.2 Characterization of Global Form and Local Angularity .....	21
2.3.3 Characterization of Surface Texture .....	26
2.4 Investigation of morphology effect on mechanical properties.....	27
2.4.1 Experimental Procedure.....	27
2.4.2 Test Results and Discussion.....	29
2.5 Concluding Remarks .....	34
3 A NEW INTERPRETATION OF THREE-DIMENSIONAL PARTICLE GEOMETRY: M-A-V-L .....	37
3.1 Introduction .....	37
3.1.1 Background.....	37
3.1.2 Objective and Scope .....	40
3.2 Proposed Formula for the New Interpretation.....	44



3.3	Four-Dimensional Aspects in the 3D Geometry Parameter Distributions .....	48
3.3.1	M-A-V-L Approach for Comprehensive Description of the Parameter Distributions.....	48
3.3.2	Power Law Relation between A/V and V .....	57
3.4	Experimental Demonstration of Predictive Capability .....	59
3.4.1	Specimen Preparation for Laboratory Direct Shear Test .....	59
3.4.2	Test Results and Discussions .....	63
3.5	Concluding Remarks .....	67
4	A NEW FRAMEWORK TO ESTIMATE THE COARSE AGGREGATE 3D GEOMETRY USING OPTICAL GEO-CHARACTERIZATION .....	69
4.1	Introduction .....	69
4.1.1	Background .....	69
4.1.2	Objective and Scope .....	72
4.2	Particle Sampling and Scanning using SL scanner .....	73
4.2.1	Particle Sampling .....	73
4.2.2	SL Scanning .....	74
4.3	Scanning Particles using Photogrammetry.....	77
4.4	Measurement of the Geometric Properties from the Reconstructed 3D Particles .....	79
4.5	Comparison of Power Law Functions Obtained from the 2 Scanning Techniques .....	81
4.6	Validation of Power Law from SL Scanning and from Photogrammetry.....	82
4.7	Concluding Remarks .....	86
5	PREDICTION OF 3D SPHERICITY WITH VOLUME ONLY .....	88
5.1	Introduction .....	88
5.1.1	Background.....	88
5.1.2	Objective and scope .....	89
5.2	Power Law Relation between A/V and V .....	90
5.3	Demonstration of the 3D Sphericity Prediction using the Volume Only.....	91
5.3.1	Sampling of Florida Limestone Particles.....	92

5.3.2	3D Scanning of the Sampled Particles .....	92
5.3.3	Characterization of the Power Law Relation between A/V and V .....	93
5.3.4	Rapid Characterization of the Shape Distribution in terms of the 3D Sphericity .....	96
5.4	Concluding Remarks .....	98
6	CONCLUDING REMARKS AND RECOMMENDATION FOR FUTURE WORK .....	99
6.1	Concluding Remarks .....	99
6.2	Recommendation for Future Work .....	101
	REFERENCES .....	103
	APPENDICES .....	119
	VITA.....	151

## LIST OF TABLES

TABLE	PAGE
Table 2.1. Influence of aggregate angularity on the mechanical performance of concrete (Partly adapted from [63]), where $f_t$ is tensile strength, $E_t$ is elastic modulus in tension, $f_{peak}$ is compressive strength, $E_c$ is elastic modulus in compression (otherwise noted). .....	14
Table 2.2. Mixture proportion (per m <sup>3</sup> mortar) (courtesy of Drs. Chang Hoon Lee and Moochul Shin at WNEU).....	28
Table 3.1. Ranges of void ratio for each specimen and the relative densities $D_r$ for the void ratio $e = 0.73$ .....	63
Table 4.1. Validation of power law equations using SL scan of 8 additionally sampled particles. ....	85
Table 5.1. True sphericity of additionally sampled 8 particles obtained by (a) 3D structured light scanning and (b) using the $V$ values indirectly estimated first with the measured particle weights, then the corresponding $A/V$ ratios found from the power function. ....	96

## LIST OF FIGURES

FIGURE	PAGE
Figure 1.1. Multiscale nature of granular materials [4]. .....	3
Figure 1.2. Conventional morphology characterization at three different scales [58]......	8
Figure 2.1. The surface-area-to-volume ratio depending on the particle morphology. ....	18
Figure 2.2. The influence of particle morphology on the formation of ‘weak’ interphase region. ....	19
Figure 2.3. Two different sets of aggregate used in this study. ....	21
Figure 2.4. Five-step image analysis procedure.....	24
Figure 2.5. Morphology of crushed and river aggregates, where the distributions are statistically represented by the bivariate ellipses (courtesy of Drs. Chang Hoon Lee and Moochul Shin at WNEU). ....	25
Figure 2.6. Water droplet test result – Image of droplets on (a) river and (b) crushed aggregates, where the outline of a droplet on a river aggregate is overlapped for optical comparison (courtesy of Drs. Chang Hoon Lee and Moochul Shin at WNEU). ....	27
Figure 2.7. Test setups: (a) Splitting tensile strength test, (b) Monotonic compression test, (c) Cyclic compression test. (courtesy of Drs. Chang Hoon Lee and Moochul Shin at WNEU). ....	29
Figure 2.8. The splitting tensile strength of the tested 10 cylinders with respect to test ages (courtesy of Drs. Chang Hoon Lee and Moochul Shin at WNEU). ....	30

Figure 2.9. The compressive strengths of the tested 10 cylinders with test ages (courtesy of Drs. Chang Hoon Lee and Moochul Shin at WNEU). .....	31
Figure 2.10. The modulus of elasticity of the tested cylinders at Days 14 and 28 (courtesy of Drs. Chang Hoon Lee and Moochul Shin at WNEU). .....	32
Figure 2.11. Responses under cyclic loading at 28 days; (a) Stress-strain curve of cylinders with crushed particles (CR) and river particles (RI); and (b) the curves ‘normalized’ by the peak compressive strength ( $f_{peak}$ ) (courtesy of Drs. Chang Hoon Lee and Moochul Shin at WNEU). .....	34
Figure 3.1. Interrelated 3D particle geometry parameters; (a) Two different particle morphology with the same size; (b) Two different particle morphology with the same volume; (c) Two different particles with same morphology having different volumes, surface areas and sizes. ....	38
Figure 3.2. Separate description of particle size and morphology distributions. ....	43
Figure 3.3. Morphology related to surface-area-to-volume (A/V) ratio. ....	45
Figure 3.4. 3D morphology (M) translated as $A/V \times L/6$ . ....	46
Figure 3.5. Particle models of mixed morphology group evaluated with Sphericity, Roundness, and proposed M values. The size L is shown next to M. The particle in the green circle is selected as a sample particle for the demonstration of interrelated of geometry parameters (See Figure 3.7). ....	52
Figure 3.6. Particle models of near-sphere group evaluated with Sphericity, Roundness, and proposed M values. The size L is also presented next to M. ....	53

Figure 3.7. Description of the distributions of the ‘interrelated’ particle geometry parameters, where the parameter values of the sample particle (selected in Figure 3.5) are marked with green circle symbols; (a) Morphology distribution using conventional Sphericity and Roundness; (b) Particle size distributions for mixed morphology and near-sphere groups evaluated in terms of particle number and volume, respectively; (c) Combined description of M and size L; (d) Combined description of A/V ratio and V; (e) Distributions of A/V ratios evaluated in terms of particle number and volume, respectively; (f) Distributions of M by volume..... 54

Figure 3.8. Development of 3D particle models and 3D printed particles; (a) Representative 2D morphology of typical mineral particles evaluated in terms of Sphericity and Roundness, modified from Krumbein and Sloss [111]; (b) Developed 3D particle models, and the quantified morphology and the inverse of Regularity; (c) 3D printed particles of the four models; (d) Direct shear test setup. .... 61

Figure 3.9. Evaluated geometry parameters for the four particle specimens; (a) Description of morphology and size using M and L as well as  $1/\rho$  and L; (b) Description of A/V ratio and V..... 63

Figure 3.10. Direct shear test result: stress-strain curves and vertical displacements obtained at four different normal stresses (40.5, 102.5, 164.4, and 226.4 kPa); where the stress-strain curve in (a) to (d) is normalized by  $\tau_{max}^*$ , maximum shear stress obtained from the specimen 4-1..... 66

Figure 3.11. Friction angles evaluated from the fitting lines of shear strengths..... 67

Figure 3.12. Dilation angles evaluated at the peak strength state. .... 67

Figure 4.1. 60 particles used in SL scanning. .... 74

Figure 4.2. HP SL Scanner Setup. ....	76
Figure 4.3. Scanning a regular shaped object in order to validate the dimensional proportionality: a) the ball mounted on the turntable by a needle arrangement; and b) scanned 3D-model of the ball. ....	77
Figure 4.4. 3D imaging and photogrammetry reconstruction of a particle: (a) Particle sitting on the arrangement of 4 needles; (b) 240 photos taken around the particle; (c) Sparse reconstruction; (d) Dense reconstruction; (e) Generated 3D particle geometry. ..	79
Figure 4.5. 60 particles 3D models scanned using SL 3D scanner. ....	80
Figure 4.6. Reconstructed 3D particle geometry based on 240 photos each using photogrammetry method. ....	81
Figure 4.7. (a) $V$ vs. $A/V$ plot for 60 particles scanned using SL scanning method and for 30 particles scanned using photogrammetry method; (b) $M$ vs $L$ plot for 60 particles scanned using SL scan and 30 particles scanned using photogrammetry. ....	82
Figure 4.8. A set of 8 additionally sampled particles for validation of the power law relation between $A/V$ and $V$ of the Florida limestone aggregate: (a) Photo of the 8 particles; (b) Digitalized 3D particles obtained from the structured light scanning. ....	84
Figure 4.9. Validation of power law equation using 8 additionally sampled particles: (a) $V$ vs $A/V$ data obtained from SL scanning plotted along with power law functions obtained in SL scan sampling and photogrammetry sampling; (b) plot of $M$ vs. $L$ . ....	85

Figure 5.1. V vs A/V relationship for 60 sampled limestone particles (black squares); power law fit equation for the sampled particles; additionally sampled 8 particles (red circle); predicted A/V values using weight superimposed on the power law equation (yellow cross).....	94
Figure 5.2. Measurement of particle weight. ....	95
Figure 5.3. A total of 344 particles used to predict the 3D Sphericity distribution of the Florida limestone aggregate. ....	97
Figure 5.4. The 3D Sphericity distribution of the aggregate particles evaluated by both particle number and volume. ....	97



## LIST OF SYMBOLS

$E_c$	modulus of elasticity of concrete in compression
$f'_c$	compressive strength of concrete
$f_t$	tensile strength of concrete
$E_t$	modulus of elasticity of concrete in tension
$f_{peak}$	peak compressive strength
V	volume
A	surface area
L	size
M	morphology
$A_s$	surface area of a sphere
$V_s$	volume of a sphere
$L_s$	size of a sphere
$\rho$	regularity
$\alpha$	index for morphological heterogeneity
$\beta$	index for representative morphology
$\psi$	'true' sphericity
$\lambda$	a geometry constant
$I_{sph}$	sphericity index
$V_{sph}$	volume of a sphere
e	void ratio
$e_{max}$	maximum void ratio
$e_{min}$	minimum void ratio

$D_r$	relative density
$\delta_h$	horizontal displacement
$\delta_v$	vertical displacement
$\tau$	shear stress
$\tau_{\max}$	maximum shear stress
$\sigma_n$	normal stress

## ABBREVIATIONS AND ACRONYMS

2D	Two Dimensional
3D	Three Dimensional
A/V	Surface area to volume ratio
ACI	American Concrete Institute
ASTM	American Society of Testing and Materials
CBM	Cement-based Materials
CR	Crushed Aggregates
DEM	Discrete Element Method
DLP	Digital Light Processing
F&E	Flat and Elongated
FEM	Finite Element Method
FIU	Florida International University
ITZ	Interface Transition Zone
KN	Kilo Newton
M-A-V-L	Morphology-Surface Area-Volume-Size
MB	Mega Byte
MP	Mega Pixel
MPa	Mega Pascal
PCD	Pixels per Circumscribed Circle Diameter
RI	River Aggregates
SFM	Structure from Motion
SL	Structured Light

SLA	Stereolithography
W/C	Water Cement Ratio
WNEU	Western New England University
XRCT	X-Ray Computed Tomography

## AUTHOR CONTRIBUTION

This dissertation is prepared in accordance with the regulation for Electronic Thesis and Dissertation (ETD) Preparation Manual by University Graduate School of Florida International University. Below is the statement of co-authorship of individual chapters:

### Chapter 2: Influence of Coarse Aggregate Angularity on the Mechanical Performance of Cement-based Materials

Image analysis was performed by Sumana Bhattacharya. Experiments were performed by Dr. Moochul Shin and Dr. Chang Hoon Lee at Western New England University. Hypothesis development, result analysis and draft preparation were performed by Dr. Seung Jae Lee, Sumana Bhattacharya, Dr. Moochul Shin and Dr. Chang Hoon Lee

### Chapter 3: A New Interpretation of Three-Dimensional Particle Geometry: M-A-V-L

Numerical modeling of all particles was performed by Sumana Bhattacharya. 3D-printing of particles was performed by Sumana Bhattacharya and Zoubair Douite. Experiments were conducted by Sumana Bhattacharya and Yu-Feng Su. Concept development, result analysis and draft preparation were performed by Sumana Bhattacharya under supervision of Dr. Seung Jae Lee.

### Chapter 4: A New Framework to Estimate the Coarse Aggregate 3D Geometry using Optical Geo-Characterization

Particle Structured Light scanning was performed by Sumana Bhattacharya and Sudip Subedi. Particle photogrammetry scanning was performed by Sumana Bhattacharya. Result analysis and draft preparation were performed by Sumana Bhattacharya under supervision of Dr. Seung Jae Lee.

## Chapter 5: Prediction of 3D Geometry using Volume Only

Particle SL scanning was performed by Sumana Bhattacharya and Sudip Subedi. Sphericity distribution was performed by Sumana Bhattacharya. Result analysis and draft preparation were performed by Sumana Bhattacharya under supervision of Dr. Seung Jae Lee.

# 1 INTRODUCTION

## 1.1 Granular Materials and Multiscale Mechanics

Granular materials are widely encountered in various forms in nature. They have a vast range of engineering, commercial and industrial applications. They are known as the second-most manipulated material in industry after water [1]. Soil, aggregate, snow, bulk food, tree leaves, chemical powder, pharmaceutical pills, lego blocks are all granular in nature. They are ideally materials consisting of discrete particulate bodies and possess a unique behavior different from any known type of material. Their constituent particles are solid rigid bodies, but the particles together can flow as complex fluids (e.g. avalanches) [2]. They possess both solid and liquid like behaviors but at different scales. At field-scale they act as continuous material, but at grain-scale they behave as discontinuous material (Figure 1.1). The complex macroscopic behavior at the field-scale is attributed to their discrete nature at the grain-scale. Hence to obtain a complete understanding of granular material behavior, it is critical to study their behavior at different scales.

Granular material field-scale behavior is a function of their grain-scale structure. Multiscale mechanics is the study of the relationship between the field-scale behavior and the grain-scale structure. Multiscale mechanics of granular materials is not completely understood as there is no standard framework or theory that suitably describes the transition of behavior from scale-to-scale i.e. how the parameters at each scale are linked. The fundamental understanding of granular material behavior is of extreme importance in areas such as civil, construction, aerospace, chemical, pharmaceutical, food processing engineering etc. Continuum-based approach such as finite element method (FEM) has been popularly adopted in engineering practices due to its detailed capturing of macroscale

phenomena. But continuum-based approach fails to give information at grain-scale where grain-to-grain interaction occurs. Since its inception in 1979, discrete element method (DEM) has gained extreme popularity in grain-scale simulation of granular materials [3]. Soil, which is a major parameter of consideration in civil engineering, is granular in nature. Although FEM captures field-scale behaviors such as settlement of foundation on soil, it fails to capture phenomena where soil grains detach from each other such as landslide, soil excavation or earth digging. The understanding of the discrete nature of soil is of utmost importance in accurate prediction of soil behavior in case of earthquake, liquefaction or landslide.

Multiscale mechanics of granular materials finds the link in geometric and mechanical properties across scales. Since the basic building block of granular materials is grain, a detailed understanding of grain properties will greatly facilitate correlation of properties across scales. The first step towards understanding this multiscale behavior is to understand the parameters that control each scale. At grain-scale, particle morphology (i.e. shape) and size are two of the most important parameters related to particle geometry that control how the grains interact among each other. Soil and rock are geologic materials which are used as cemented and uncemented materials in construction. Cemented material is concrete, pavements (flexible and rigid) etc. Uncemented material is soil, railway ballast etc. Macroscale properties of concrete include strength (compressive, tensile and flexural), abrasion resistance, creep, fire resistance, durability, workability, toughness, permeability etc. Macroscale properties of soil are bearing capacity, shear strength, slope stability, lateral earth pressure, consolidation, permeability and seepage, etc. Multiscale mechanics



is the relation between inter-scale properties such as grain-scale morphology properties and macro-scale mechanical properties.

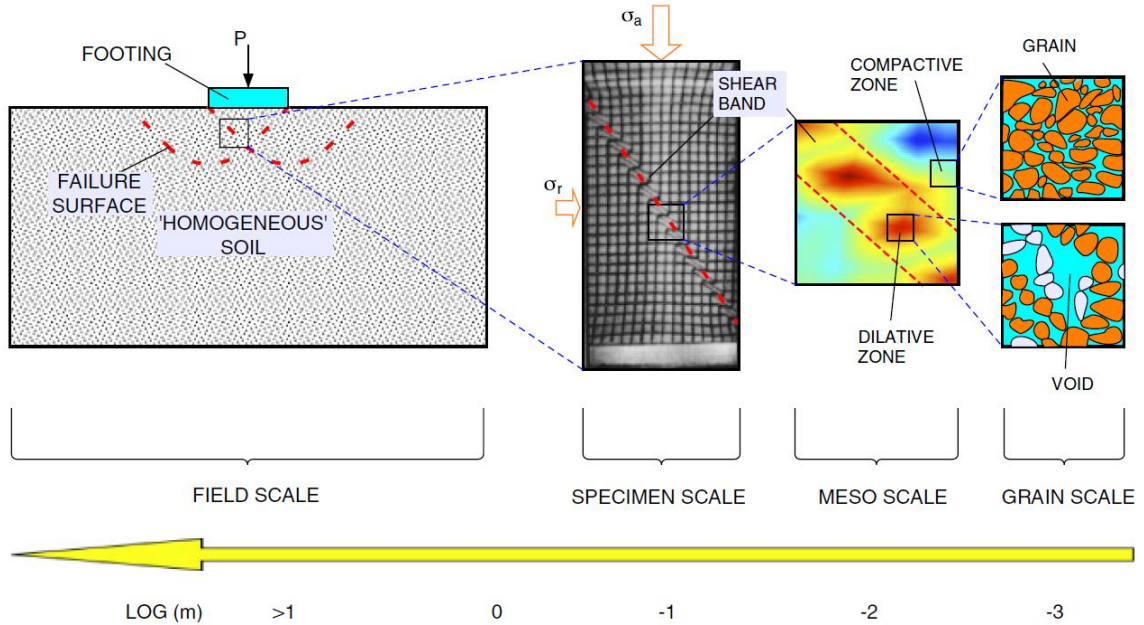


Figure 1.1. Multiscale nature of granular materials [4].

## 1.2 Importance of Particle Morphology in Multiscale Mechanics

Particle 3D morphology is one of the most important grain-scale properties of aggregate that influence its macroscale behavior. Particle morphology directly controls how two grains interact. In soil mechanics, the force carried by soil is transferred from grain to grain through interparticle contact points. Particle morphology determines the number of contact points in a soil assembly as well as the contact network. It also controls particle interlocking mechanism which controls its load bearing capacity. Numerous studies have investigated the importance particle morphology plays on macroscale properties such as aggregate maximum and minimum void ratio, peak shear strength, critical shear strength, dilation, particle breakage, stiffness [5–10].

Construction aggregates are indispensable part of civil engineering. Bound coarse aggregates are used in highway or airport pavement materials and as the main constituent of concrete. Unbound aggregates are used as railway ballast materials. Railway tracks are high in demand as convenient and economic mode of transportation [11]. Ballast aggregates are one of the most important components of a railway track. Regular wear and tear from railway load make the ballast particle undergo breakage and chipping which alter its gradation. This change in grain-scale morphology distribution changes the properties of ballast in macroscale and requires replacement [12,13]. It is necessary to regularly inspect the ballast material quality to avoid ununiform settlement or train derailment.

The influence of particle morphology on the mechanical performance, particularly on the strengths, of cement-based materials (CBM) has been broadly investigated. The use of flat and elongated particles in concrete has been evidenced to negatively impact the strengths [14–16], which led to the development of guidelines and specifications suggesting to limit the use of flat and elongated particles up to 10~15 percent of the total amount [17–19]. Existing studies generally agree that higher peak strengths are obtained by using more angular particles [20–26]. The rough-textured aggregates have also been observed to enhance the overall material performance including higher strengths [14,27] and higher ductility [28,29] than smooth-textured aggregates. The micro-irregularities of surface texture can also accelerate the rate of hydration as providing nuclei for precipitation of hydrated products [30,31]. The rutting susceptibility in asphalt concrete is known to decrease with the roughness of surface texture [32].

### 1.3 Existing Methods of Particle Morphology Characterization and Measurement

In early days, sedimentologists were the first to develop interest in particle morphology as it revealed important information about particle mineralogy and mode of sediment transport [33–37]. For practical applications, civil engineers were primarily concerned with particle size distribution [38]. Particle size has been measured either quickly by sieve analysis or by linear measurement devices such as ruler or caliper. On the other hand, the morphology has been traditionally characterized using three factors defined at three different scales [39]: (i) global form (at particle diameter scale), (ii) local angularity (at intermediate scale typically one-tenth of particle diameter), and (iii) surface texture (at small microscopic scale) as shown in Figure 1.2. The global form provides the largest scale morphological information related to the particle's diameter scale  $O(d)$  and characterizes the extent to how equidimensional the particle morphology is (e.g. sphere vs. ellipsoid). The local angularity describes the overall sharpness of corners defined at a smaller length scale by one order of magnitude  $O(d/10)$  [9]. On the other hand, the surface texture is defined at the smallest morphology scale related to roughness.

Several measurable indices have been developed in the past to describe global form and local angularity. Sphericity and Roundness [40] are the oldest and broadly adopted descriptors to optically characterize the global form and the local angularity [41,42]. Both Sphericity and Roundness range between 0 and 1. A low Sphericity indicates an elongated shape such as an ellipsoid, while a high Sphericity close to 1 indicates a near-equidimensional shape such as a sphere; a low Roundness close to 0 indicates a particle with sharp corners, while a high Roundness indicates the opposite. In addition, Regularity  $\rho$  was defined as the arithmetic average of Sphericity and Roundness [6], which can be

leveraged to comprehensively describe the global form and the local angularity. Compared to the global form and the local angularity that have been optically characterized using Sphericity and Roundness, the effect of surface texture has been mechanically characterized and modeled in terms of the inter-particle friction angle [43–45] in the discrete element analysis [46,47].

Although there are several modified or simplified definitions of Sphericity, the original definition which is termed as ‘true’ sphericity is the ratio of surface area of a sphere with the same volume of the particle to the surface area of the particle [37]. Due to difficulty in measuring the 3D surface area associated with this formula, several simplified 2D formulas were developed considering the largest face of the particles. For large particles, the 2D projections were captured by camera lucid method or taking photographs and surface areas were measured using planimeters. The difficulty and time associated with measuring these morphology indices often made their practical use inconvenient. For this reason, field engineers often characterized particles qualitatively with visual morphology chart. Qualitative characterization included categorization of particles in groups such as elongated, flat, spherical, angular, rounded, sub-rounded etc. Boggs used electronic particle size analyzer on sand sized particles to measure Sphericity and Roundness which was not possible before for small size particles due to limitation in instrumentation [37].

With the recent advancement of optical geo-characterization and the need of quantitative morphology assessment, the digital cameras and image processing algorithms have been adopted for computation of the morphology indices [48]. Digital image processing made it easier to capture 2D images of particles and process those images to obtain various parameters such as size, perimeter, surface area [49]. Many 2D shapes indices have since

been developed such as flat and elongated (F&E) ratio, angularity index, shape factor, angularity factor etc. based on geometric parameters easily retrieved from the 2D images [50,51]. However, the computation requires some considerable time at the moment even for the 2D morphology analysis with the necessity to sample, scan, and analyze as many aggregate particles as possible to enhance the statistical reliability of characterized morphology. More recently, the dynamic image analysis equipment has been developed for a fast 2D morphology analysis, but which has limitations in the particle size that can be captured [52–54].

Sophisticated 3D particle morphology analysis takes even longer and computationally more expensive. For example, X-Ray Computed Tomography (XRCT) scanning enabled to capture the voxel-based 3D particle geometry and subsequent mesh reconstruction to extract the morphology information [55,56]. Therefore, some significant time is required for the image processing including the 3D particle segmentation, so XRCT has been selectively used to capture the granular skeletal structure such as fabric. Furthermore, XRCT scanning is not affordable for the morphology analysis of a large number of aggregates. A promising alternative to capture the 3D particle geometry is to use portable imaging equipment such as affordable digital camera, for which the photogrammetry technique can be used to develop the 3D models of the individually scanned particles and analyze the 3D morphology [57]. However, this approach can be only applied for coarse aggregates, e.g., track ballast, due to the limited resolution of camera, and requires an extensive number of photos taken to develop accurate 3D particle model. While sampling as many particles as possible is needed for robust morphology characterization of the given

aggregate, the 3D imaging task is labor-intensive, thus only limited number of particles could have been analyzed.

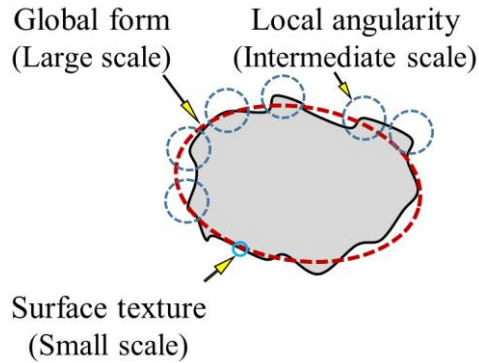


Figure 1.2. Conventional morphology characterization at three different scales [58].

#### 1.4 Research Objective and Scope

The objective of this dissertation is to advance towards better understanding of multiscale mechanics of granular material. The goal of multiscale mechanics is the systematic correlation between grain-scale geometric properties with macroscale mechanical properties. This essentially means identification of key parameters at each scale and thereafter, systematic and robust correlation of these parameters. The objective of this dissertation is to identify grain-scale 3D geometric parameters and provide a new robust 3D characterization index for granular particles having more accurate correlation with macroscale properties compared to existing indices, which at the same time can be readily and easily implemented in practice. Next it aims to validate the seamless correlation of this grain-scale index to macroscale mechanical property. Direct shear strength is selected as the macroscale property for the scope of this dissertation. Finally, the dissertation provides a convenient technique to measure grain-scale 3D morphology parameters in a quick and efficient manner.

Lack of affordable and easily implementable 3D characterization and measurement techniques significantly hinders the systematic consideration of particle morphology in construction industry and in constitutive modeling. This research shows how the surface-area-to-volume-ratio concept was first conceived from cemented granular material behavior. Then this concept is expanded to encompass granular material in general. Finally, it shows easy and accurate practical application. The broad objectives of this dissertation are listed below:

- 1) Investigation and understanding of the fundamental mechanism by which coarse aggregate angularity influences macroscale strength behavior of cemented granular material.
- 2) Development of a suitable morphology index that can robustly describe the interrelation of different geometry components of particles.
- 3) Experimental validation of the accuracy of macroscale predictive capability of this morphology index.
- 4) Demonstration of practical measurement technique of particle 3D geometry parameters quickly and efficiently for a large number of particles.
- 5) Development of practical method to quickly determine particle 3D ‘true’ Sphericity distribution of aggregate group.

## 1.5 Overview

This dissertation is broadly composed of three inter-related parts: 1) morphology characterization; 2) correlation with macroscale mechanical properties; 3) practical measurement technique. This dissertation starts with understanding key morphology components that influence the behavior of cemented granular materials. Building on that

concept, a new characterization index has been developed. The accuracy of the predictive capability of this index has been experimentally validated using direct shear test on 3D-printed particles. Finally, this dissertation provides efficient and practical method to quickly measure particle geometry properties.

Chapter 2 identifies the morphology components that influence the behavior of cemented granular material. It relates particle morphology to surface-area-to-volume-ratio. Spherical particles have lower surface-area-to-volume-ratio while angular particles have higher surface-area-to-volume-ratio. Cemented granular material is composed mainly of three phases: aggregates, binding matrix and the interphase regions commonly known as ‘weak links’ that initiate crack development and propagation. Due to high surface-area-to-volume-ratio in angular particles, cemented granular materials with angular particles have more ‘weak links’. These ‘weak links’ initially reduce the compressive strength by forming microcracks. But at high deformation, the microcracks and particle high angularity together contribute to increase interlocking mechanism, which is manifested as the higher peak strength in cemented granular material with angular coarse aggregate. To experimentally corroborate these mechanisms, two sets of aggregate batches, one angular and the other rounded, are collected and their morphology have been analyzed using 2D image analysis method. Cemented granular materials made from these two types of aggregates are subjected to cyclic compression tests to confirm the morphology-driven mechanisms.

Chapter 3 further investigates the influence of surface-area-to-volume ratio and develops a new characterization concept M-A-V-L where morphology is presented as  $M=(A/V \times L)/6$ . It also shows the inter-relation between different particle geometry components such as surface area (A), volume (V) and size (L). 200 geometric particles have been generated to



show how the geometric properties are inter-related. This study finds out that particle surface-area-to-volume-ratio and volume follow a power law relationship, which is an interesting behavior of particle geometric parameters. Next direct shear test on 3D-printed synthetic particles have been performed to corroborate the macroscale correlation property of M-A-V-L characterization.

In Chapter 4, a set of 60 Florida limestone particles have been 3D scanned using HP SL 3D scanner to compute their geometric properties. The purpose is to validate that the power law relationship between surface-area-to volume-ratio and volume also holds true for naturally occurring mineral particles as obtained theoretically. It also demonstrates the capability of the SL scanner to produce high quality scan models of different size particles. Then SL scanning results are compared with cost efficient and portable photogrammetry scan results. 30 particles out of the previously scanned 60 particles are scanned using photogrammetry method. The study compares the two power law equations obtained from each of the scanning techniques as well as the M values of the 30 particles. The validation of these power law functions across different particle sizes have been demonstrated by using additionally sampled 8 particles of different sizes.

In Chapter 5, the power law relationship between particle surface-area-to-volume-ratio and volume, is leveraged to predict Wadell's 'true' 3D Sphericity using particle volume only. The power law is obtained from the previously SL scanned 60 particles and volume is measured using particle weight. This study shows the quick prediction of 'true' sphericity distribution of an aggregate group consisting of 344 particles without actually 3D scanning them.

Finally, Chapter 6 concludes the dissertation giving recommendation for future work.

## 2 INFLUENCE OF COARSE AGGREGATE ANGULARITY ON THE MECHANICAL PERFORMANCE OF CEMENT-BASED MATERIALS

### 2.1 Introduction

#### 2.1.1 Background

Aggregate in cement-based materials (CBM) is not only one of the major components that occupies the largest volume (higher than 60%), but also a critical factor that determines the structural performance of CBM. Aggregate is the most economic component of concrete after water. Cement which is the most expensive component acts as a binding material to hold the aggregate skeleton in place. Compressive strength of aggregates ranges from 65 MPa to 270 MPa [59], while compressive strength of cement mortar is around 20 MPa [60]. Hence aggregates are primarily responsible for the compressive strength of concrete. For normal-strength concrete, the strength of aggregate is higher than the strength of cement, hence aggregate strength does not play as significant role as it plays for high strength concrete where cracks pass through aggregates [61]. Apart from strength of aggregate, particle morphology of aggregate is one of the two most important ‘particle scale’ factors along with the particle size.

While morphology influence has been generally accepted in the construction aggregate research, the influence of local angularity on the overall stress-strain response is still largely under debate in the research community. Researchers have often reported observations and conclusions not complementing one another. For example, Saouma et al. [20] reported both elastic modulus and strengths were significantly increased with the particle angularity. This

trend was consistently reflected in the ACI 318 codes [62] where the modulus of elasticity is estimated as proportional to the specified design compressive strength, e.g.  $E_c = 4700\sqrt{f'_c}$  for normal weight concrete. However, it is worthwhile to note that the empirical equation does not factor in the morphology effect nor the void formed by aggregates that affect mechanical properties of concrete. To the contrary, some of the literature [21–25] commonly observed the ‘opposite’ trend where the elastic modulus decreased while the strengths increased with higher morphological angularity (and vice versa, i.e., the elastic modulus increased using round aggregates). For example, Guinea et al. [21] showed the tensile and compressive strengths of crushed aggregate are higher than those of the round aggregate, while the elastic modulus of the crushed aggregate is lower than that of the round aggregate. On the other hand, Rocco and Elices [63] largely concluded there was no significant morphology effect despite some minor tendency in the measured properties. Table 2.1 summarizes the reported results from various studies.

Table 2.1. Influence of aggregate angularity on the mechanical performance of concrete (Partly adapted from [63]), where  $f_t$  is tensile strength,  $E_t$  is elastic modulus in tension,  $f_{peak}$  is compressive strength,  $E_c$  is elastic modulus in compression (otherwise noted).

Studies	Aggregate		$f_t$ (MPa)	$E_t$ (GPa)	$f_{peak}$ (MPa)	$E_c$ (GPa)
	Size (mm)	Morphology				
Saouma et al. [20]	38 (max)	R <sup>a</sup>	2.67	--	24.8	16.9 <sup>b</sup>
		C <sup>a</sup>	3.96	--	36.6	23.2 <sup>b</sup>
Guinea et al. [21]	5-7	R	3.93	--	63.8	39.8
		C	4.15	--	73.2	33.1
Li et al. [22]	5-40	R	1.80	24.6	39.9	43.9
		C	2.12	17.6	44.63	35.1
	5-150	R	1.58	43.1	27.53	36.4
		C	1.91	40.0	21.82	33.1
Giaccio and Zerbino [24]	19 (max)	R/TS/3 <sup>c</sup>	4.3	--	61.4	49.7
		R/TR/3 <sup>c</sup>	4.6	--	60.9	45.5
		C(G) <sup>d</sup> /TR/3	5.7	--	74.6	48.4
		C(Q) <sup>d</sup> /TR/3	5.0	--	79.4	38.8
	19 (max)	R/TS/5	2.8	--	29.6	46.4
		R/TR/5	3.2	--	31.0	43.0
		C(G) <sup>d</sup> /TR/5	3.8	--	30.1	39.1
		C(Q) <sup>d</sup> /TR/5	3.0	--	33.1	33.0
Donza et al. [25]	16 (max)	R(S) <sup>d</sup>	--	--	57.1 <sup>e</sup>	38.3 <sup>e</sup>
		C(G) <sup>d</sup>	--	--	64.7 <sup>e</sup>	35.4 <sup>e</sup>

Note:

- R: Round, C: Crushed
- Effective Young's modulus.
- R: Round, C: Crushed / TS: Texture Smooth, TR: Texture Rough / 3: Water/Cement ratio is 0.3, 5: Water/Cement ratio is 0.5
- (G) granite, (Q) Quartz, (S) siliceous
- Digitized the 28 days properties from the plots in [25]

While the existing studies provide great insight into the morphology effect, some limitations are found including: (a) the angularity was not quantified, but instead qualitatively characterized as crushed or round after eyeballing the aggregates, thereby it is unclear how the test results were influenced by the angularity; (b) morphology variables

were not systematically controlled. Fine and coarse aggregates are mixed together in the parametric studies that may have significant variance in the angularity of the aggregates; and (c) no further investigation has been made to understand why, in particular, the elastic modulus was ‘negatively’ influenced by the angularity.

### 2.1.2 Objective and Scope

The influence of angularity remains to be better understood to enhance the predictive capabilities in estimating the mechanical performance of CBM. This study aims to advance the understanding of the angularity effect and plug up the gap existing in the body of knowledge. This study focuses on the interaction of three key phases in the material, i.e., constituent particles, binding matrix, and interphase region that works as the load-transferring bridge between the constituent particles and the binding matrix. The particular emphasis is given to understand how the angularity affects the interaction of the three key phases, and consequently the macroscopic material behavior.

This study strategically focuses on the influence of coarse aggregate morphology. If both coarse and fine aggregates are considered in the study, the level of the parametric complexity would significantly increase in the control variables, resulting in the mixed morphology effects produced by both aggregates. Considering the particle surface area is a critical mediator to correlate the aggregate morphology with the mechanical behavior, and the surface area of fine aggregate could be incomparably larger than that of the coarse aggregate, the inclusion of fine aggregate may potentially interfere with systematic observation of the influence of the coarse aggregate. The influences of fine and coarse aggregates can be considerably different, and it is necessary to strategically focus the already complicated influence of coarse aggregate first. Furthermore, the morphology

characterization of fine aggregates is technologically challenging due to the small particle size and a large number of particles for reliable sampling. Only a few studies were able to characterize the shape of fine aggregates by using advanced image analysis systems such as a laser diffraction method, or X-ray computed tomography methods [64–66]. Therefore, coarse aggregate is only adopted to prepare the CBM specimens for the experimental testing, while factoring out the influence of fine aggregate morphology. However, the findings from this study can be extended for investigating the influence of fine aggregate morphology that is left for future study.

The following highlights the materials and the approach adopted in this study, and the major findings from the experimental investigation of the influence of coarse aggregate angularity:

- Two types of coarse aggregates, (a) river and (b) crushed aggregates with discernible morphology differences, are adopted. The influence of particle size distribution is excluded in the investigation by controlling the nominal size between 9.5 mm to 12.5 mm to focus on the morphology effect (Section 2.3.1).
- The morphological characteristic is systematically quantified in terms of the Sphericity and Roundness for measuring the global form and local angularity instead of qualitative description such as round or angular as often used in the existing studies (Section 2.3.2.1).
- An image-based characterization technique is leveraged to robustly quantify the morphology of each particle instead of eyeballing description that may be subjective depending on inspectors (Section 2.3.2.2).

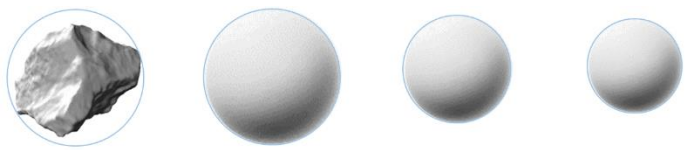
- The aggregate morphology is statistically defined on the sampled individual particle morphology (Section 2.3.2.3).
- A series of laboratory mechanical tests including cyclic compression test is performed on cylindrical specimens prepared with each type of the aggregate, and the overall CBM stress- strain response is obtained including the elastic modulus, the strengths, and the time-dependent transition of the mechanical properties (Section 2.4).
- The result shows the angularity negatively influences the small- strain performance, while positively impacts the mechanical property in the ultimate state at a large strain level.

## 2.2 Hypothesized Morphology-driven Particle Scale Mechanisms

Hypothesis #1: (More ‘weak links’ with the angularity). CBM is mainly composed of three phases: (a) aggregates that constitute the granular skeleton of CBM, (b) binding matrix that partially occupies the interstitial space, and (c) interphase region between the particles and the binding matrix. The interphase region substantially affects the overall performance of CBM, as it plays the critical role in the load-transferring mechanisms between particles and binding matrix. However, it is also susceptible to damage due to its weak mechanical properties [67,68]. Therefore, the interphase region commonly has been referred to as ‘weak links’ [14,69]. This study postulates that the aggregate angularity influences the formation of ‘weak links,’ and consequently the macroscopic mechanical behavior for the following reason.

The aggregate morphology is specifically related to aggregate’s surface-area-to-volume ratio, e.g., a sphere has the ‘smallest’ surface-area-to-volume ratio in all the geometric

shapes, and the ratio increases with the morphological angularity. For example, the surface-area-to-volume ratio of a cube is 1.24 times higher than that of a sphere given the same volume, while that of ‘more angular’ regular tetrahedron is 1.49 times higher than that of the sphere with the same volume. Figure 2.1 illustrates an example of a more realistic particle morphology (Figure 2.1a) shown with three spheres (Figure 2.1b, c, and d) that are differently scaled to match one of volume (V), surface area (A), or size (L) of the angular particle. Following interpretations can be made: (i) an angular particle has a higher A/V ratio compared to the sphere (round particle) of the same size (Figure 2.1b); (ii) the A/V ratio has a unit of inverse length, indicating that the A/V ratio depends on size. Therefore, the A/V ratio of the sphere increases (from 4 to 6 cm<sup>-1</sup>) with decrease in size (from 1.5 to 1.0 cm). However, if a particle is angular, the A/V ratio is still larger compared to a sphere given the same volume (Figure 2.1d).



	(a)	(b)	(c)	(d)
Volume (V):	0.53 cm <sup>3</sup>	1.77 cm <sup>3</sup>	0.71 cm <sup>3</sup>	0.53 cm <sup>3</sup>
Surface area (A):	3.86 cm <sup>2</sup>	7.07 cm <sup>2</sup>	3.86 cm <sup>2</sup>	3.17 cm <sup>2</sup>
Size (L):	†1.50 cm	1.50 cm	1.11 cm	1.00 cm
A/V:	<b>7.28 cm<sup>-1</sup></b>	4.00 cm <sup>-1</sup>	5.41 cm <sup>-1</sup>	6.00 cm <sup>-1</sup>

†Size in terms of circumsphere diameter

Figure 2.1. The surface-area-to-volume ratio depending on the particle morphology.

This fundamental concept between the surface-area-to-volume ratio and the morphology is the guiding principle hypothesizes that the angular aggregate inherently develops larger ‘weak’ inter- phase region along the aggregate surface due to the larger surface- area-to-volume ratio. Figure 2.2 schematically shows the concept.



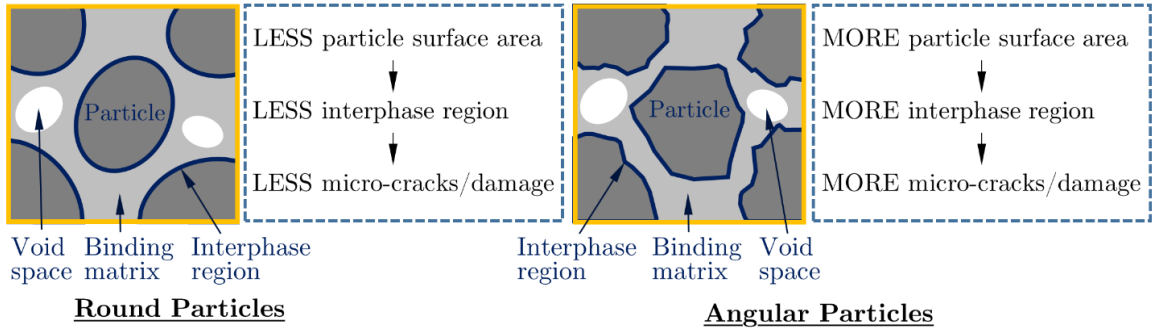


Figure 2.2. The influence of particle morphology on the formation of ‘weak’ interphase region.

Hypothesis #2: (High stress concentration on the binding substances). Sharp corners and surface concavity of the aggregate produce the localized ‘stress concentration’ on the nearby binding matrix [68]. The stress concentration caused by angular aggregate is likely to exacerbate the micro-damage compared to that caused by round aggregate, which will, in turn, negatively impact the mechanical performance. Consequently, it is highly possible that cracks initiate, propagate, and connect between the larger inter- phase regions, leaving more permanent micro-damage which can be manifested by early small-strain modulus reduction in the macroscopic material behavior.

Hypothesis #3: (Interlocking mechanism in CBM with significant micro-damage). Once CBM develops significant micro-damage at the interface of the aggregate and the binding matrix at a high stress-strain level, the interlocking mechanisms of frictional materials kick in. The angularity increases the shear resistance at the interface with the normal stress increases between the aggregate and the binding matrix at a higher loading level. Vast literature reports the angularity enhances the interlocking mechanisms, thus greater strengths are observed [20–26]. Therefore, the ‘damaged’ CBM with angular aggregates manifests higher strengths and moduli in the ultimate state, compared to the CBM with

round aggregates. It is also noted that this concept of the larger surface-area-to-volume ratio of angular aggregates can be translated by a larger quantity of the interlocking between particles and binding matrix, which generally supports the greater mechanical performance observed for the specimen with angular aggregates.

In summary, the angularity will ‘negatively’ (by Hypotheses #1 and #2) or ‘positively’ (by Hypotheses #3) impact the mechanical performance of CBM. Depending on which mechanisms dominate, the resulting performances (e.g. strength, elastic modulus) can vary. This study experimentally investigates and systematically addresses the influence of afore-stated morphology-driven particle scale mechanisms.

### 2.3 Aggregate Morphology Characterization

Determination of the aggregate surface-area-to-volume ratio requires 3D scanning and photogrammetric processing of individual particle, followed by the digital construction of high-resolution 3D models [70] to numerically measure the surface area and volume. The mobile imaging technique using portable devices such as smartphones, tablets, or digital cameras make this 3D modeling process more accessible and affordable, and it has been recently adopted for 3D aggregate modeling [71]. While this approach is technologically ‘sustainable’ with the newer generations of mobile devices and advances in the photogrammetry technique, evaluating the morphology through 3D modeling is still computationally demanding for a large number of particles. Therefore, this study adopts a set of the conventional 2D particle morphology descriptions to indirectly represent the 3D morphology and then to correlate the geometrical information with the material behavior of CBM.

### 2.3.1 Preparation of Coarse Aggregate Samples

Two different types of coarse aggregate are collected for the study, (a) crushed (angular), and (b) river (round) particles, of size #5 according to ASTM C33 [72], i.e., passing aggregate through 25 mm ranges from 90 to 100% by mass. Some photos of the sampled particles are shown in Figure 2.3, where the morphology difference is clearly observed. The samples are sieved from the bulk aggregates to minimize the variance of nominal size, so the particles that pass 12.5 mm sieve and retained at 9.5 mm sieve are then collected and used in the experimental study. Therefore, the size gradation effect is controlled and minimized. The aggregates are washed and stored in the dry oven at 110 °C for 24 hours to remove the moisture from the particles.



Figure 2.3. Two different sets of aggregate used in this study.

### 2.3.2 Characterization of Global Form and Local Angularity

#### 2.3.2.1 Morphology Description using Sphericity and Roundness

A variety of 2D morphology indices such as Sphericity and Roundness [73], Shape Factor and Angularity Factor [74], and Flat & Elongated Ratio and Angularity Index [75], have been developed to quantify the morphology. This study adopts the Sphericity and Roundness [35] to quantify the global form and local angularity respectively, which are broadly adopted in the aggregate research community. In particular, this study employs the sphericity defined by ‘width-to-length ratio’ among the five most common definitions of Sphericity, which was reported as the best estimate of the global form [41]. Both sphericity

and roundness theoretically range between 0.0 and 1.0. A higher sphericity indicates the global form is more equidimensional such as a sphere, while a higher roundness indicates less sharp corners of the particle. These indices quantify the 2D particle morphology based on 2D digital photos. Considering 3D morphology may look quite different depending on how the particle is seen from selected angles, this study takes five photos per particle including three images obtained from three orthogonal axes and two more images from random orientations. This study follows the procedure established by many other researchers to select the three orthogonal angles [76–78] that commonly corroborate using three orthogonal projections provide good accuracy for the 3D morphology quantification. Two additional random images are adopted to enhance the reliability of the image-based morphology analysis.

#### 2.3.2.2 Image-based Analysis Procedure

Image analysis is proceeded in five steps for each particle to characterize the morphology as outlined in Figure 2.4.

Step 1 - Image acquisition (2.4a): Thirty particles are randomly sampled from each type of the crushed and river aggregates. Five photos are taken on each particle, thus a total of 150 images are obtained for each group of the sampled aggregates. Note that  $\pm 0.05$  of the 95% confidence intervals for the mean values of both morphological indices are postulated. Assuming the resulting standard deviation is 0.1, the required number of images is about 16. Considering the total number of images taken is 150, the resulting mean value from this analysis can be statistically validated. Particles are placed on a grid paper whose cell size is 7 mm  $\times$  7 mm, i.e., the diagonal length is about 10 mm. The particle photos are taken using iPhone 7+ equipped with a 12-megapixel camera at 401 pixels per inch. This study

employs the affordable smartphone to demonstrate the proposed approach can be seamlessly applied to the engineering practice in a cost-effective manner, but any innovative imaging method may be adopted to acquire the aggregate images.

Step 2 - Foreground segmentation (2.4b): This step adopts the GrabCut algorithm [79] to segment the foreground particle image from the background that is implemented in OpenCV library [80]. This semi-automatic algorithm performs a ‘hard’ segmentation using an iterative graph cut, minimizing the energy defined in the objective function. The final output is a segmented particle image on a black background.

Step 3 - Image binarization (2.4c): The segmented image from Step 2 is then converted to a black/white binary image for use as the input for angularity computation. Accordingly, the color of pixels inside the foreground particle is changed to white.

Step 4 - Image vectorization (2.4d): The obtained binary image after Step 3 is a raster graphics with the pixels that appear as a grid of low-resolution squares. This may impact the roundness computation if the code does ‘overfitting’ when evaluating the local angularity. Therefore, the binary image is vectorized to minimize the impact that orients from the graphical noise. This study adopts an open source vectorization code, Potrace [81], to capture the best-fitting particle outline. The vectorized image is then converted to a high-resolution bitmap for use in the morphology analysis. The high-resolution bitmap is normalized to 1,000 pixels per circumscribed circle diameter (PCD) as recommended by Zheng and Hryciw [41] to use their morphology analysis code in Step 5.

Step 5 – Morphology computation (2.4f): This study adopts a sphericity and roundness computation algorithm and code developed by Zheng and Hryciw [41]. The high-resolution images are leveraged to analyze the aggregate morphology.



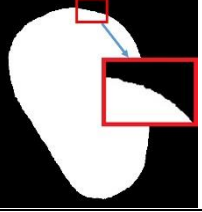
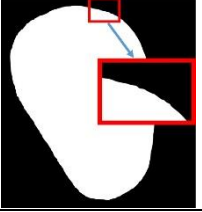
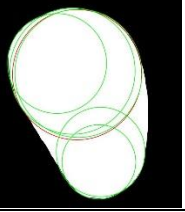
Step 1	Step 2	Step 3	Step 4	Step 5
				
(a) Image acquisition	(b) Foreground segmentation	(c) Image binarization	(d) Image vectorization	(e) Morphology computation

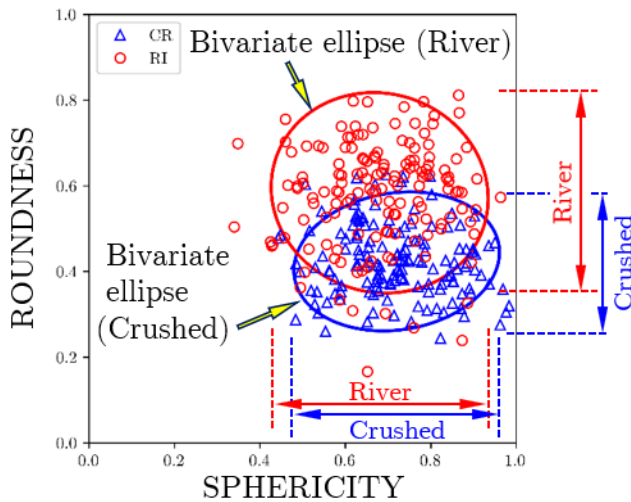
Figure 2.4. Five-step image analysis procedure.

### 2.3.2.3 Analysis Result

The results of the measured Sphericity and Roundness are plotted in Figure 2.5 with the ellipses representing 95% contour of the bivariate normal distributions for each aggregate morphology. The sphericity and roundness of all 150 projections are included in order to better represent the particle 3D geometry. The center of the bivariate ellipse for river (RI) aggregate, indicating the mean values, is located upper-left to that of crushed (CR) aggregate, and the width and height of the ellipse represent 95% intervals of bivariate normal distribution: (a) The sphericity of RI aggregate is lower than that of CR aggregate by 0.04 (to the horizontal axis), but the center and width of both ellipses are overall comparable to each other, meaning the global forms of two aggregate types are largely similar; (b) On the other hand, the mean value of the roundness of the RI aggregate is considerably higher than that of CR aggregate by 0.16 (to the vertical axis) despite some outliers located below CR aggregate. Furthermore, the RI aggregate shows a larger variation in the roundness than that of CR aggregate by 0.14 (i.e., 0.46 vs. 0.32), so the RI ellipse is located well above the CR ellipse.

This result can be interpreted that the CR aggregate has significantly more angular morphology than the RI aggregate. Therefore, it is conjectured that the CR aggregate has overall larger surface-area-to-volume ratios due to the significantly higher angularity, thus

confirming that these aggregate samples are suitable to investigate the influence of morphological angularity. The larger size of RI ellipse (i.e., larger variation in the roundness) is possibly attributed by the nature of how we obtain each aggregate: the crushed aggregate is produced by a crusher; the river aggregate is naturally occurring, which has inherently higher randomness in the shapes. Further, the computed covariance between sphericity and roundness, as manifested by the rotation of the bivariate ellipses, are respectively -0.001 and 0.0009 for the river and crushed aggregates, inferring that both parameters are negligibly correlated.



**Geometry of bivariate ellipses:**

- River aggregate:  
Center:  $(x, y) = (0.68, 0.58)$   
Size: (width, height) = (0.51, 0.46)  
Rotation: -17.46 deg.
- Crushed aggregate:  
Center:  $(x, y) = (0.72, 0.42)$   
Size: (width, height) = (0.48, 0.32)  
Rotation: 8.93 deg.

Figure 2.5. Morphology of crushed and river aggregates, where the distributions are statistically represented by the bivariate ellipses (courtesy of Drs. Chang Hoon Lee and Moochul Shin at WNEU).

The sensitivity of the evaluated morphology to the resolutions of the particle images is also investigated. Photos of a set of particles are taken at three different resolutions: 8, 12, and 24 megapixels (MP), and then the image analysis is performed via the same procedure described above to analyze and compare the aggregate morphology. A high-resolution 24.3-megapixel mirrorless digital camera is used to take 12 MP and 24 MP photos, and

different smartphones are used including the iPhone 7+ for 8 MP and 12 MP photos. An overall good comparison is made in the evaluated morphology obtained from all the photos. The largest differences in the resulting sphericity and roundness for given particles are respectively less than 1% and 5 %, which indicates the image-based analysis performed in this study is not sensitive to the resolution and the result is reliable.

### 2.3.3 Characterization of Surface Texture

Obtaining the mineralogical information of the crushed and river aggregates is important in the sense that the surface texture is largely determined by intrinsic mineralogy [43]. This study attempts to indirectly estimate the surface roughness by measuring the water contact angle, since the contact angle represents the surface roughness of materials [82,83], i.e., the mechanical characteristic of surface texture. To this end, water droplet tests are performed to measure and compare the contact angles of both river and crushed aggregates using a goniometer. Figure 2.6 shows the images of water droplets on a surface of (a) river and (b) crushed aggregates. Comparable contact angles of about  $30^\circ$  are consistently observed on both types of the aggregates, indicating the surface roughness are overall comparable to each other. Consequently, the influence of the surface texture is controlled in this study. While we recognize there is room for improvement for robust characterization of the surface texture, a systematic investigation of the surface texture effect is beyond the scope of this study and is left for future study.

It is also worthwhile to note that Pan et al. [29] reported that the influence of the surface texture on the fracture energy, a property measuring crack initiation and propagation, is relatively not significant as compared to the surface area determined by global form and local angularity. Therefore, any small difference and/or measurement error in the surface



texture between the two types of aggregates is not anticipated to significantly affect the experimental test results.

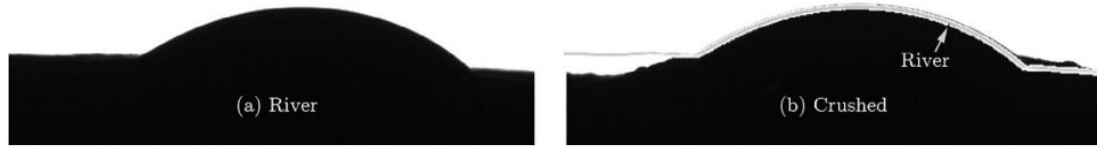


Figure 2.6. Water droplet test result – Image of droplets on (a) river and (b) crushed aggregates, where the outline of a droplet on a river aggregate is overlapped for optical comparison (courtesy of Drs. Chang Hoon Lee and Moochul Shin at WNEU).

## 2.4 Investigation of morphology effect on mechanical properties

### 2.4.1 Experimental Procedure

Two groups of cement-based specimens are prepared with each of CR and RI aggregates to experimentally investigate the influence of the coarse aggregate angularity on the mechanical properties of CBM. Table 2.2 summarizes the mix design proportions which is used to cast 32 cylindrical specimens of 76.2 mm  $\times$  154.2 mm dimension. The mixture proportion is designed such that for each type of aggregate (CR or RI) there is an identical volume of paste and aggregate (i.e. 52% paste, 43% aggregate, and 5% air by volume). The volume ratio of paste to aggregate is selected as 1.2, which is generally used for the normal-strength concrete. For normal-strength concrete, the compressive strength of concrete increases with increase in aggregate content [61]. In this study the mix proportions contain a fixed volume of aggregates (43%) for both types of aggregates. Air voids are intentionally introduced in concrete to reduce damage caused by freezing and thawing to increase durability. It reduces the strength of concrete, for each 1% increase in volume of air void, there is a 5% decrease in strength of concrete [84]. However, it increases the workability

of concrete. In this experimental investigation, a 5% air void is introduced in the mix portion. Fine aggregates smaller than 4.75 mm are deliberately excluded from the mix to focus only on the coarse aggregate morphology effects on the mechanical properties of the specimens, as discussed previously in the scope of study (Section 2.1.2). Aggregates are also washed and oven-dried to remove any inert particles from the aggregate surface and adjust absorption of aggregates in the mixture. The cylindrical specimens are then cured in a temperature-controlled chamber at 23 °C until the designed testing ages are achieved.

Table 2.2. Mixture proportion (per m<sup>3</sup> mortar) (courtesy of Drs. Chang Hoon Lee and Moochul Shin at WNEU).

Component	Crushed <sup>a</sup>	River <sup>a</sup>
Cement <sup>b</sup> (kg)	634	
Water (kg)	317	
W/C	0.5	
Coarse Aggregate <sup>c,d</sup> (kg)	1090	1121
Volume ratio of Paste to Aggregate	1.2	

Note:

- a. Both mortars are estimated to have 5% of air.
- b. Specific gravity of cement is estimated to be 3.15.
- c. Specific Gravity: 2.53 (Crushed) and 2.60 (River) per ASTM C127 [85].
- d. Absorption: 1.4% (Crushed) and 1.1% (River) per ASTM C127.

The thirty-two specimens are used to perform three different laboratory tests: (a) a splitting tensile strength test (10 specimens) according to ASTM C496 [86], (b) a monotonic compressive strength test (10 specimens) according to ASTM C39 [87], and (c) a cyclic compression test (12 specimens) according to ASTM C469 [88] at each of 1, 3, 8, 14, and 28 days of specimen ages. Figure 2.7 shows experimental set-up for three different tests showing the cylinder specimens before the tests, for which a 1,112 KN (250,000 lb) hydraulic compression machine is used. The adopted loading rate for splitting tensile

strength is about 0.7 MPa/min (100 psi/min) and it is about 0.14 MPa/sec (20 psi/sec) for both monotonic and cyclic compression tests complying with the corresponding standards. The elastic modulus of the tested cylinders are computed from the load-deformation response which is measured using an extensometer (as shown in Figure 2.7c).

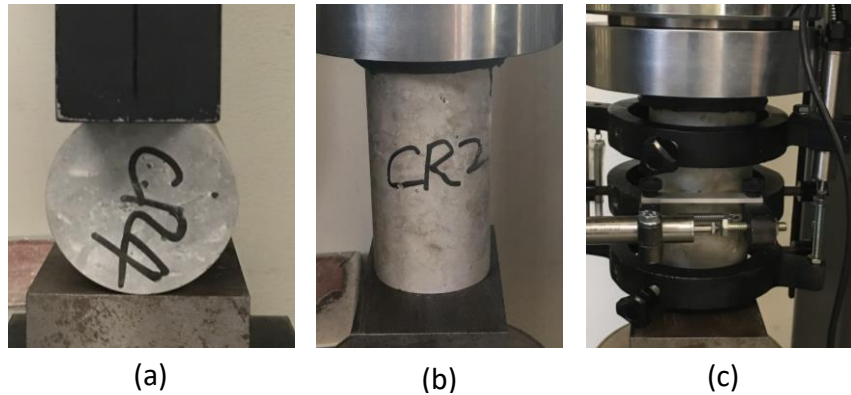


Figure 2.7. Test setups: (a) Splitting tensile strength test, (b) Monotonic compression test, (c) Cyclic compression test. (courtesy of Drs. Chang Hoon Lee and Moochul Shin at WNEU).

#### 2.4.2 Test Results and Discussion

Figure 2.8 shows the manifested splitting tensile strength values for CR and RI aggregates at 5 different test ages. The splitting tensile strengths increase with time for both types of aggregates. However, for CR specimens the values of splitting strength are clearly higher compared to that of the RI specimens. At 28 days, CR specimen has a 57% higher splitting tensile strength than that of the RI specimen.

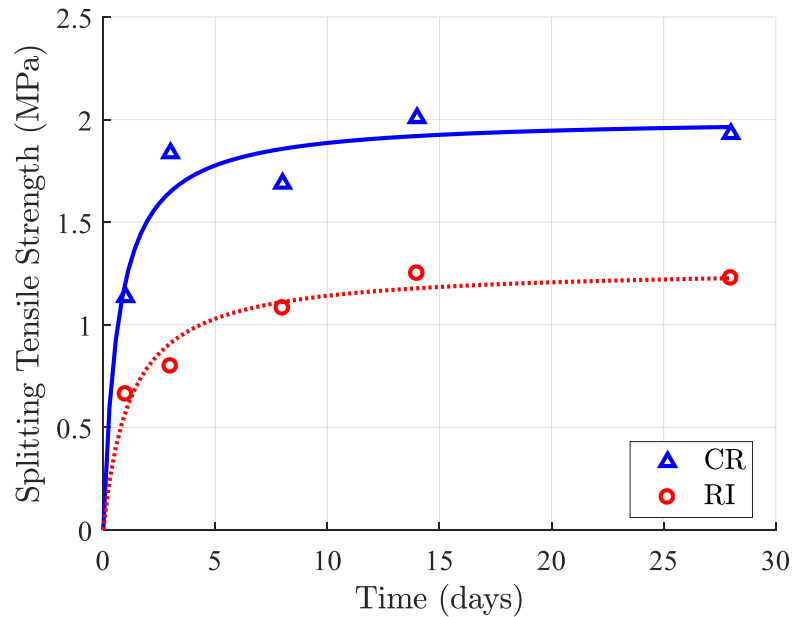


Figure 2.8. The splitting tensile strength of the tested 10 cylinders with respect to test ages (courtesy of Drs. Chang Hoon Lee and Moochul Shin at WNEU).

The measured compressive strengths of the cylinders are showed in Figure 2.9 for 5 different test ages. Similar to the results of splitting tensile strength test, here also the CR specimens showed higher compressive strengths than the RI specimens. At 28 days, the CR specimen has an 85% higher compressive strength than the RI specimen. These splitting and compressive strength results demonstrate the efficacy of the postulated mechanism #3 in the ‘damaged’ CBM (discussed in Section 2.2) and underpin the general observations in the works of literature, i.e., a higher strength is obtained with a higher aggregate angularity.

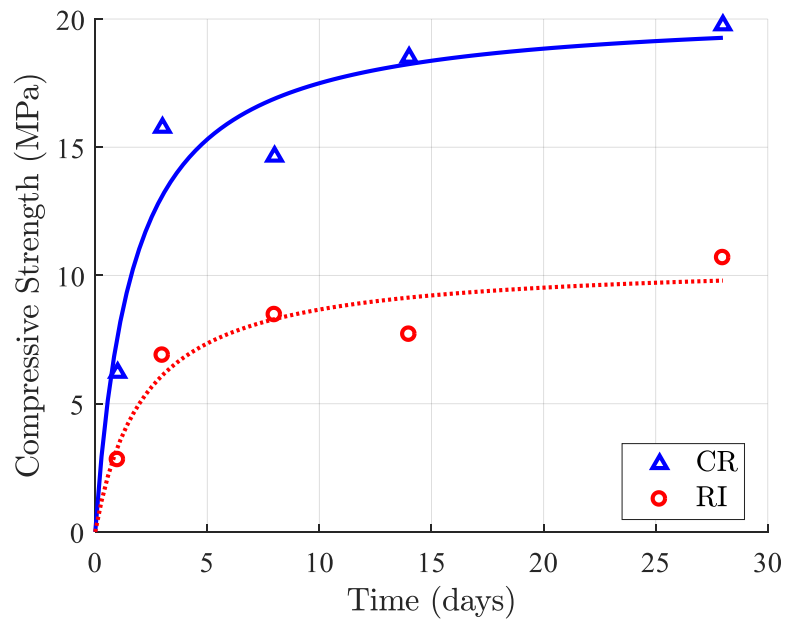


Figure 2.9. The compressive strengths of the tested 10 cylinders with test ages (courtesy of Drs. Chang Hoon Lee and Moochul Shin at WNEU).

Comparison of elastic moduli of each specimen at 14 and 28 days is shown in Figure 2.10 (the measurements taken at the earlier days are not available due to the improper readings from the extensometer). Unlike the compressive and tensile strength test results previously discussed, the RI specimens is found to have a higher elastic modulus than that of the CR specimens. This finding underpins the postulated mechanisms #1 and #2, whereby the angular particle morphology in CBM causes early small-strain modulus reduction while the round particle morphology delays early micro-damage initiation.

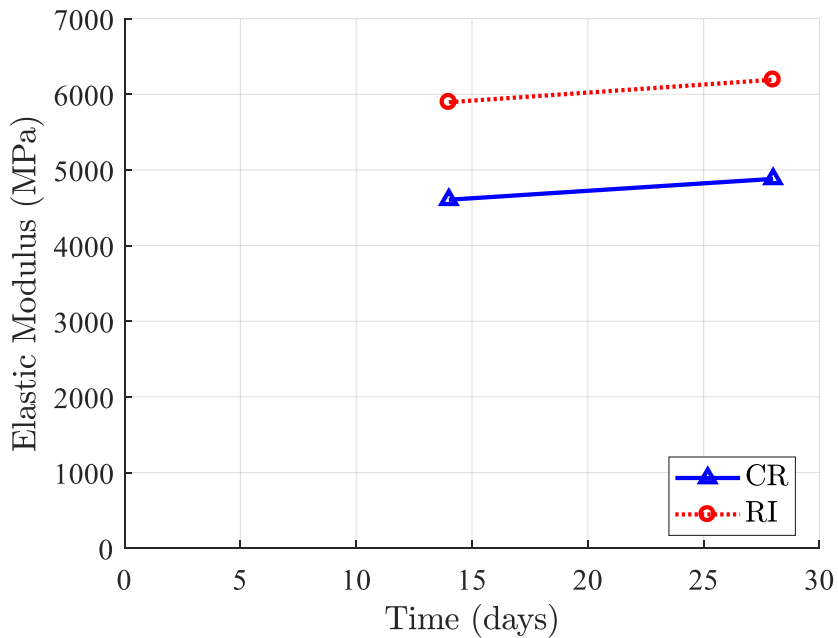


Figure 2.10. The modulus of elasticity of the tested cylinders at Days 14 and 28 (courtesy of Drs. Chang Hoon Lee and Moochul Shin at WNEU).

The cyclic compression tests are performed by ‘incrementally’ loading the cylindrical specimens at four consecutive cycles : (1) loading up to 40~50% of the compressive strength (obtained from the monotonic compression tests performed earlier) and unloading; (2) reloading up to 60~70% and unloading; (3) reloading up to 80~90% and unloading; and finally (4) loading until failure. The loading rate of 0.14 MPa/sec is adopted for this test.

The cyclic compression test results at 28 days are shown in Figure 2.11. Figure 2.11a shows the original stress-strain curve, while Figure 2.11b shows the normalized curve with respect to their respective peak compressive strength. The figure also confirms the trend observed in the splitting tensile and monotonic compression tests, i.e., the RI specimen shows a superior initial performance while the CR specimen shows a superior ultimate strength. There is a noticeable reduction in the secant modulus of CR specimen even at small strain and the secant modulus of the RI specimen is clearly higher at the first cycle. At the first

cycle, which is 40% of the peak compressive strength of CR specimen, there is a significant permanent damage. But at the first cycle, which is 45% of peak compressive strength, the RI specimen is still in elastic region (Figure 2.11b). As a result, the residual strain at the end of the first cycle is  $325 \mu$  for CR specimen which is significantly higher than  $50 \mu$  for RI specimen. In RI specimen, the higher elastic modulus is obtained at a significantly lower stress level (here, 40~45% of the peak compressive strength) by the lower deformation. Slate and Hover (1984) reported that the both elastic strain energy and fractured surface energy governs the strain at the stress level of about 30% of peak stress. Thus, smaller strain at a given stress level can be associated with a relatively higher elastic strain energy and lower fractured surface energy. However, once the specimens are significantly damaged by the repeated application of cyclic loading, the higher aggregate surface area in CR specimen positively influences the performance carrying more load by interlocking mechanism with the binding matrix at the particle interface. This is manifested in the last loading cycle where CR specimen possesses both higher modulus as well as strength compared to RI specimen.

In summary, the resulting stress-strain responses obtained from the cyclic loadings can be explained by the afore-stated morphology-driven particle scale mechanisms, i.e., the smaller permanent damage and the higher secant modulus of the RI specimen at the small-strain range can be explained by the mechanisms #1 and #2, while the higher strengths and modulus of the CR specimen at the relatively larger strain can be corroborated with the mechanism #3.

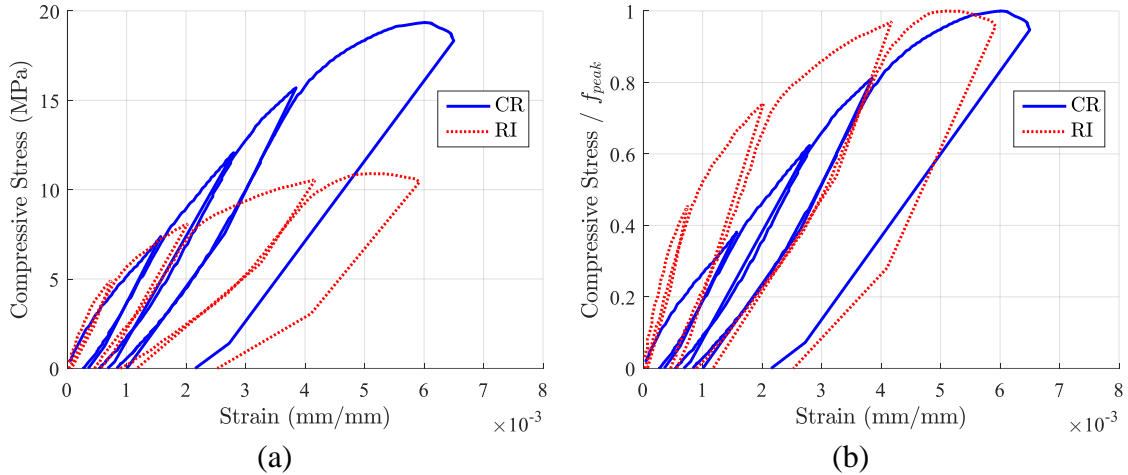


Figure 2.11. Responses under cyclic loading at 28 days; (a) Stress-strain curve of cylinders with crushed particles (CR) and river particles (RI); and (b) the curves ‘normalized’ by the peak compressive strength ( $f_{peak}$ ) (courtesy of Drs. Chang Hoon Lee and Moochul Shin at WNEU).

## 2.5 Concluding Remarks

This study investigates the effect of coarse aggregate angularity on mechanical properties of the cement-based materials (CBM). Three mechanisms driven by particle scale morphology are postulated to elaborate the angularity-dependent behavior that is largely under debate in the research community. This study makes a systematic approach by strategically (a) limiting the size to coarse aggregates, (b) preparing two types of aggregates with discernible difference in the angularity, while the other morphological properties (i.e., global form and surface texture) are comparable, (c) quantifying the morphology with the sphericity and roundness, not relying on conventional eyeballing, and (d) experimentally demonstrating the small-strain material performance is negatively influenced by the aggregate angularity. Consequently, the findings imply the use of the crushed (angular) particles would not be always beneficial to the material performance if subjected to



loadings inducing relatively low-level strain, where the rounded particles would lead to the better performance by delaying early micro-damage initiations.

Due to more number of micro-cracks, CBM with angular particles face durability problem especially in coastal regions where moisture penetration is frequent. In coastal regions, soluble sulphates in soil and water increase the risk of corrosion of reinforcing steel. In cold regions, moisture in cracks lead to freezing and thawing. This further ruptures the cracks and expands them resulting in significant deterioration in concrete strength [90]. Hence in coastal area and cold region, round aggregates provide better durability than crushed aggregate.

Due to high surface-area-to-volume ratio, angular aggregates have high voids. Hence, they require more water and paste to maintain workability [91]. The study also focuses on normal-strength concrete with a high W/C ratio of 0.5 to maintain workability. This is loosely cemented material, so cracks pass through the binder matrix and not through particles. How W/C ratio affects the influence of coarse aggregate morphology on CBM performance is left for future investigation.

The scope of this study is limited to normal-strength concrete where cracks pass through the interphase region. In concrete with light-weight aggregates, cracks pass through the aggregates. In high-strength concrete which is characterized by good bonding between aggregates and binding matrix, some cracks go through the aggregates [92]. The influence of aggregate angularity on high-strength concrete and concrete with light-weight aggregates is an area of future study. This study is limited to analysis of coarse aggregate angularity. Further research has to be done to completely understand the influence of fine

aggregate morphology on CBM. One of the future works is to incorporate the morphology effect in ACI codes to estimate elastic modulus and compressive strength of concrete.

In summary, CBM with round aggregates provide a higher elastic modulus, i.e. superior small-strain behavior, thus enhancing durability due to less microcracks in small-strain loading. On the other hand, CBM with angular aggregates provide a higher peak strength, i.e. better resistance to extreme loads.

### 3 A NEW INTERPRETATION OF THREE-DIMENSIONAL PARTICLE GEOMETRY: M-A-V-L

#### 3.1 Introduction

##### 3.1.1 Background

The influence of particle geometry is a key to understand the complex behavior of the granular materials, but our knowledge of the subject remains at best incomplete. The 3D particle geometry is characterized in terms of four parameters, i.e., morphology M, surface area A, volume V, and size L. The quantities of these parameters are interrelated, e.g., if size changes, surface area and volume also change. Morphology is also closely related to size, as morphology affects the size measurement [93] as well as surface area and/or volume. For example, Figure 3.1a shows two differently shaped particles of the same size (measured in terms of the diameter of particle's bounding sphere). These particles necessarily have different volumes and surface areas from each other. On the other hand, if the particle volume is same as shown in Figure 3.1b, these particles have different sizes and surface areas as well as the different morphology. If two particles with the same morphology are of different sizes, these particles have different volumes and surface areas (Figure 3.1c).

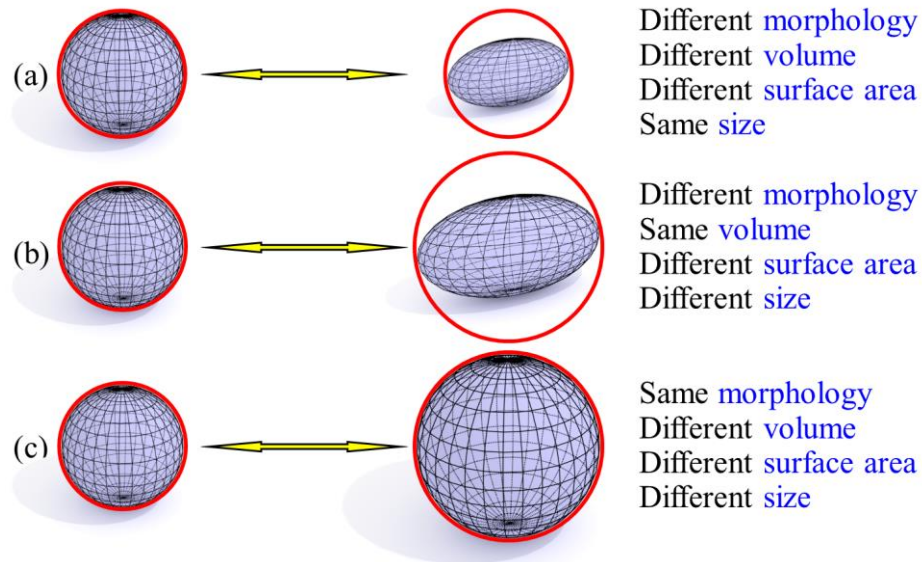


Figure 3.1. Interrelated 3D particle geometry parameters; (a) Two different particle morphology with the same size; (b) Two different particle morphology with the same volume; (c) Two different particles with same morphology having different volumes, surface areas and sizes.

The definitions of particle volume, surface area, and size are clear, and each parameter is characterized by a single scalar value. On the other hand, three factors have been traditionally used for the characterization of morphology at three different scales (discussed in Chapter 1): (i) global form, (ii) local angularity, and (iii) surface texture. Regularity  $\rho$  is defined as the arithmetic average of Sphericity and Roundness. Sphericity (descriptor for global form) and Roundness (descriptor for local angularity) are traditionally defined in 2D using the particle projection images [41]. These 2D descriptors have been commonly adopted due to the ease of characterization of global form and local angularity, but which have inherent limitation to interrelating the morphology with volume and surface area that are defined in 3D.

The ‘true’ Sphericity is a 3D descriptor developed by Wadell [40] that characterizes the particle morphology by comparing its surface area to that of a sphere with the same volume. It is worth to note the ‘true’ Sphericity is not an indicator of the global form only, because it is a function of the surface area, thereby also influenced by the local angularity [94,95]. This 3D Sphericity formula has not been popularly used due to the challenge of measuring the surface area until recently the 3D optical characterization techniques became available in the research community such as X-ray computed tomography [96,97], 3D laser scanning [98,99], photogrammetry [100]. Other 3D Sphericity descriptors were also developed with the advances in the 3D optical characterization techniques, e.g., Alshibli et al. [101] used 3D synchrotron microcomputed tomography to obtain 3D images of various soil particles and proposed a new Sphericity index  $I_{\text{sph}} = V / V_{\text{sph}}$ , where  $V_{\text{sph}}$  is the volume of a sphere with a diameter equals to  $d_s$  which is the shortest principal axis length of the particle that passes through the center of particle mass.

Kong and Fonseca [102] proposed another volume-based Sphericity index similar to  $I_{\text{sph}}$  such that the maximum value of the index can be 1. Bullard and Garboczi [103] introduced two 3D Roundness concepts:  $R_w$ , a 3D analog of Wadell’s 2D Roundness, and  $R_n$  for a simple 3D angularity measurement that accounts for the angle between the surface position vector and the unit normal vector over the particle surface. Zhao and Wang [95] introduced a 3D Roundness that considers the curvatures at all particle corners, which may be viewed as another 3D interpretation of Wadell’s 2D Roundness. Cruz-Matías and others [42] introduced a 3D Roundness index that considers the difference between the particle morphology and the reference ellipsoid. Although these developed 3D descriptors

contributed to a realistic measurement of the 3D particle morphology, the interrelation of morphology to the other 3D geometry parameters was not considered.

### 3.1.2 Objective and Scope

**Problem statement #1:** Morphology is closely related to surface area, volume, and size, as demonstrated with the examples in Figure 3.1, which therefore may be considered as a set of ‘morphology parameters.’ If so, can we represent morphology  $M$  as a function of surface area  $A$ , volume  $V$ , and size  $L$  instead of the conventional approach that characterizes the morphology in terms of Sphericity and Roundness (that are independently measured of surface area, volume, and size)? While the importance of characterizing the individual contributions of Sphericity and Roundness to overall morphology is appreciated, this study aims to address this new question as it would provide a new perspective that unravels the ‘interrelation’ of the four geometry parameters, which has not been possible with the conventional approach.

Previous research mostly considered particle morphology and size as the major parameters that could influence the granular material behavior, for which the size was controlled in the granular material specimens to study the morphology effect or the other way around. However, it would be important to comprehensively address the four-dimensional aspects (i.e., volume, surface area as well as morphology and size) of the 3D particle geometry to better understand the particle geometry effect and enhance the predictive capability. For example, if two particle models having different morphology are adopted in particle-based simulations (e.g., discrete element method) to study the morphology effect on the granular material behavior, the different volume and surface area may produce additional or uncontrolled effects on top of the effect by different morphology if sizes are same (e.g.,

Figure 3.1a). While previous studies on the granular materials mostly focused on particle morphology or size effect, the volume of solid particles is also an important factor that needs to be systematically considered as it is a major parameter that determines the granular skeletal density. Furthermore, the particle surface area is another important factor, e.g., soil plasticity is greatly influenced by the surface area [104], [105], and also plays a critical role in the performance of cemented granular materials (e.g., concrete) due to its direct impact on the quantity of bonding characteristics between particle surface and binding matrix [14,67–69,106]. The previous studies commonly corroborated that the interface of particles and binding matrix, known as the “interface transition zone (ITZ),” plays a critical role in the load-transferring mechanism in the cemented granular materials and the quantity of bonding characteristics at this ITZ is governed by the particle surface area. The authors in elsewhere [106] demonstrated the particle surface area is a critical mediator correlating the particle morphology with the mechanical performance of cemented granular materials due to its direct impact on the bonding quantity at the ITZ.

**Problem statement #2:** Particles of different morphologies, if size is same, manifest different volumes and surface areas. Previous research that focused on the particle morphology effect on the granular material behavior adopted particles of different morphology in the parametric study, but considering these particles also present different volumes and surface areas, how can we conclude the different behavior is caused by the different morphology only? Hypothetically speaking, different particle morphologies having same volume, surface area, and size may need to be considered to understand the morphology effect. However, it is implausible to have such particles as implied by the examples in Figure 3.1 and unconvincing to control all four geometry parameters to

develop such particle models for discrete element analysis. Furthermore, particle volume and surface area are also significant factors that affect the granular material behavior. Therefore, it would be important to address the four-dimensional aspects of 3D particle geometry to better understand the parameters' combined influence on the granular material behavior as it is hard to independently discuss the effect of one parameter from the others. Comprehensive characterization of the particle geometry 'distributions' is a prerequisite to better understand the causality between the particle geometry effect and the granular material behavior. Previous research mostly focused on the morphology and size effect, for which it was necessary to characterize at least three parameters, i.e., Sphericity, Roundness, and size. A 3D scatter plot could be developed with data markers to describe the distributions, i.e., each marker representing the geometry of a particle in 3D plot space, where each axis refers to Sphericity, Roundness, and size. However, to the best of the author's knowledge, this approach has not been adopted in the engineering practice possibly because a 3D scatter plot is difficult to interpret if looked at one viewpoint and is not immediately obvious as multiple figures are required from different viewpoints for better interpretation. Engineers, instead, have separately described the distributions in 2D plot space to facilitate the data interpretation [48,52,107–110] as shown in Figure 3.2. However, the geometry parameters are not cross-referenced with this approach, thus only partial information is deliverable. For example, as illustrated in Figure 3.2, it is not possible to find out the corresponding Sphericity or Roundness for a particle size of interest, and vice versa.



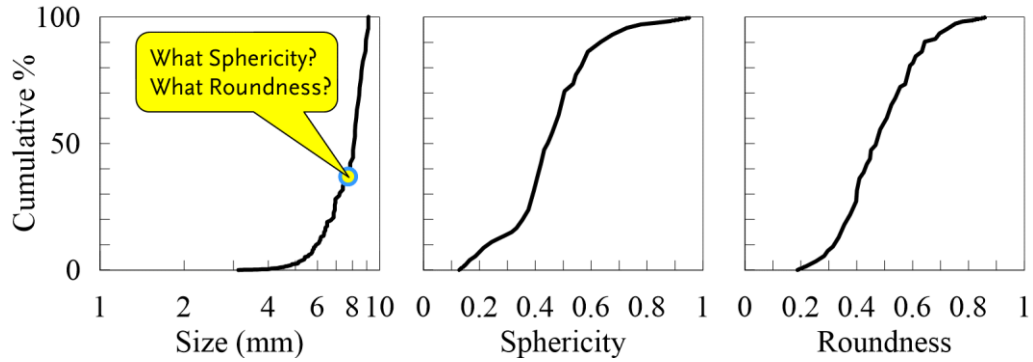


Figure 3.2. Separate description of particle size and morphology distributions.

**Problem statement #3:** As discussed above, it is already challenging to make a comprehensive description of the geometry parameter distributions even for three parameters without losing the valuable information regarding the parameters' relations. Along with the need of addressing the four-dimensional aspects of 3D particle geometry enunciated with the problem statements #1 and #2, such comprehensive description may be even more challenging with the four geometry parameters. This study aims to introduce a new approach that can graphically preserve the four parameters' relations when plotting the parameter distributions in 2D plot spaces, which helps comprehensively describe the four-dimensional aspects of 3D particle geometry.

To address the problem statement #1, this study introduces a new formula in Section 3.2 that can systematically quantify the interrelation of four 3D particle geometry parameters, morphology  $M$ , surface area  $A$ , volume  $V$ , and size  $L$ . With the new formulation, a parameter can be represented as a function of the other three, which enables to comprehensively address the four-dimensional aspects of the 3D particle geometry on two 2D plot spaces. This plotting approach to address the problem statement #3 is discussed in Section 3.3. The new formula and plotting method will help better understand the

parameters' combined influence on the behavior of granular materials (the problem statement #2), which is demonstrated in Section 3.4.

### 3.2 Proposed Formula for the New Interpretation

This study leverages the fundamental geometric principle: 'morphology is related to surface-area-to-volume (A/V) ratio.' An example is shown in Figure 3.3, where the A/V ratios are compared for the five different particle models having a same unit volume. The sphere has the smallest A/V ratio, which increases with more angular morphology. The A/V ratio of a cube is 1.24 times higher than that of a sphere with the same volume. The A/V ratio of a regular tetrahedron (which is more angular than the cube) is 1.49 times higher than the sphere. The A/V ratio also increases with elongation. The A/V ratio of a stretched tetrahedron in the figure is 1.65 times higher than the A/V ratio of the sphere with the same volume (The length of three edges of stretched tetrahedron is 3.2 each, and the length of the other edges is 1.5). With extreme angularity, the A/V ratio becomes significantly larger than that of the sphere as shown for the great stellated dodecahedron in the figure.

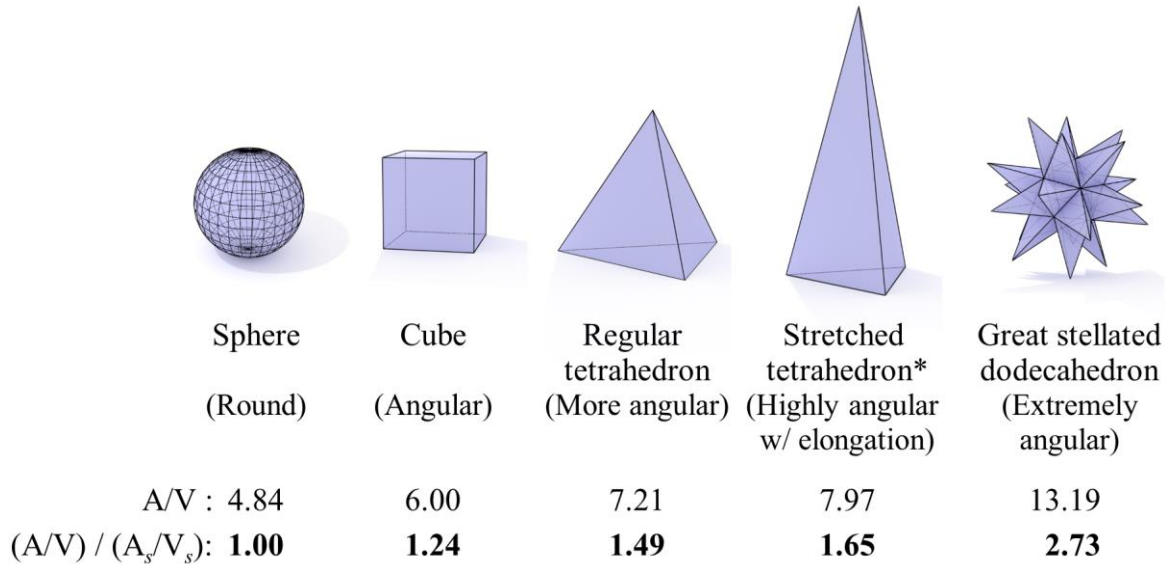


Figure 3.3. Morphology related to surface-area-to-volume (A/V) ratio.

While the A/V ratio is related to particle morphology, it is critical to note that the ratio is not constant for a given morphology because the value depends on the size as implied by its unit, which is a reciprocal length ( $L^2/L^3 = L^{-1}$ ). Therefore, the A/V ratio is inversely proportional to the size. For this reason, the product of A/V ratio and size turns out to be an invariant for a given morphology, which therefore can be leveraged as a morphology indicator. Building upon this concept, this study proposes a new formula (Equation 3.1) that interprets the 3D particle morphology M as a function of the other geometry parameters, i.e., surface area A, volume V, and size L:

$$M = (A/V \times L) / (A_s/V_s \times L_s) = (A/V \times L) / 6 \quad 3.1$$

where the A/V ratio is multiplied by L for the scale-independent characterization of a given particle morphology, which is unit-less. The subscript *s* in Equation 3.1 means sphere. Therefore, M indicates the relative morphological irregularity compared to the sphere. The A/V × L does not change for a given morphology and A<sub>s</sub>/V<sub>s</sub> × L<sub>s</sub> (of sphere) is invariantly 6. Therefore, the minimum possible value of M is clearly 1, and is higher than 1 for typical

mineral grains. It is interesting to note that  $M$  is a size-independent parameter, although  $M$  is expressed as a function of  $L$  (size).

Figure 3.4 demonstrates how the new formula is interpreted, in which three different spheres (Figure 3.4c, d, and e) are scaled to match one of  $V$ ,  $A$ , or  $L$  of the irregularly shaped particle in Figure 3.4b (highlighted in gray). The 3D particle model of the irregular morphology is a polyhedron with 10,374 triangular faces in its surface mesh, which is developed from a mineral grain after 3D scanning using a photogrammetry technique introduced in Zhang et al. [71]. A larger particle with the same irregular morphology is also shown in Figure 3.4a, which is 1.5 times larger than the particle in Figure 3.4b by size. The volume and surface area of the particles in Figure 3.4a and b are numerically obtained from the developed 3D polyhedron model after scaling the size to 2.25 and 1.5 cm, respectively.

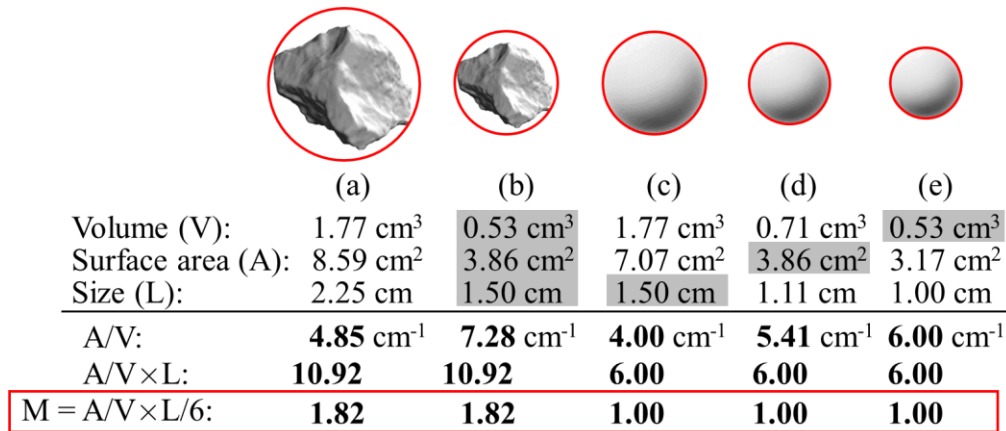


Figure 3.4. 3D morphology ( $M$ ) translated as  $A/V \times L/6$ .

Following observations can be made: (i) Particle morphology is related to  $A/V$  ratio, thus the irregular particle in Figure 3.4b has a higher  $A/V$  ratio compared to the sphere of the same  $L$  in Figure 3.4c, (i.e.,  $7.28 \text{ cm}^{-1}$  vs.  $4 \text{ cm}^{-1}$ ); (ii) Since the  $A/V$  ratio is inversely proportional to the size, the  $A/V$  ratio increases while  $L$  decreases. For example, the  $A/V$

ratio of sphere in Figure 3.4e is larger by 1.5 times compared to that in Figure 3.4c (i.e.,  $6 \text{ cm}^{-1}$  vs.  $4 \text{ cm}^{-1}$ ), while L is smaller by 1.5 times (i.e., 1.0 cm vs 1.5 cm). This principle also holds true for the irregularly shaped particles (Figure 3.4a, and b): the A/V ratio increases by 1.5 times from 4.85 to  $7.28 \text{ cm}^{-1}$  and L decreases by 1.5 times from 2.25 to 1.50 cm; (iii) Therefore, the  $A/V \times L$  values remain the same for each morphology regardless of the sizes, i.e., 10.92 and 6.0; (iv) The  $A/V \times L$  for any sphere is invariantly 6, thus the minimum possible value of M is clearly 1. The example in Figure 3.4 demonstrates that the higher the morphological irregularity is, the higher the M value becomes. This study witnesses the maximum value of M is about 3 for typical mineral particles based on the Krumbein and Sloss chart [111], which will be further discussed in Section 3.4.

With the new formulation  $M = A/V \times L/6$ , if one knows A, V and L, then morphology can be evaluated in terms of M. On the other hand, in previous studies on the granular materials, the morphology was separately evaluated in addition to the information of A, V, and L. The examples in Figure 3.1 can be systematically described by the proposed formula,  $M = A/V \times L/6$ , regarding how the other three parameters may change when one of the parameters is kept constant. In addition, this formula explains the ‘unilateral’ relation between morphology and size; it is clear that the change of M impacts A, V, and L values from the formula, so change of M may change L (Figure 3.1b). However, the change of L does not change M (Figure 3.1c), i.e., simply scaling of the particle size does not change the morphology. The A/V ratio is linearly proportional to  $1/L$  for a given morphology, so the change of L is canceled out by the change of A/V, which makes M invariant of the size. Therefore, the ‘unilateral’ relationship between morphology and size can be explained with the new formula.

### 3.3 Four-Dimensional Aspects in the 3D Geometry Parameter Distributions

#### 3.3.1 M-A-V-L Approach for Comprehensive Description of the Parameter Distributions

The proposed formula,  $M = A/V \times L/6$ , helps graphically preserve the relations of the four 3D particle geometry parameters when plotting the parameter distributions. This paper demonstrates the approach with two 2D spaces, (i) L vs. M and (ii) A/V vs. V, where A/V works as the messenger between the two spaces as  $A/V = M/L \times 6$ . Therefore, this approach helps comprehensively address the four-dimensional aspects of the 3D particle geometry. Two particle groups are numerically developed as below to demonstrate the efficacy of the proposed approach:

(a) Mixed morphology group, where a total of 100 polyhedral particles are modeled with a variety of morphology such that the evaluated M ranges between 1 and 3. In Figure 3.5, the particle models are presented with the computed Sphericity, Roundness, and M. The particle size ranges from 3 mm to 9 mm, which is also presented in the figure. The sizes are deliberately controlled such that smaller particles tend to have a more irregular morphology to distinguish the distribution from the group (b) below. It is worthwhile to note that the relation between size and morphology in these synthetic particle models is just for demonstration purpose, which does not imply smaller mineral particles in nature have a more irregular morphology.

(b) Near-sphere group, where another 100 polyhedral particles are modeled to be near-spherical. The particle models are shown in Figure 3.6, for which the Sphericity, Roundness, and M also are evaluated. The particle shapes in this group are all similar, so the evaluated M is near-uniformly distributed and is close to 1. The sizes are randomly selected between 3 mm and 9 mm, which are also shown in the figure. The geometry

property values of the two groups of 100 particles are provided in Appendix A (Table A.1 and Table A.2).

A 2D image of each particle is used to analyze the conventional Sphericity and Roundness, for which the orientation with the maximum 2D projection area is selected as it is the most possible orientation when the particle is placed on a flat surface due to the higher stability [112]. A Sphericity and Roundness analysis code by Zheng & Hryciw [41,113] is utilized for the 2D image-based morphology analysis. A sample particle model is selected and shown in the green circle in Figure 3.5, whose corresponding data points are marked in Figure 3.7. The size of the sample particle is 5.886 mm, and the computed Regularity  $\rho$  (i.e., average of 2D Sphericity and Roundness) is 0.3955 (thus  $1/\rho$  is 2.528).

The parameter M measures the overall 3D morphology, while the conventional Sphericity and Roundness quantify the 2D morphology at both the large and intermediate scales respectively. While direct comparison may not be made as these are defined in different dimensions, the M tends to increase with elongation and angularity (i.e., lower Sphericity and lower Roundness) and vice versa. For example, the particle with a relatively high M value (= 2.313) located at 6–1 (row # – column #) in Figure 3.5 has a low Sphericity and a low Roundness. On the other hand, the particle with a low M value (= 1.064) located at 1–10 in the same figure has a high Sphericity and a high Roundness.

There are particle models in Figure 3.5 and Figure 3.6 that have practically the same M values although Sphericity and Roundness are different. For example, the particles located at 1–1, 1–2, and 1–3 in Figure 3.5 have the practically same M values with the particles in Figure 3.6 located at 6–6, 2–3, and 6–5 respectively. The three particle models in Figure 3.5 are more equidimensional and angular (i.e., higher Sphericity and lower Roundness)

compared to the particle models in Figure 3.6 that are more elongated and round (i.e., lower Sphericity and higher Roundness). Therefore, the compensating effect results in the same M value that may be seen as a limitation, but which is necessarily not. This may be better understood with analogy to Regularity  $\rho$ : Regularity is a function of Sphericity and Roundness, so it is necessary to evaluate Sphericity and Roundness first (i.e., individual morphology parameters) to estimate the Regularity. It is worthwhile to note that previous studies demonstrated Regularity was a reasonable indicator of various soil mechanical properties at both small and large strain levels [6,9] and facilitated the data interpretation as it is a single measure of overall morphology. Although the compensating effect may result in same  $\rho$  value, the individual contributions of Sphericity and Roundness can be analyzed as the data is already available. Likewise, M is a function of A, V, and L, which can be considered as individual morphology parameters. The A, V, and L need to be evaluated first to estimate M. Although the compensating effect may result in same M value, analogous to Sphericity and Roundness to the Regularity, the individual contributions of the three parameters (i.e., A, V, and L) to M can be assessed. For example, although particle 1–2 in Figure 3.5 has the same M value as that of particle 2–3 in Figure 3.6, these two particles have different A, V, and L values from each other: the A, V, and L values of particle 1–2 (Figure 3.5) are 214.14 mm<sup>2</sup>, 280.71 mm<sup>3</sup>, and 8.719 mm, respectively, which are different from those of particle 2–3 (Figure 3.6), 178.87 mm<sup>2</sup>, 221.99 mm<sup>3</sup>, and 8.262 mm.

It is also interesting to see the differences in Roundness between these particles are larger than those in Sphericity, e.g., the Roundness values of 1–2 in Figure 3.5 and 2–3 in Figure 3.6 are 0.321 and 0.858, while the Sphericity values are 0.977 and 0.879. As discussed in



Chapter 1, the local angularity characterizes the morphology feature that is smaller than the global form by one order of magnitude. Therefore,  $M$  appears to reasonably reflect the different contributions of morphology factors at different length scales. It however does not mean  $M$  underestimates the local angularity, as  $M$  value can be significantly high with the local angularity only. For example, the great stellated dodecahedron in Figure 3.3 is not elongated but angular, and its  $M$  value is 5.33, which is very high.

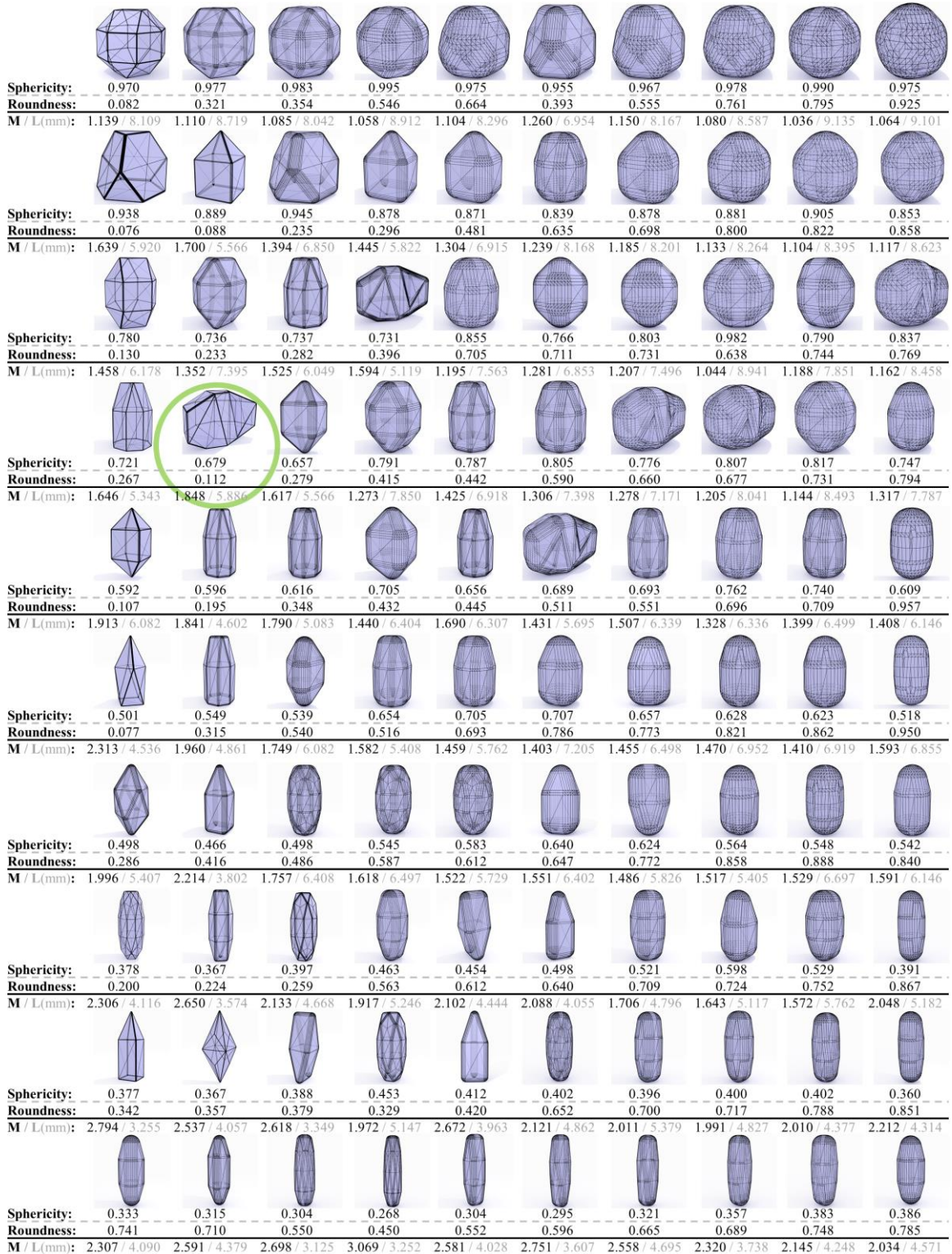


Figure 3.5. Particle models of mixed morphology group evaluated with Sphericity, Roundness, and proposed M values. The size L is shown next to M. The particle in the green circle is selected as a sample particle for the demonstration of interrelation of geometry parameters (See Figure 3.7).



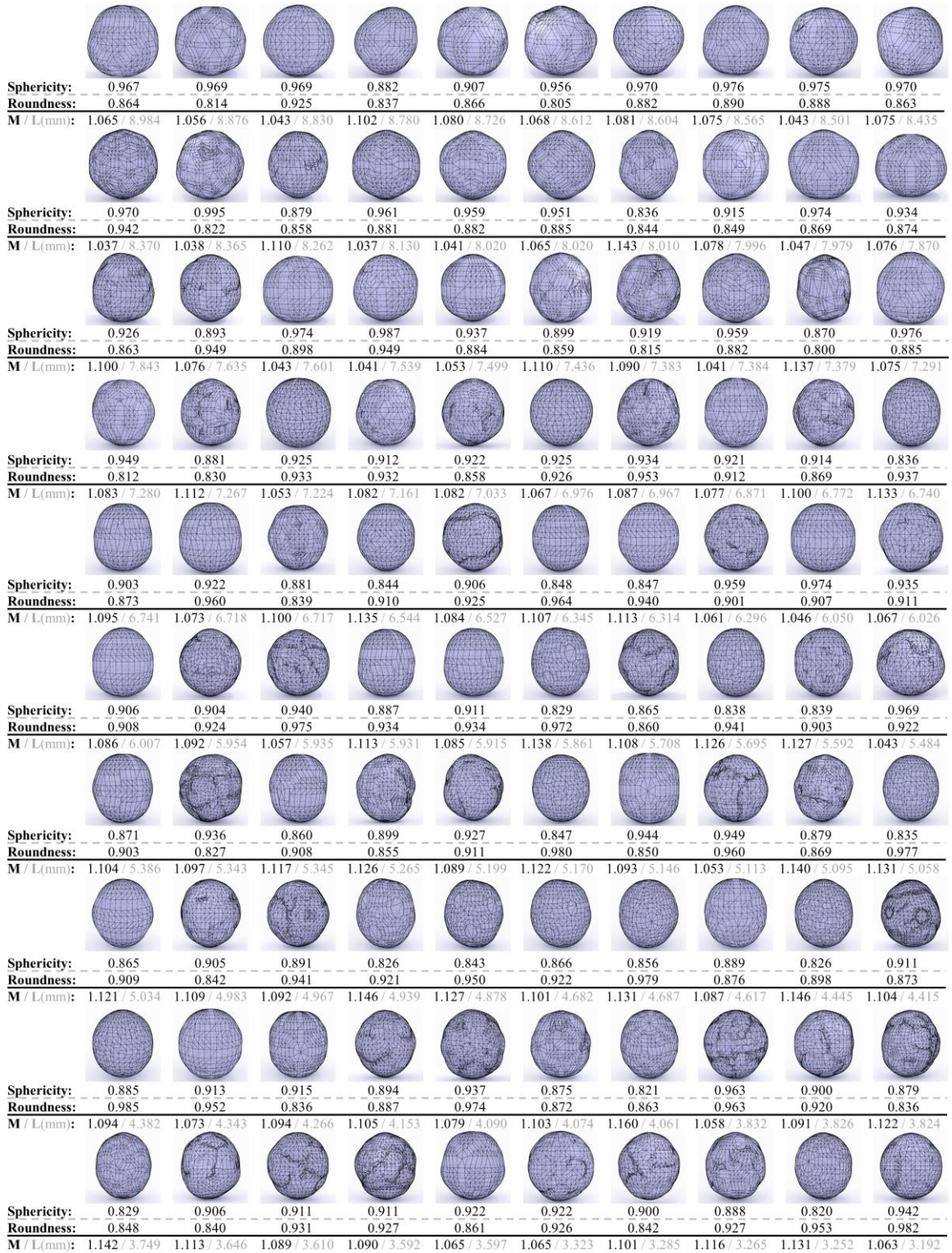


Figure 3.6. Particle models of near-sphere group evaluated with Sphericity, Roundness, and proposed M values. The size L is also presented next to M.

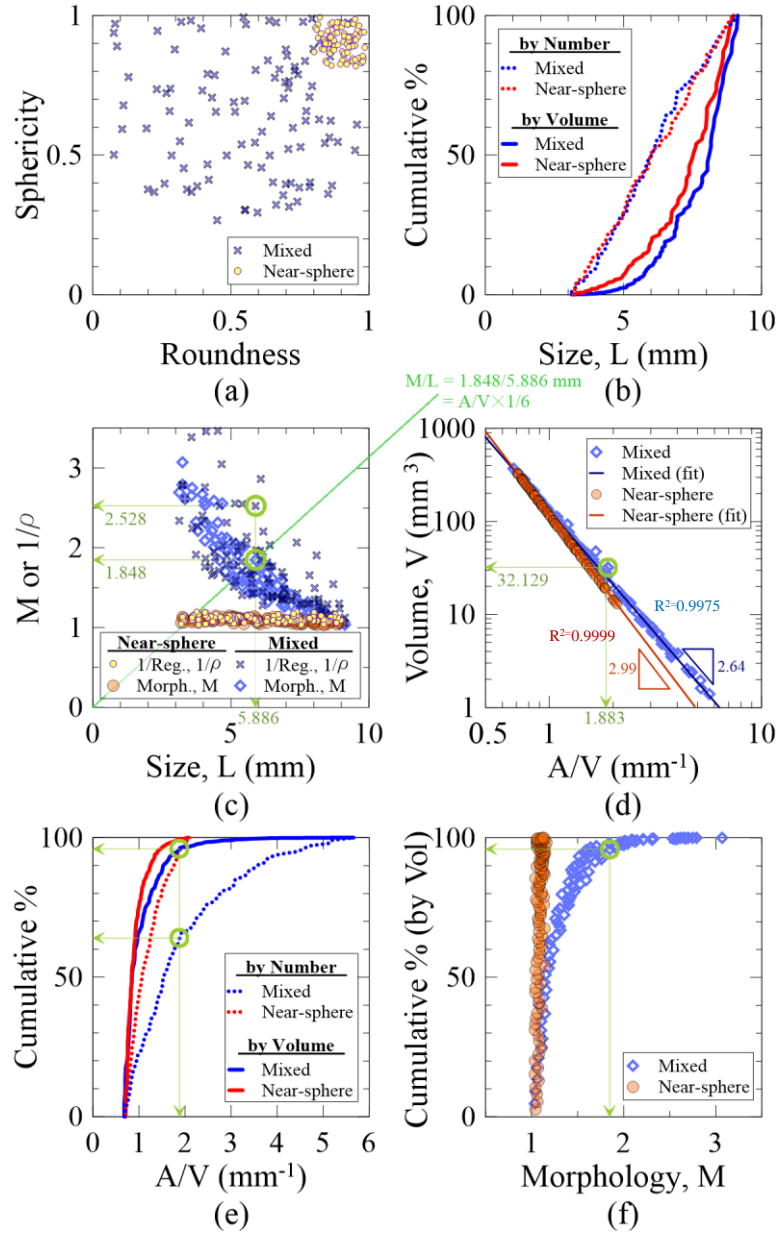


Figure 3.7. Description of the distributions of the ‘interrelated’ particle geometry parameters, where the parameter values of the sample particle (selected in Figure 3.5) are marked with green circle symbols; (a) Morphology distribution using conventional Sphericity and Roundness; (b) Particle size distributions for mixed morphology and near-sphere groups evaluated in terms of particle number and volume, respectively; (c) Combined description of M and size L; (d) Combined description of A/V ratio and V; (e)

Distributions of A/V ratios evaluated in terms of particle number and volume, respectively;  
(f) Distributions of M by volume.

Figure 3.7 demonstrates how the proposed formula,  $M = A/V \times L/6$ , can be used to comprehensively describe the evaluated particle geometry parameters for the two synthetic particle groups in Figure 3.5 and Figure 3.6. The evaluated Sphericity and Roundness are plotted in Figure 3.7a. The data points for the mixed morphology group are spread over the space due to the variety of morphology, while those of the near-sphere group are concentrated in the upper-right corner due to the overall narrow range of morphology values with near-equidimensional and round shapes. Figure 3.7b shows the particle size distributions of the two groups that are evaluated by both the number and volume of particles shown in terms of the cumulative percentage. The size distributions by the number of particles are overall close to each other. However, the difference is more apparent in the distributions if evaluated by the volume because the particles in near-sphere group have higher volume compared to the irregularly shaped particle of same size in the other group. This can be explained by the example in Figure 3.4, where the volume of sphere in Figure 3.4c is higher compared to the irregularly shaped particle of the same size in Figure 3.4b. The relations of geometry parameters in the distributions can be effectively described by using two 2D plots: a plot presenting L vs. M (Figure 3.7c). This plot can relate M and L to A/V, because  $M/L = A/V \times 1/6$ ; another plot presenting the combined A/V vs. V distribution (Figure 3.7d), where the surface area A can be retrieved by  $A/V \times V$ . Therefore, M-A-V-L approach can be used to comprehensively describe the distributions of the four 3D particle geometry parameters, whereby the relations of parameters are graphically contained in these two 2D plots.

The L vs. M distributions are shown in Figure 3.7c for both mixed morphology and near-sphere groups. The morphology is also evaluated by Regularity  $\rho$ . The inverse of Regularity ( $1/\rho$ ) is used for consistent comparison against M because a higher  $\rho$  represents near-equidimensional and round shape, while a higher M represents the opposite. Figure 3.7c is a way that can combine the information from Figure 3.7a and b that are conventional characterization approach that presents morphology and size distributions separately, which therefore makes it hard to examine the relation of those. On the other hand, Figure 3.7c combines both information in a single plot which facilitates the data interpretation, e.g., which clearly shows the relation between morphology and size in the mixed morphology group, i.e., the smaller the size is, the more irregular the morphology is. Despite the similar trend for both plots using M and  $1/\rho$ , there is more data scatter in the  $1/\rho$  plot. This scatter is possibly due to the inaccuracy associated with the 2D characterization of 3D particle morphology, and the characteristic of the reciprocal function  $1/\rho$ , as  $1/\rho$  nonlinearly increases as  $\rho$  gets smaller for low Sphericity and low Roundness. Figure 3.7c also depicts the overall similar particle morphology distributions on the near-sphere group with  $M \sim 1$  and  $1/\rho \sim 1$ , i.e., close to the minimum possible value for both descriptors. The plots shown in Figure 3.7c may be represented by probabilistic density distributions if the Z-axis is used to indicate the density of data.

The A/V vs. V distributions are shown in Figure 3.7d. The data in Figure 3.7c can be cross-referenced to the A/V ratio in Figure 3.7d as  $A/V = M/L \times 6$ . For example,  $M/L = 1.848/5.886$  mm for the sample particle from Figure 3.7c, thus the A/V ratio can be computed to  $1.883 \text{ mm}^{-1}$  ( $= M/L \times 6$ ). The volume V of the sample particle then can be found in Figure 3.7d, which is  $32.129 \text{ mm}^3$ . The surface area A then can be estimated by

$A/V \times V$ , which is  $60.5 \text{ mm}^2 (=1.883 \text{ mm}^{-1} \times 32.129 \text{ mm}^3)$ . Therefore, once two plots that represent (i) L vs. M and (ii) A/V vs. V distributions are provided, the four-geometry information (M, A, V, and L) can be retrieved for every single particle. In other words, the individual contributions of A, V, and L (as the morphology parameters) to M can be retrieved by using this approach. Regularity  $\rho$  also represents the single measure of morphology like M. However, if  $\rho$  is used in the place of M, it is not possible to cross-reference the data between the (i) L vs.  $\rho$  and (ii) A/V vs. V plots, so retrieval of the complete four geometry information is not feasible.

### 3.3.2 Power Law Relation between A/V and V

Interestingly, the A/V and V in Figure 3.7d show a linear relation in log-log scale, which can be approximated by a ‘power law’. The relation of A/V and V for the mixed morphology group can be approximated to  $V = (A/V)^{-2.64} \times 129.66$ , and then to  $\log(V) = -2.64 \times \log(A/V) + \log(129.66)$ . The fitted line is shown with a slope of -2.64 in the log-log space, and the equation can be reformulated to  $\log(V) = 1.61 \times \log(A) - 1.29$ , which directly relates V with A. Using  $A/V = M/L \times 6$  relation, the power function can be also formulated to  $\log(V) = -2.64 \times \log(M) + 2.64 \times \log(L) + 0.06$ , which interrelates V, M, and L. Similarly, the data for the near-sphere group can be also fitted to  $V = (A/V)^{-2.99} \times 116.26$  and can be further formulated to find the other relations.

Considering the general relation between V and A for any geometry can be expressed as  $V = A^{3/2} \times \lambda$ , where  $\lambda$  is a geometry constant, the relation between V and A/V can be formulated to  $V = (A/V)^{-3} \times \beta$ , where  $\beta = 1/\lambda^2$ . Therefore, the power value of the A/V and V relation is invariantly -3 for a group of particles with an identical morphology. For example, the power value is identically -3 for each group of spheres, cubes, tetrahedra or

whatever morphology as far as all particles in the group have a same look. (The particles in the group, of course, will be in different sizes, otherwise the A/V and V relation will be plotted single data point in the 2D plot space). If the relation between V and A/V of particles in a group can be generalized to  $V = (A/V)^\alpha \times \beta$ , any deviation of the  $\alpha$  value from -3 can indicate the degree of morphological heterogeneity of a given particle group. For example, the  $\alpha$  value of the near-sphere group is -2.99, which is practically -3, because the morphology in that group is nearly identical. On the other hand, the  $\alpha$  value of the mixed morphology group is -2.64, and the farther deviation from -3 indicates a broader spectrum of morphology in the particle group.

The  $\beta$  values can be analytically defined for some known geometries, e.g.,  $V = (A/V)^{-3} \times 36\pi$  for a sphere, where the  $\beta$  value is  $36\pi$  (~113.10). The  $\beta$  values of icosahedron, cube, and tetrahedron are 136.46, 216, and 374.12 respectively, which increases with geometric angularity. Therefore, the  $\beta$  value (i.e., the intercept in the log-log space) may imply a characteristic of the representative morphology for a given particle group. It is noted that the  $\beta$  value of near-sphere group is 116.26 which is close to that of a group of spheres (i.e., 113.10), and the  $\beta$  value of mixed morphology group is 129.66, which is higher than that of the near-sphere group. While further investigation of these  $\alpha$  and  $\beta$  values defined in the A/V and V space is beyond the scope of this study and left for future research, the  $\alpha$  value may imply the morphological heterogeneity and the  $\beta$  value may give a hint of the representative particle morphology in particle group, which will provide another interesting interpretation to the characterization of geometry parameter distribution.

The A/V distributions are evaluated by both the number and volume of particles and plotted in terms of the cumulative percentage in Figure 3.7e. The sample particle's corresponding



cumulative percentages are marked in green in Figure 3.7e. Both plots by the number and volume of the particles depict that the near-sphere group maintains a higher cumulative percentage given an A/V ratio, in other words, a lower A/V ratio given a cumulative percentage. This is because the particle morphology in the near-sphere group is near-equidimensional and round, which makes the A/V ratio smaller, so the A/V plots are located on the left of those of mixed morphology group. Compared to the cumulative percentages by the number, the difference in the plots by the volume is much smaller, because the small particles in the mixed morphology group have a higher irregularity thus a higher A/V, while the large particles in both groups have overall similar morphology. Therefore, Figure 3.7e shows the cumulative percentages by the volume are similar up to 60%. This is supported by Figure 3.7f, where the M distributions are shown in terms of cumulative percentage by the volume. As shown in Figure 3.7f, the M distributions between the two groups are overall comparable up to 60%, meaning 60% of particles by volume have a similar morphology.

### 3.4 Experimental Demonstration of Predictive Capability

#### 3.4.1 Specimen Preparation for Laboratory Direct Shear Test

Experimental study is performed to demonstrate the predictive capability of the proposed formula to estimate the influence of particle geometry. A set of 3D particle models are developed and 3D-printed for use in the direct shear test instead of using mineral particles to explicitly control the geometry parameters. The Krumbein and Sloss chart (Figure 3.8a) is referenced as the particle image library that is evaluated in terms of Sphericity and Roundness. Particles are numbered in ‘row # – column #’ format for convenience. The far different four morphologies at the corners in the chart, i.e., 1-1, 1-5, 4-1, and 4-5, are

selected for the 3D particle development. The Fourier descriptor-based modeling technique using solid of revolution, morphing and stretching is used to generate a realistic 3D particle model from the 2D cross-sectional images [114]. The developed 3D models are shown in Figure 3.8b with the evaluated M for each model.

The particle 4-1 is the most irregular among the four morphologies and therefore has the highest M value of 2.71. The irregularity evaluated by M (3D descriptor) is in order of 4-1 > 4-5 > 1-1 > 1-5 (i.e.,  $M = 2.71 > 1.96 > 1.36 > 1.08$ ). Regularity  $\rho$  (2D descriptor) is also evaluated, and  $1/\rho$  is shown in the figure. The irregularity evaluated by  $1/\rho$  is in the order of 4-1 > 1-1 > 4-5 > 1-5. Both M and  $1/\rho$  estimate the particle 4-1 is the most irregular, and 1-5 is the opposite. However, the order of 1-1 and 4-5 is different. It appears that  $1/\rho$  estimates the contribution of the particle 1-1's angularity (at the intermediate scale) is higher than the particle 4-5's elongation (at the global scale), while M estimates the contribution of the particle 4-5's elongation is higher. The Krumbein and Sloss chart represents a spectrum of mineral particle morphologies. Therefore, it is anticipated that the upper bound of M value for the mineral particles is about 3, which indicates a highly irregular morphology that may exist in nature.

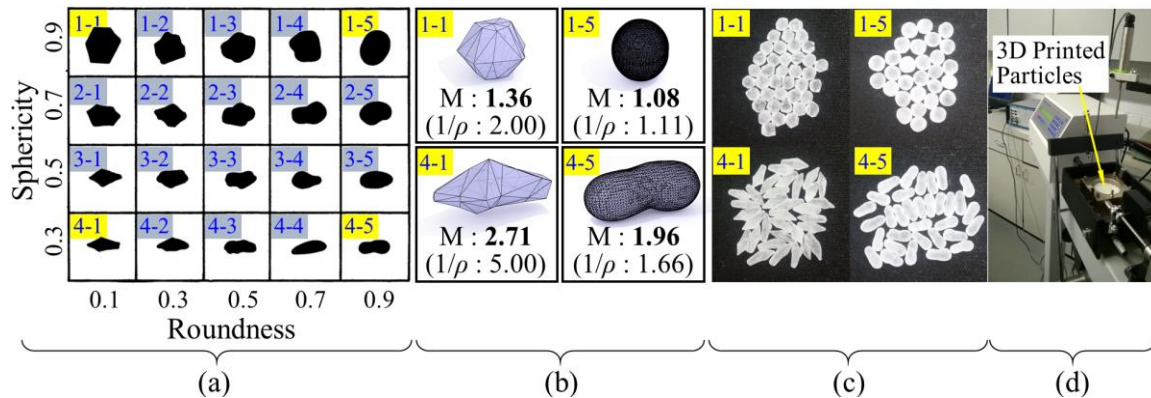


Figure 3.8. Development of 3D particle models and 3D printed particles; (a) Representative 2D morphology of typical mineral particles evaluated in terms of Sphericity and Roundness, modified from Krumbein and Sloss [111]; (b) Developed 3D particle models, and the quantified morphology and the inverse of Regularity; (c) 3D printed particles of the four models; (d) Direct shear test setup.

The developed 3D particle models are then 3D printed (Figure 3.8c) for laboratory direct shear test (Figure 3.8d). Form 1+ Stereolithography (SLA) printer is used for the 3D printing [115]. Particles are printed in 50 microns of layer thickness. Therefore, the surface texture of printed particles is controlled because the particles are printed using the same material at the same printing resolution. The compressive strength and the elastic modulus of the printed objects utilizing the Formlabs resin are reported in Watters and Bernhardt [116] and Zguris [117], which are roughly comparable to those of Florida limestone [118]. The cylindrical shear box size is 63.5 mm (2.5 in) in diameter  $\times$  37 mm (1.5 in) high. Each particle model is scaled to have the same volume ( $11.67 \text{ mm}^3$ ) such that a same number of particles can be considered per test specimen.

Each specimen of particles 1-1, 1-5, 4-1, and 4-5 is uniformly graded, i.e., composed of identical particles of same morphology, volume, surface area, and size. The initial void ratio is controlled to about 0.73 for the testing. The evaluated geometry of all four

specimens are shown in Figure 3.9, where the evaluated  $1/\rho$  is also plotted for comparison. As the four particle models are controlled to have the same volume ( $11.67 \text{ mm}^3$ ), it is obvious that the particle size increases with the morphological elongation and angularity. Consequently, the near-spherical particle 1-5 is the smallest as 3.05 mm, while the most irregular particle 4-1 is the largest as 5.97 mm. Therefore, M and L increase together in the order of 1-5, 1-1, 4-5, and 4-1 as shown in Figure 3.9a. A similar tendency is shown for  $1/\rho$  except for the particle 4-5 that is out of the trend, i.e.,  $1/\rho$  decreases while L increases. Figure 3.9b depicts the combined description of A/V and V, where the same trend is observed in order of 4-1 > 4-5 > 1-1 > 1-5 from the largest A/V. Likewise, the same order is estimated for the surface area A because all particles have the same V. Considering the trend in the evaluated M and the other geometry parameters in order of 4-1 > 4-5 > 1-1 > 1-5, the same trend of the mechanical performance such as shear strength and modulus is anticipated from the laboratory test.

Table 3.1 shows the maximum and minimum void ratios that can be obtained for the four specimens. The particles are poured in a circular motion using a funnel onto the shear box, and tamped in layers if necessary, to achieve the initial void ratio through trial and error process. The deposition of particles is randomly done, so the specimens' fabric is not controlled. The corresponding relative densities for the void ratio of 0.73 are also summarized in the table. While the initial void ratios of all specimens are controlled to be the same, particle 4-1 is relatively dense, and the other particles are relatively loose. The adopted particle sizes conform to the requirement of ASTM D3080/D3080M [119]. The specimens are tested at four different normal stresses, 40.5, 102.5, 164.4, and 226.4 kPa. The rate of shear is maintained at 1 mm/min.

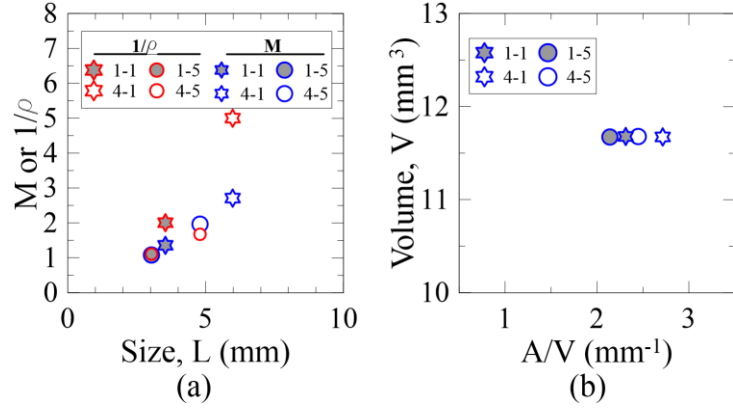


Figure 3.9. Evaluated geometry parameters for the four particle specimens; (a) Description of morphology and size using M and L as well as  $1/\rho$  and L; (b) Description of A/V ratio and V.

Table 3.1. Ranges of void ratio for each specimen and the relative densities  $D_r$  for the void ratio  $e = 0.73$

Particle #	$e_{min}$	$e_{max}$	$D_r$ (%)	Particle #	$e_{min}$	$e_{max}$	$D_r$ (%)
1-1	0.58	0.73	~0.00	1-5	0.62	0.76	21.42
4-1	0.70	0.87	82.35	4-5	0.59	0.73	~0.00

### 3.4.2 Test Results and Discussions

Each test is repeated three times, from which average response is obtained to eliminate the influence of initial particle arrangements [47,120]. No significant particle breakage or deformation is found at the end of tests, but some particle corners are chipped off. Therefore, the specimens are inspected after each test, and the chipped particles are replaced with new ones. Figure 3.10a-h show the average responses of shear stress and vertical displacement at the four different normal stresses. Data from each individual test is provided in Appendix B. While limited stick-slip fluctuation is shown in the test, the observed mechanical behavior is overall consistent in order of  $4-1 > 4-5 > 1-1 > 1-5$  from

the highest to the lowest shear strength and modulus as shown in Figure 3.10a-d. The friction angles evaluated from the shear stress responses are shown in Figure 3.11, which clearly shows the strengths in the order.

A similar trend is shown for the vertical displacement in Figure 3.10e-h with the specimen of 4-1 showing the highest rate of dilation. The nature of specimen 4-1's vertical displacement is also different from the other specimens: the vertical displacement of 4-1 increases continuously while the responses of other specimens are relatively flattened out. The difference in the displacements is possibly attributed to the different relative densities of the specimens as shown in Table 3.1. A higher range of void ratio is typically obtained with higher particle irregularity as broadly evidenced in the literature [6,121,122]. Despite the initial void ratio in all specimens controlled to 0.73, it is observed the relative density of specimen 4-1 is about 82% (i.e. relatively dense), while those of the other specimens are less than 21% (i.e., relatively loose). Therefore, the specimen 4-1 is able to continuously dilate while being sheared. The dilation angles are shown in Figure 3.12, which are computed based on the vertical and horizontal incremental displacements at the peak strength state. A trend of higher dilation is also shown in the same order of 4-1 > 4-5 > 1-1 > 1-5.

The test result demonstrates that the proposed approach can reasonably relate the particle scale information to the macroscopic mechanical property by its order and corroborates its predictive capability to estimate the influence of particle geometry effect. All the particles used in this study pass through 4 mm sieve and are retained in 2 mm sieve. The conventional Unified Soil Classification System classifies the coarse-grained particles in terms of particle size only using the sieves, thereby the specimens in this study are

classified as a same soil despite the significant differences shown in the test results. This research finding indicates the current specification remains to be significantly improved for enhanced soil classification.

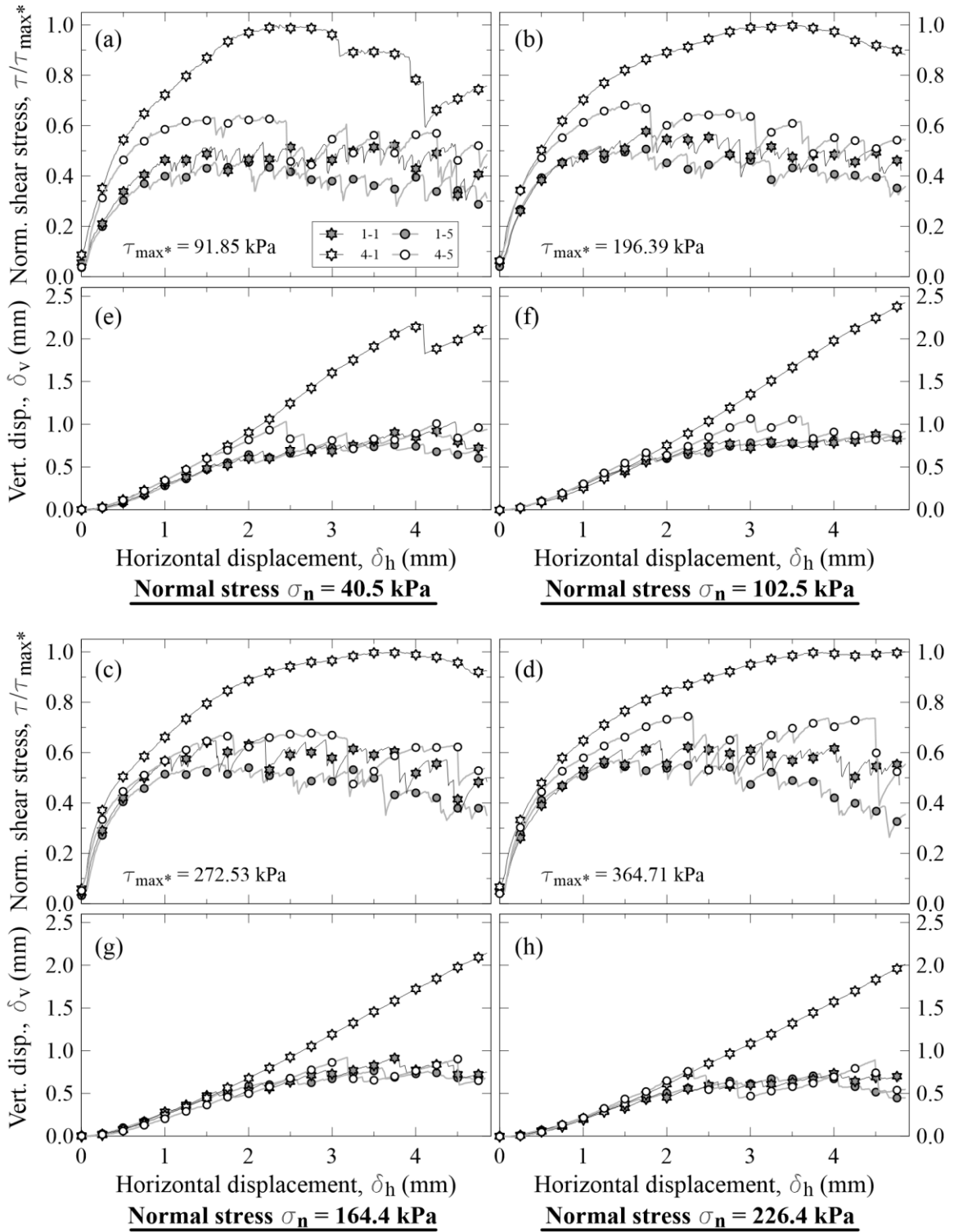


Figure 3.10. Direct shear test result: stress-strain curves and vertical displacements obtained at four different normal stresses (40.5, 102.5, 164.4, and 226.4 kPa); where the



stress-strain curve in (a) to (d) is normalized by  $\tau_{\max}^*$ , maximum shear stress obtained from the specimen 4-1.

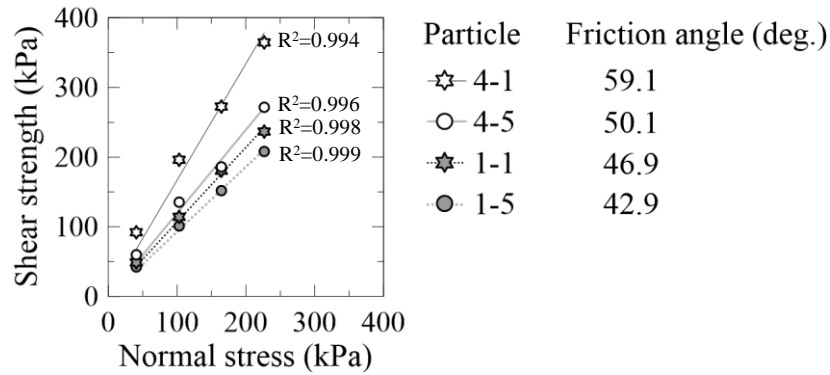


Figure 3.11. Friction angles evaluated from the fitting lines of shear strengths.

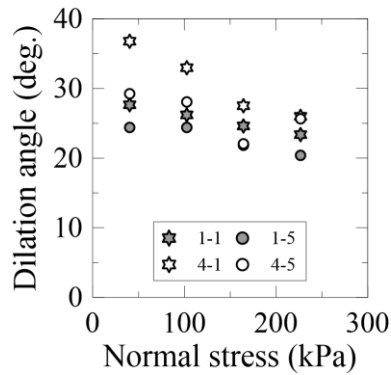


Figure 3.12. Dilation angles evaluated at the peak strength state.

### 3.5 Concluding Remarks

This study proposes a new formula,  $M = A/V \times L/6$ , that interprets the 3D particle morphology  $M$  as a function of the other geometry parameters, i.e., surface area  $A$ , volume  $V$ , and size  $L$ . Therefore, this MArVeLously simple formula clearly unravels the interrelation of  $M$ - $A$ - $V$ - $L$  by considering  $A$ ,  $V$ , and  $L$  as a set of ‘morphology parameters.’

This approach enables to conduct straightforward 3D particle morphology characterization using the simple formula. If one knows  $A$ ,  $V$  and  $L$ , then morphology can be evaluated in terms of  $M$ , which is much easier than conventional approach that separately evaluated the

morphology in addition to the information of A, V, and L. With the new formula, it is possible to comprehensively describe the four-dimensional aspects of the 3D particle geometry parameters in 2D plot spaces where the individual contributions of A, V, and L (as the morphology parameters) to M can be retrieved. Therefore, this approach is complementary to the conventional approach as it helps to consider the four geometry parameters' combined influence on the behavior of granular materials. This study will contribute to enhance the predictive capability, effective aggregate quality control and proactive planning for the optimal maintenance in the field of transportation geotechnics.

A challenge of applying the proposed approach to the engineering practice may be concerned with measuring the surface area of mineral grains. This measurement can be performed by using the 3D optical characterization techniques such as photogrammetry. Notwithstanding such techniques are computationally expensive at the moment, the proposed approach is sustainable in the sense that the 3D optical characterization techniques become more accessible and affordable with newer generations of imaging equipment and the advances in image processing algorithms.

## 4 A NEW FRAMEWORK TO ESTIMATE THE COARSE AGGREGATE 3D GEOMETRY USING OPTICAL GEO-CHARACTERIZATION

### 4.1 Introduction

#### 4.1.1 Background

The comprehension and analysis of 3-dimensionality of particle geometry is a complex phenomenon and have been a challenge for both academic and practitioner communities for a long time. Particle 3D analysis was first made possible with the invention of X-Ray Computed Tomography (XRCT). XRCT uses X-ray absorption by the object to accurately describe its 3D volume map. It is the fastest method as several touching particles can be scanned together. It generates a detailed volume mesh where other scanning techniques (such as laser scanning, photogrammetry etc.) only provide a surface mesh. This is also useful in detecting any void inside of the particle. XRCT has been used extensively to investigate the particle morphology, grain packing, in-situ movement of grains during shearing, particle breakage, strain localization of shear band etc. [8,9,123].

XRCT gives 3D voxel-based volume mesh which requires complex 3D analysis using sophisticated mathematical methods such as Fourier series or spherical harmonics analysis [55,56,124] to convert them to polyhedron surface meshes. Due to computationally expensive mesh generation, requirement of heavy and expensive machinery and lack of portability, XRCT technique is far too complicated for field adaptability. For this reason, simplified analysis using 2D images has gained much more popularity even though they do not accurately describe the particle geometry. The most common method of 2D geometric analysis is to take particle images with even lighting and monochromatic

background in either static or dynamic method [49,125]. In static method particles are placed on a stationary tray [41] and in dynamic method particles are placed on a conveyor belt [126] or poured in a chamber with camera arrangement [54]. After the images are captured, the particle outline is extracted using different image analysis techniques. This boundary information is used to compute different geometric properties such as area, perimeter, maximum size, convex hull etc. One of the disadvantages of these methods is their 2D nature. When the particles are placed on a tray, only the most stable face is visible from top. This one projection may not be representative and could be with complete disagreement with other projections. For example, two of the three major perpendicular projections of an ellipsoid are ellipses but the third one is a circle. Also, these 2D definitions cannot be directly extended to 3D, for example, 3D roundness is not well defined. Another major disadvantage is separate characterization of size and morphology where valuable information is lost regarding how they are interrelated.

This dissertation proposes M-A-V-L concept which is based on the interrelation between different geometry components. As shown in Chapter 3, M-A-V-L systematically characterizes 3D particle geometry while providing accurate correlation with macro-scale shear strength properties. The practical implementation of this method involves obtaining particle geometry information. With the advancement in optical geo-characterization and leveraging the endless capability of modern computers, it is easy to obtain a complete 3D model of any object by 3D scanning. In this study, particle 3D scanning is leveraged as a suitable alternative to traditional methods of measurement such as caliper measurement and 2D image processing.

There are several technologies available for 3D scanning with their own advantages and disadvantages. The most sophisticated and expensive one being XRCT [55,56] as mentioned earlier. It is most suitable for scanning microscopic sand sized particles where most other 3D scanning techniques fail. However, very large size boulder particles cannot be scanned by this method due to limitation in equipment dimension. In laser triangulation 3D scanning method, a point or line source of laser is emitted [127]. As the laser hits the object the reflected laser is captured by a sensor located inside the scanner. Based on the angle of the reflected laser the accurate location of the point in the object is determined. A complete 3D point cloud of the object is obtained once all the points have been successfully captured.

A structured light scanner (SLS) projects a set of DLP (digital light processing) patterns on the object and cameras mounted at specific distances captures those patterns [108]. 3D meshes are generated depending on the distortion of the light patterns by the object. SL scanners are reportedly faster and more efficient in capturing intricate details than laser triangulation scanners. Photogrammetry method of scanning particles is gaining popularity because it only requires a camera (including smartphone camera) and some free software [57,100]. This method consists of taking multiple pictures of an object from all possible latitude and elevation. The photogrammetry software finds overlapping points from 2 or more photos and determines its coordinates. Clearly, more number of photos will enhance the quality of the scanned model. This method is cost effective and can be used to scan particles on site. This can be used on large-size particles which are difficult to be transported to laboratory set up. Although photogrammetry is not suitable for scanning

microscopic particles due to limitation in camera capability, the present study shows that it can be easily used to scan up to ~20 mm particle.

#### 4.1.2 Objective and Scope

The objective of this study is to investigate if the power law relationship in M-A-V-L holds true for naturally occurring mineral particle geometry as observed theoretically in Chapter 3. This essentially requires scanning particle 3D geometry to obtain A, V and L information. In this study, a set of mineral particles have been 3D scanned using highly accurate SL 3D scanner. Then a subset of these particles is scanned using cost effective photogrammetry technique. Since SL scanner is calibrated using actual length dimensions, the scanned models are automatically scaled to the actual size of the particles, i.e. the ratio of scanned model to real object is 1:1 [128]. Hence the geometry data such as volume and surface-area-to-volume-ratio obtained in this method is directly used to obtain the power law function using M-A-V-L concept. But photogrammetry 3D models are not scaled to real size, as a result the size information is lost in the photogrammetry models. Hence the sizes of the actual particles are measured using a caliper and the models are scaled to match the caliper-measured size. Then V and A/V information is extracted to obtain the power law equation. A comparison of these two methods is provided with their advantages and disadvantages. Finally, an additional set of 8 particles are scanned to validate the obtained power law equation. These 8 particles set are deliberately chosen from different size groups in order to validate the power law across different size.

## 4.2 Particle Sampling and Scanning using SL scanner

### 4.2.1 Particle Sampling

A set of 60 crushed Florida limestone particles are randomly sampled. The set is comprised of particle from 2 different size groups: large ASTM #4 (sieve size 19 mm to 37.5 mm) and intermediate ASTM #57 (sieve size 4.75 mm to 25 mm) [129]. Different sizes were chosen to demonstrate the capability of the scanner to scan both large and small size particles. Figure 4.1 shows the photo of 60 particles scanned using SL scanning. The particles have extremely irregular surface features, the surfaces are whitish, matte and not reflective. Previous studies [100,127] have focused on scanning granite aggregates having a colored texture with high contrast, less surface pores which are believed to have acted favorably towards the success of the scanning method. On the other hand, Florida limestone has monochromatic, matte, white texture with porous surface which is less reported in literature and hence chosen in this study.



Figure 4.1. 60 particles used in SL scanning.

#### 4.2.2 SL Scanning

For this study, an HP 3D Structured Light Scanner Pro S3 is used. It uses a high-resolution dual camera set up and a projector mounted on an aluminum sliding rail along with an automatic turntable capable of 360-degree rotation. The instrumental set up is shown in Figure 4.2. Below are the steps followed to set-up and scan the particles:

The projectors and both the cameras are mounted on the sliding rail. The camera is set approximately at an angle of  $20^\circ$  with the projector. The particle is placed on the turntable and projector is turned on and focused so that the striped DLP patterns on the object are



not blurred. Both the cameras are slid and rotated to position along the sliding rail to have the object in view. The camera focal length is adjusted such that the object is clearly visible in the camera view screen. The object is then removed, and the calibration board is positioned in place of the object. 60 mm scale is used for calibration of the 60 particles in this study. A checker board pattern appeared on the calibration board after successful calibration. This calibration using actual dimensions enables the scanner to capture the real size of the object.

After calibration is performed, the calibration board is replaced with particle. Particles are placed on the tip of a needle bed in order to capture entire surface features (Figure 4.3a). Particles are rotated a full 360 degrees with scanning taking place at every 10 degrees, i.e. a total 36 scans from 36 different angles are captured. These 36 scans are fused together using the HP 3D Scan 5 software to make a single object. A resolution of 500 (no unit) was selected for all particles which means that the distance between two vertices of each particle scan were  $\sim 0.5-0.25\%$  of the size of the particle. Selection of this value of resolution limits the scan file size to  $\sim 250-450$  MB per particle. Selecting a higher resolution value ( $>500$ ) makes the distance between the vertices smaller resulting in a finer mesh and a larger file size. But this has no significant impact on the surface area, volume and size of the particle. The cost of the entire scanning device kit is around \$6950. The reported measurable size range for this scanner is  $\sim 10-600$  mm with the camera resolution of 1920x1200 HD. The scanning resolution is  $\sim 0.05\%$  of the scanned object size.

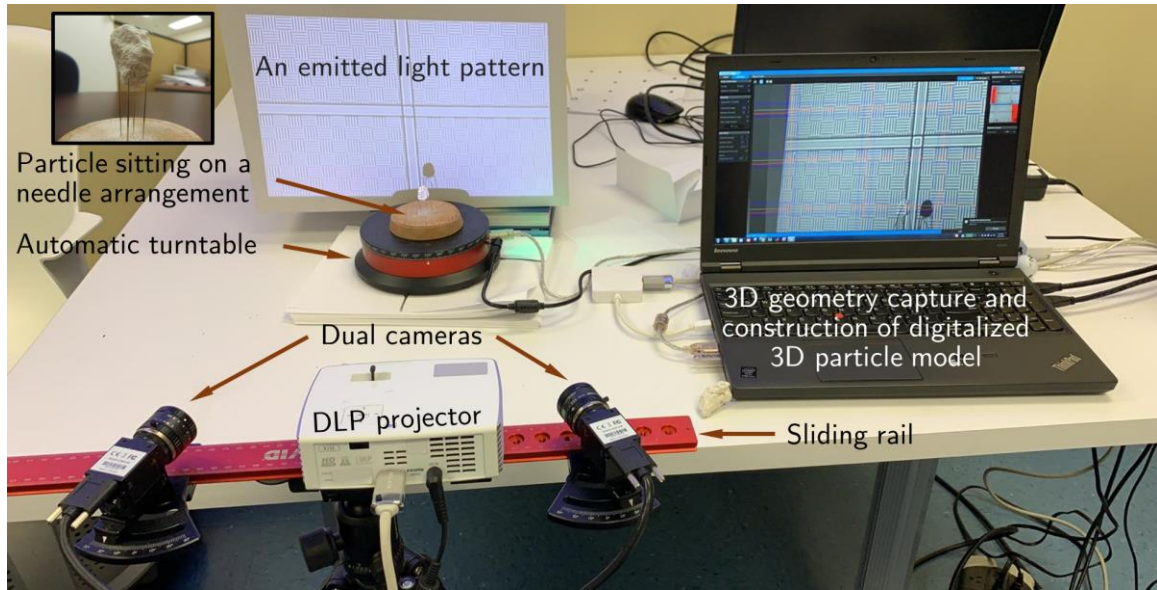


Figure 4.2. HP SL Scanner Setup.

Since the particles are very irregular in shape, in order to verify that the scanned models correspond to the real particle in dimension and the measured values are correct, a ball (Figure 4.3a and b) which has regular shape and known dimensions is scanned. The dimensions of the ball are measured in 3 perpendicular directions using a caliper and validated against the measurement obtained from the scanned 3D model. These two measured values are found to match closely with each other. Hence the scanned models are dimensionally proportional to the real particles.

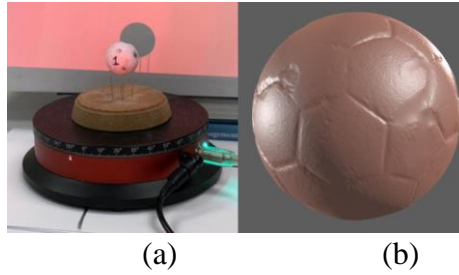


Figure 4.3. Scanning a regular shaped object in order to validate the dimensional proportionality: a) the ball mounted on the turntable by a needle arrangement; and b) scanned 3D-model of the ball.

### 4.3 Scanning Particles using Photogrammetry

30 particles out of the 60 particles originally scanned in SL scanning method has been scanned using photogrammetry method. An affordable digital camera, Nikon Coolpix S6300 (16-megapixel resolution) with a 10× optical zoom Nikkor lens is adopted for the 3D imaging of the sampled particles. Lee *et al.* (2019) tested the sensitivity of the evaluated particle morphology to the camera resolution. They concluded overall good comparison was found up to 5% of difference in the evaluated morphology obtained from photos taken using 8, 12, and 24-megapixel cameras, which corroborates the use of 16-megapixel resolution is a reasonable choice. Each particle is mounted on an arrangement of 4 needles to also scan the particle's bottom (Figure 4.4a). Photos are taken in a normal office room setting with regular ceiling lights and background. A total of 240 photos (4608×3456 pixels) are taken for each particle from different orientations (Figure 4.4b). The particle and the surrounding background remain stationary during the 3D imaging. The 240 images are taken to make sure the local details of surface morphology can be captured, in particular, for the small to intermediate (ASTM #57) aggregates. The photos are also taken such that some significant overlap can be made in the background to better stitch the images

during the photogrammetry reconstruction. It takes about 15 mins to capture the 240 photos, and about a day to complete the 3D imaging of all 30 particles.

All the photos are then fed to photogrammetry software for 3D reconstruction of particle geometry, for which this project adopts VisualSFM, freeware using the structure from motion photogrammetry technique [130]. VisualSFM first performs a series of pairwise photo matching to identify overlap in the loaded photos followed by the sparse 3D reconstruction (Figure 4.4c). Then the CMVS package, an add-on to VisualSFM, is used to perform the dense reconstruction (Figure 4.4d) from which dense point cloud is generated [131]. Lastly, high-fidelity 3D particle model is developed with surface mesh based on the point cloud (Figure 4.4e), for which this study adopts MeshLab, an open source 3D mesh processing system equipped with a set of surface reconstruction algorithms [132]. The Poisson surface reconstruction is selected among the built-in algorithms, which provides a high degree of modeling fidelity over the reconstructed surface [133].

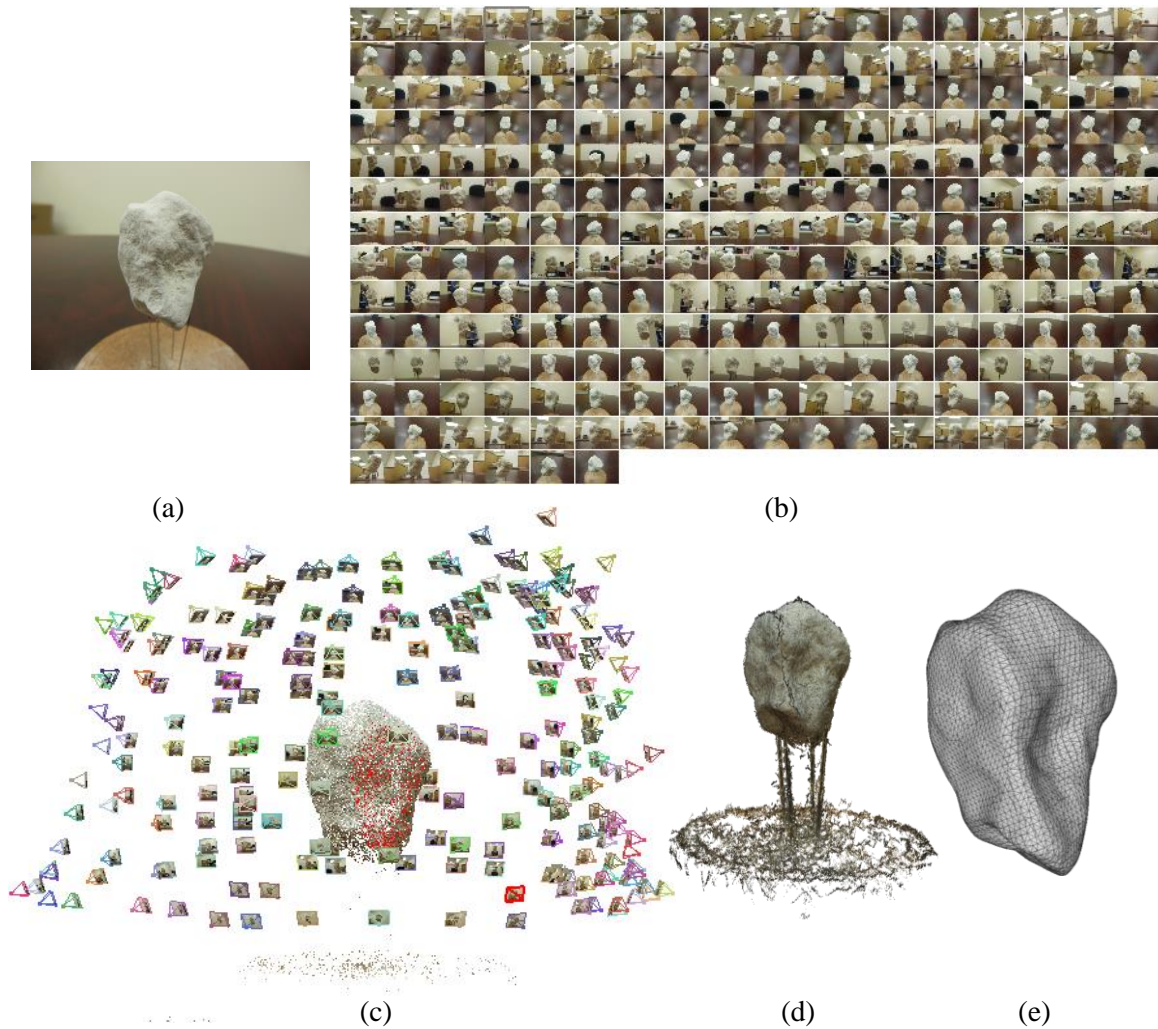


Figure 4.4. 3D imaging and photogrammetry reconstruction of a particle: (a) Particle sitting on the arrangement of 4 needles; (b) 240 photos taken around the particle; (c) Sparse reconstruction; (d) Dense reconstruction; (e) Generated 3D particle geometry.

#### 4.4 Measurement of the Geometric Properties from the Reconstructed 3D Particles

The 3D models obtained in SL scanning are shown in Figure 4.5. These 3D models are automatically in the same scale as the real particles. The reconstructed 3D particles using photogrammetry method are shown in Figure 4.6. In photogrammetry technique, the actual scale information is lost. Hence, particles scanned using this method is scaled to match the volume of the corresponding SL scanned models. Then surface area and size are obtained

from the scaled 3D models. To obtain volume and surface area, Blender 3D-printing add-on has been used [134]. Size is measured in terms of the diameter of the circumscribing sphere, which is computed using a Matlab code [135].

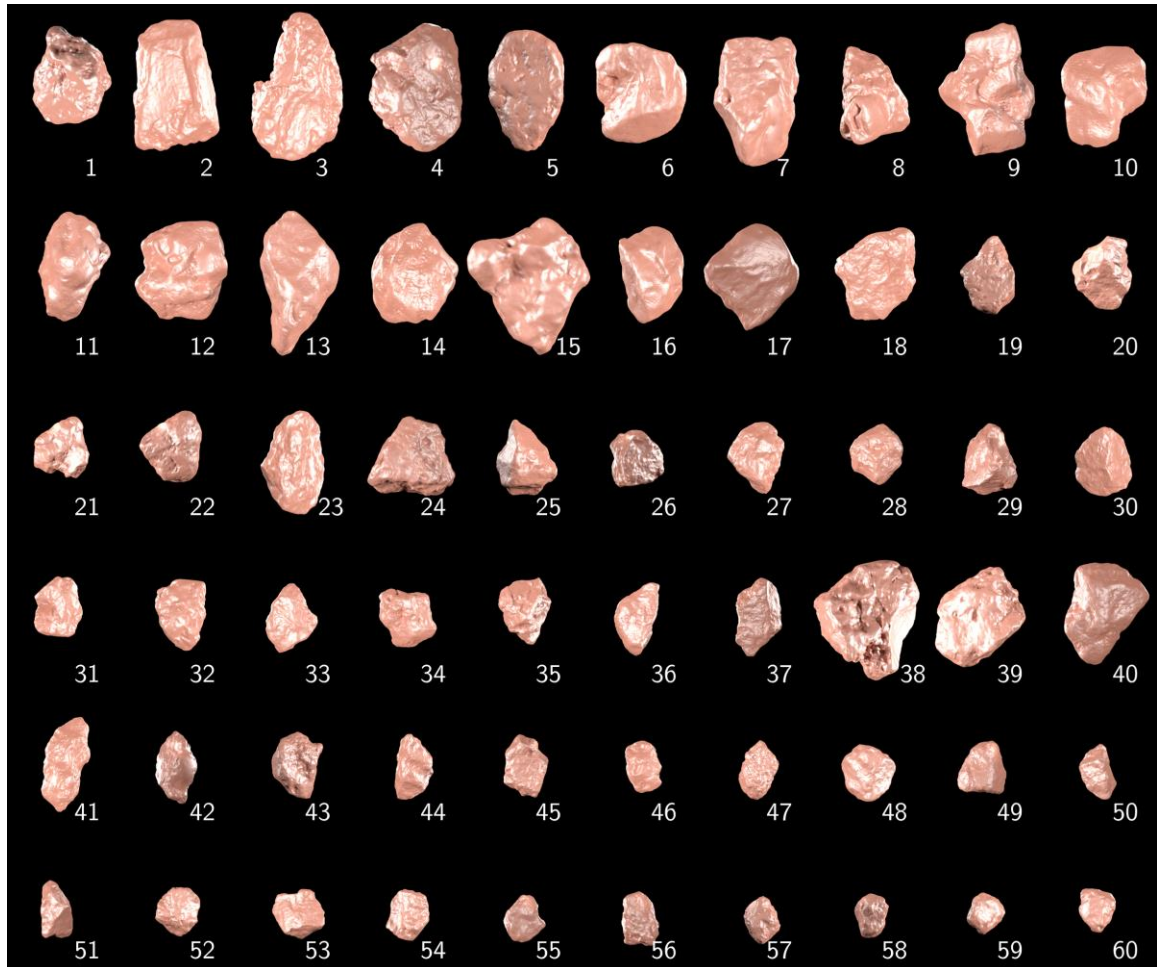


Figure 4.5. 60 particles 3D models scanned using SL 3D scanner.



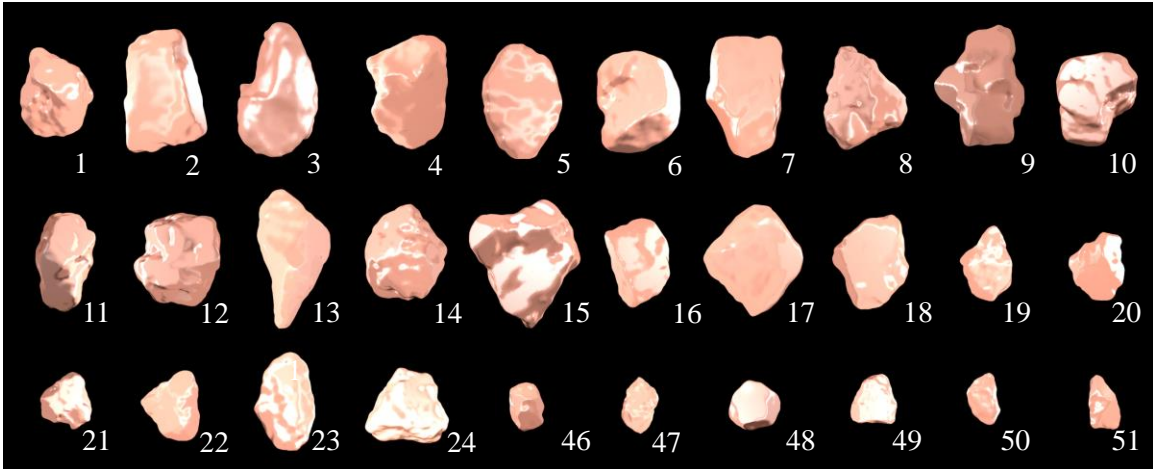


Figure 4.6. Reconstructed 3D particle geometry based on 240 photos each using photogrammetry method.

#### 4.5 Comparison of Power Law Functions Obtained from the 2 Scanning Techniques

The geometry information obtained from the 3D models can be used to obtain the power law relationship. The log-log scale plot for  $V$  vs.  $A/V$  for 60 particles scanned in SL scan method and 30 particles scanned in photogrammetry method are shown in Figure 4.7a. As expected, the relationship between  $V$  and  $A/V$  of the particles is shown as a straight line in the log-log space. The equation of power law function obtained from 60 SL scanned particles is  $V = (A/V)^{-3.177} \times 180.46$  and the equation of the same obtained from 30 photogrammetry scanned particles is  $V = (A/V)^{-3.167} \times 162.33$ . The coefficient of determination for SL scanned samples is 0.99277 and for photogrammetry scanned samples is 0.992198, they are basically comparable. The  $\alpha$  and  $\beta$  values (introduced in Chapter 3) for the limestone particles are 3.18 and 180.46 (using SL scanning) respectively.  $\alpha=3.18$  indicates that the distribution is not morphologically homogeneous and  $\beta = 180.46$  indicates that the representative morphology is between icosahedron and cube. Figure 4.7b

shows the morphology vs size plot for M values obtained in these two different scanning techniques. Here photogrammetry scanned particles are scaled to have the same volume as the SL scanned particles as mentioned previously. Figure 4.7 gives the inter-related 2D morphology space. Different geometry property values for 60 SL scanned particles and 30 photogrammetry scanned particles are provided in Appendix C, Table C.1.

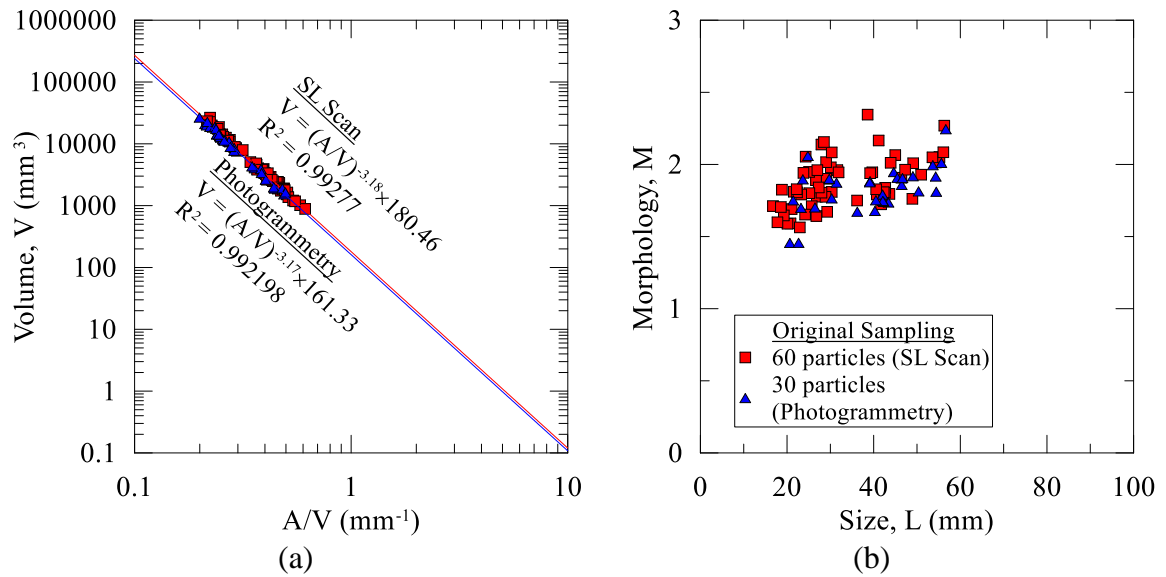


Figure 4.7. (a) V vs. A/V plot for 60 particles scanned using SL scanning method and for 30 particles scanned using photogrammetry method; (b) M vs L plot for 60 particles scanned using SL scan and 30 particles scanned using photogrammetry.

#### 4.6 Validation of Power Law from SL Scanning and from Photogrammetry

The power law fit curve is the key for estimation of A/V from V. Another set of 8 particles is selected for validation from the same limestone aggregate batch where the 60 particles were sampled (Figure 4.8). The size of 7 out of the additional 8 particles is <10 mm and one is ~95 mm. Different size for validation particles are deliberately chosen to investigate the accuracy of the power law function for smaller sized particles the scanning of which is more difficult using surface scanning method. Figure 4.9a shows the actual V vs. A/V plot



of the 8 particles, obtained from the SL scanning of the 8 particles. Using these V values, A/V is also estimated from the two power law equations. A good comparison is shown with the estimated A/V ratios in both scanning methods, which also corroborates the power law relationship across the sizes. Figure 4.9b shows the M vs. L plot differentiating the size and morphology of the 7 small particles and 1 large particle. Table 4.1 shows the estimated and measured A/V values of the 8 particles, where a good comparison is also shown. The % difference in the measured A/V values and the estimated A/V values leveraging the two power law equations is small and ~5%. This shows the fidelity of using the power law equation to estimate A/V from only V. This significantly reduces the scanning effort as particle volume can be measured indirectly e.g. using particle weight and specific gravity. In this study, SL scanned data have been leveraged to scale the photogrammetry models. In order to use photogrammetry alone, the size of each individual particle has to be measured using a caliper and the scanned models can then be scaled to the measured size. Geometry data for 8 additionally sampled particles are provided in Appendix C, Table C.2.

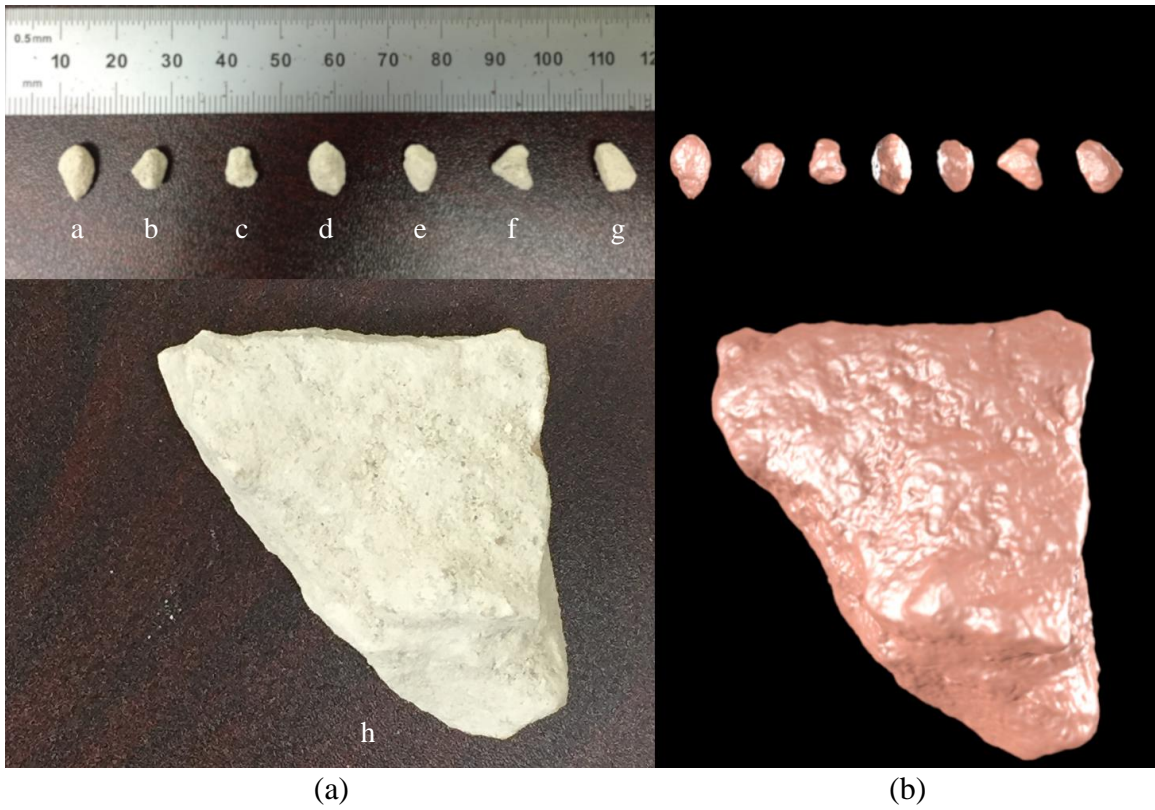


Figure 4.8. A set of 8 additionally sampled particles for validation of the power law relation between  $A/V$  and  $V$  of the Florida limestone aggregate: (a) Photo of the 8 particles; (b) Digitalized 3D particles obtained from the structured light scanning.

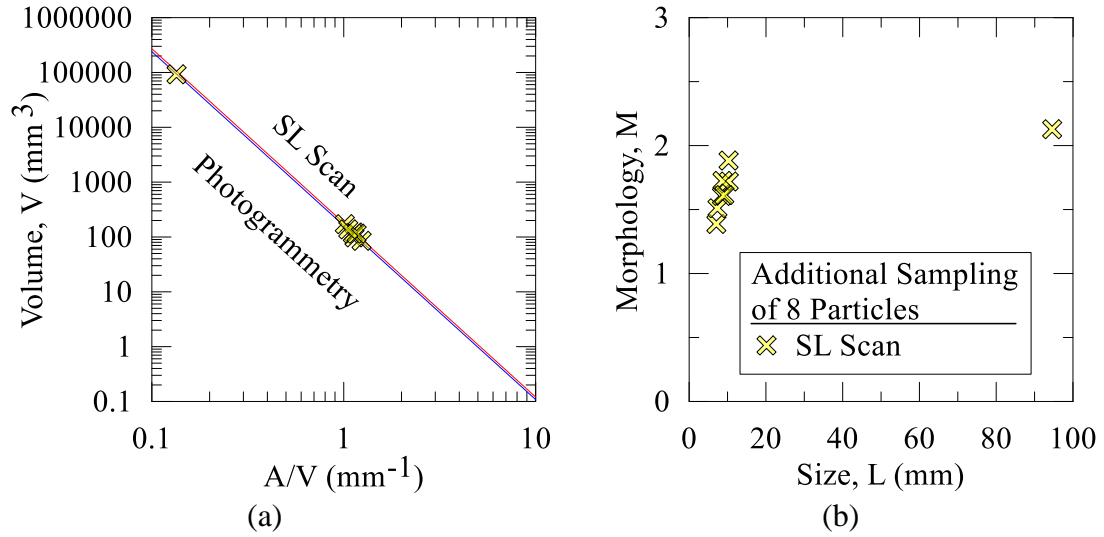


Figure 4.9. Validation of power law equation using 8 additionally sampled particles: (a)  $V$  vs  $A/V$  data obtained from SL scanning plotted along with power law functions obtained in SL scan sampling and photogrammetry sampling; (b) plot of  $M$  vs.  $L$ .

Table 4.1. Validation of power law equations using SL scan of 8 additionally sampled particles.

Particle #	V from SL Scanning ( $\text{mm}^3$ )	A/V from SL Scanning ( $\text{mm}^{-1}$ )	A/V from Power Law ( $\text{mm}^{-1}$ )		% Difference	
			SL Scanning	Photogrammetry	SL Scanning	Photogrammetry
a	119.939	1.133	1.137	1.098	0.349	3.107
b	98.395	1.136	1.210	1.169	6.548	2.697
c	85.090	1.238	1.267	1.223	2.330	1.167
d	171.181	1.013	1.017	0.981	0.397	3.072
e	114.887	1.115	1.153	1.113	3.355	0.207
f	114.752	1.166	1.153	1.113	1.116	4.582
g	137.460	1.055	1.089	1.052	3.242	0.319
h	92488.695	0.134	0.140	0.135	4.343	0.483

## 4.7 Concluding Remarks

The study in this chapter validates the power law for mineral particles. The power law function obtained from scanning a group of sample particles is leveraged to obtain  $A/V$  using only  $V$ . The power law relationship between particle  $V$  and  $A/V$  which was obtained theoretically before in Chapter 3 is also obtained for natural mineral particles. This power law function is an important characteristic of particle 3D geometry. It provides useful relation between particle 3D volume and surface area. This power law can be leveraged to quickly obtain particle 3D geometry information without scanning them. Particle volume can be obtained by measuring particle weight and specific gravity. Using volume and power law function, particle surface area can be measured. Hence this significantly reduces particle 3D scanning effort.

This study also demonstrates successful scanning of particles of up to  $\sim 7$  mm size using SL scanner and particles of  $\sim 20$  mm using photogrammetry. Scanning smaller particles less than  $\sim 10$  mm using photogrammetry requires expensive and powerful cameras. Scanning sand sized particles is not possible using photogrammetry method. Although it would be interesting to obtain the 3D geometry information of microscopic clay-sized particles, at this time it is limited by lack of proper optical geo-characterization equipment. This prediction method is extremely useful in measuring geometry values for small sized particles, the scanning of which is relatively more difficult.

This study also provides a comparison between two different scanning techniques: more expensive, highly accurate and non-portable SL scanning method and economic and portable photogrammetry method. The results show good agreement between these two estimated values which establish photogrammetry as a reliable method of 3D scanning

particles in field. In this study the photogrammetry successfully applied to limestone aggregates with monochromatic, matte and porous texture that was previously considered as unfavorable for scanning.

## 5 PREDICTION OF 3D SPHERICITY WITH VOLUME ONLY

### 5.1 Introduction

#### 5.1.1 Background

Particle shape is a key information to robustly establish a link between the underlying grain scale mechanisms and the macroscopic material properties of the bound and unbound aggregates widely used in the construction. There are vast number of literatures evidenced the particle shape effect on the macroscale properties such as void ratio, stiffness, peak and critical shear strength, dilation, etc. [5–13]. Therefore, major efforts have been made to better characterize the particle shape, for which several shape descriptors were developed in the research community [50,51,53,73,136], etc. However, these descriptors commonly quantify the 2D particle shape for convenience in the field inspection with the challenges in characterizing the shape in 3D.

A traditional 3D shape descriptor is the ‘true’ Sphericity  $\psi$  coined by Wadell [73] that characterizes the 3D particle shape in terms of the surface area as shown in Equation 5.1 below.

$$\psi = A_s / A \quad 5.1$$

where  $A_s$  is surface area of a sphere having the same volume with the particle of interest and  $A$  is surface area of the particle. It is worthwhile to note that the true Sphericity is not only an indicator of the overall particle form, e.g., how elongated the particle is, but also the particle angularity, i.e., overall sharpness of corners, because  $\psi$  is a function of the surface area that is influenced by both form and angularity [94,95]. The true Sphericity is

simple to use, as it quantifies the 3D shape with surface area, compared to other conventional descriptors that require complex geometry analysis even for 2D shape characterization [41,137]. However, the true Sphericity has not been popular in the engineering practice, ironically, due to the challenge of measuring the surface area. The recent advances in optical geo-characterization leveraging 3D scan, e.g., X-ray Computed Tomography (XRCT), Photogrammetry [55,57,100], enabled to facilitate capturing of 3D particle geometry by developing digital 3D model, which made the measurement of surface area more feasible as well as the volume, and in turn the true Sphericity. However, the 3D scanning requires some extensive time and high computational cost, which still makes hard to adopt the true Sphericity to characterize the shape distribution of aggregate with the necessity of scanning as many particles as possible to enhance the statistical significance.

#### 5.1.2 Objective and scope

The objective of this study is to introduce a new framework that can robustly estimate the true Sphericity of aggregate particles with a minimal effort of 3D scanning. The key of this new prediction approach is to leverage the relationship between the particle surface-area-to-volume ratio ( $A/V$ ) and the particle volume ( $V$ ) that can be approximated by a power law. Therefore, the surface area can be quickly estimated with volume only from the identified power law relation, and in turn the shape distribution of particles can be rapidly characterized in terms of the true Sphericity. Section 5.2 below discusses the power law relation between  $A/V$  and  $V$ , and Section 5.3 demonstrates the feasibility of this 3D Sphericity prediction framework on a set of mineral particles.

## 5.2 Power Law Relation between A/V and V

The relationship between A and V for any particle geometry can be expressed as  $V = A^{3/2} \times \lambda$ , where  $\lambda$  is a geometry constant, which can be easily understood as the particle surface area A is in squared length and the volume V is in cubic length. This  $V = A^{3/2} \times \lambda$  can be reformulated to  $V = (A/V)^{-3} \times \beta$ , which is a power function with a power value  $\alpha = -3$  and  $\beta = 1/\lambda^2$ . This formulation indicates the power value  $\alpha$  is identically -3 for sphere, cube, tetrahedron or whatever shape as far as the particles in the group have a same look (shape). Considering  $V = (A/V)^\alpha \times \beta$  can be represented as  $\log(V) = \alpha \times \log(A/V) + \log(\beta)$ , this power law relation between A/V and V is shown as a linear plot in the log-log space, where the power term  $\alpha$  corresponds to the slope of the log-log plot, and the constant term  $\beta$  corresponds to the intercept of the plot. The following therefore can be postulated:

- The  $\alpha$  value of the A/V and V relation is always -3 for a group of particles with an identical shape. Therefore, any deviation of the power value  $\alpha$  from -3 indicates the degree of shape heterogeneity, i.e., farther deviation of  $\alpha$  from -3 indicates more diversity of shapes in the particles.
- The  $\beta$  value can be analytically defined, e.g.,  $\beta = 36\pi$  (~113) for sphere (i.e.,  $V = (A/V)^{-3} \times 36\pi$ ),  $\beta = 136.46$  for icosahedron,  $\beta = 216$  for cube, and  $\beta = 374.12$  for tetrahedron, which increases with geometric angularity. Therefore, the  $\beta$  value implies a characteristic of the representative shape for a given particle group.

How  $\alpha$  and  $\beta$  varies with morphology distribution is an area of future study. This requires more 3D geometric data collection for construction materials across globe with inherent variability in grain geometry. Consequently, the  $\alpha$  and  $\beta$  values represent the geometric signature of a group of particles. Once the power law relation between A/V and V is



identified, and the A/V ratio of a particle for a given V can be quickly estimated. The true Sphericity  $\psi$  in Equation 5.1 can be reformulated as below with the consideration of the particle volume V, which is also the volume of the sphere by the definition of the true Sphericity:

$$\psi = (A_s/V) / (A/V) \quad 5.2$$

Therefore, for a given V, the corresponding A/V can be found from the identified power function. Computation of the surface area of sphere  $A_s$  is straightforward using the theoretical formula, i.e.,  $A_s = \pi^{1/3} \times (6V)^{2/3}$ .

### 5.3 Demonstration of the 3D Sphericity Prediction using the Volume Only

This section demonstrates the proposed 3D Sphericity prediction as follows: (1) A set of 60 particles are first sampled from a batch of Florida limestone construction aggregate; (2) An affordable 3D scanner, HP 3D Structured Light (SL) Scanner Pro S3 with dual cameras [138], is employed to capture the 3D geometry of the sampled 60 particles; (3) The obtained surface area A and volume V of the particles are used to identify a power law relation between A/V and V. The weights of the sampled particles are also measured to obtain the specific gravity of solids, which is for use later to estimate the volume of any particles in the aggregate by weighing. Eight other Florida limestone particles of different sizes are additionally sampled to see whether the power law holds true for the different sizes; (4) The true Sphericity of another 344 particles are then estimated using the volume. The weight of each particle is first measured, and then the volume V is computed using the specific gravity of particles. The corresponding A/V ratio is found from the power law function, and  $A_s$  is computed from the theoretical formula, whereby the distribution of the true Sphericity can be found.

### 5.3.1 Sampling of Florida Limestone Particles

A set of 60 particles are sampled from a batch of Florida limestone construction aggregate provided by the Florida Department of Transportation (Figure 4.1). The particles are whitish in color and have matte texture. These particles are randomly selected from two groups of different sizes: ASTM #57 (25.0 to 4.75 mm) and #4 (37.5 to 19 mm) aggregates.

### 5.3.2 3D Scanning of the Sampled Particles

The 3D geometry of the sampled 60 particles is captured through 3D scanning for which the Structured Light (SL) scanning is considered. An incentive of SL scanning is that it performs a scan at 1:1 scale. Therefore, the digitalized 3D particle produced by the SL scanning has the actual particle size, and there is no need to re-scale the digital particle to the manually measured size, e.g., using a caliper, which is the major difference from the single camera photogrammetry [128]. Consequently, the actual particle surface area and volume are also immediately obtainable. This study employs an affordable SL scanner, HP 3D Structured Light Scanner Pro S3 [138]. The SL scanner is equipped with dual high-resolution cameras and a Digital Light Processing (DLP) projector that can create a digital 3D model with up to 0.05 mm resolution.

The 3D scanning setup is shown in Figure 4.2, where the cameras and projector are mounted on the aluminum sliding rail and capture the 3D geometry of the particle on the automatic turntable capable of 360-degree rotation. The DLP projector emits a series of light patterns on the particle. As the patterns get distorted on the object, the two high-resolution cameras capture the changed patterns, based on which the companion software computes the 3D geometry and creates the polyhedral mesh. The automatic turntable is set to rotate at 10 degrees interval, which allows for scanning from all 360 degrees with a total

of 36 scans. The particles are placed on a needle arrangement mounted on the turntable to scan the whole surface including the bottom. Figure 4.5 shows the digitalized 60 particles. The SL scanning results in high-quality 3D polyhedral meshes with around a million triangular surface elements.

### 5.3.3 Characterization of the Power Law Relation between $A/V$ and $V$

The surface area  $A$  and volume  $V$  obtained from the digitalized 60 particles are utilized to identify the power law relation between  $A/V$  and  $V$ . Figure 5.1 shows the 60 data points (black squares) from the sampling, from which the relation is approximated by a power function,  $V = (A/V)^{-3.18} \times 180.46$ . The power value  $\alpha = -3.18$  implies some level of shape heterogeneity in the aggregate due to the deviation from -3. The intercept  $\beta = 180.46$  represents a shape with angularity somewhere between icosahedron ( $\beta = 136.46$ ) and cube ( $\beta = 216$ ). Since the all particle volumes are known, the specific gravity of solids can be computed with the weight measured. This specific gravity of solids then can be used later to estimate the volume of any particle selected from the Florida limestone aggregate by weighing. To this end, 30 particles are randomly selected from the 60 particles and then the weights are measured using a scale with resolution of 0.1 mg (Figure 5.2). The variation of solid density is typically small, thus fewer particles (i.e., 30 particles) are weighed. The average of specific gravity is 2.247 with a standard deviation of 0.107. The measured weights of 30 particles are provided in Appendix C, Table C.3.

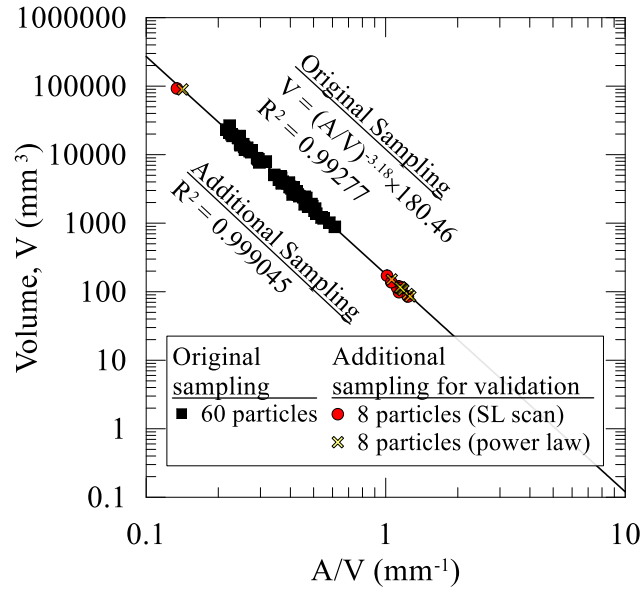


Figure 5.1. V vs A/V relationship for 60 sampled limestone particles (black squares); power law fit equation for the sampled particles; additionally sampled 8 particles (red circle); predicted A/V values using weight superimposed on the power law equation (yellow cross).

Eight additional particles are selected from the batch of Florida limestone aggregate for validation of the power law (Figure 4.8a). Particles of different sizes from the initially sampled 60 particles are selected, where 7 particles are smaller (less than 10 mm) while the other particle is larger (size ~ 95 mm) than the 60 particles. Likewise, the SL scanner is used to capture the 3D geometry of the 8 particles (Figure 4.8b), from which the A/V and V values are obtained and plotted (red circles) in Figure 5.1. The data points are close to the power function, which indicates that the power law relation holds true for the different sizes. It is worthwhile to note that the A/V ratio is inversely proportional to the particle size as implied by the unit, a reciprocal length. Therefore, the A/V of the large particle is small, while those of the 7 small particles are large. The particle volume V can be also indirectly estimated from the measured particle weights with use of the specific gravity of solids. Then the corresponding A/V value can be found from the power function.

The  $A/V$  and  $V$  values estimated in this manner are plotted as  $\times$  symbols in Figure 5.1, which are close to the data obtained from the high-resolution SL scanning. Therefore, the true Sphericity evaluated either way are close to each other as summarized in Table 5.1, which indicates the true Sphericity can be robustly predicted with the volume only once the power law relation between  $A/V$  and  $V$  is identified.

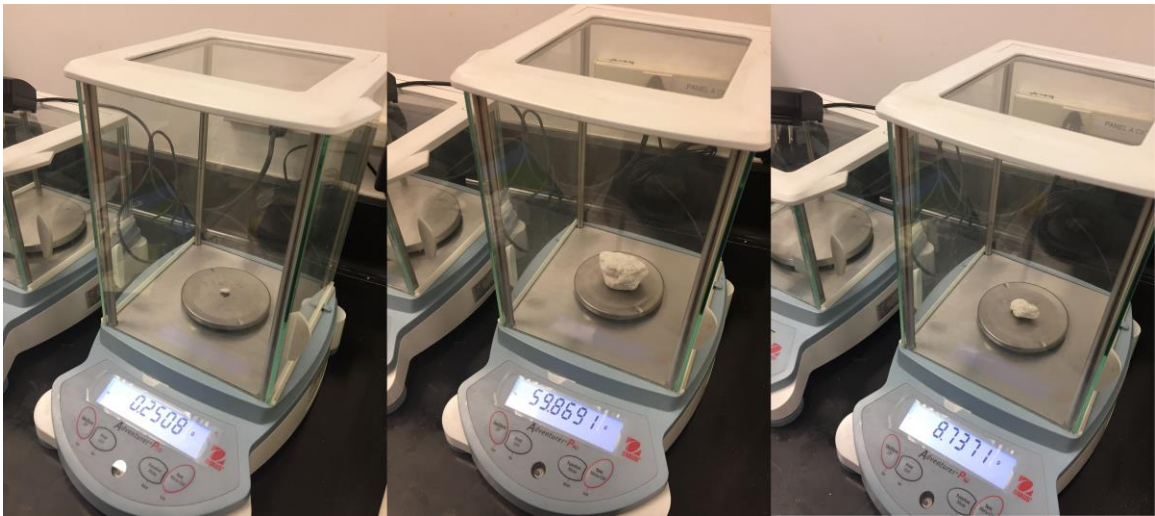


Figure 5.2. Measurement of particle weight.

Table 5.1. True sphericity of additionally sampled 8 particles obtained by (a) 3D structured light scanning and (b) using the V values indirectly estimated first with the measured particle weights, then the corresponding A/V ratios found from the power function.

Particle #	(a) 3D SL scanning	(b) V estimated with weight and A/V from the power function	% difference
a	0.865	0.863	0.231
b	0.922	0.866	6.074
c	0.888	0.868	2.252
d	0.860	0.859	0.116
e	0.892	0.864	3.139
f	0.853	0.864	1.290
g	0.888	0.863	2.815
h	0.795	0.763	4.025

#### 5.3.4 Rapid Characterization of the Shape Distribution in terms of the 3D Sphericity

The 3D Sphericity of a large number of particles are then estimated using the volume. A total of 344 particles are randomly selected from the same batch of ASTM #57 and #4 aggregates (Figure 5.3). The whole process to compute the Sphericity of 344 particles takes around 2 hours (i.e., about 20 seconds per particle), which is reasonably fast as the volume can be quickly obtained by measuring the weight, and the rest of the procedure is straightforward. Figure 5.4 shows the 3D Sphericity distribution of all 344 particles evaluated by both particle number and volume, which represents the overall shape distribution of the limestone aggregate.

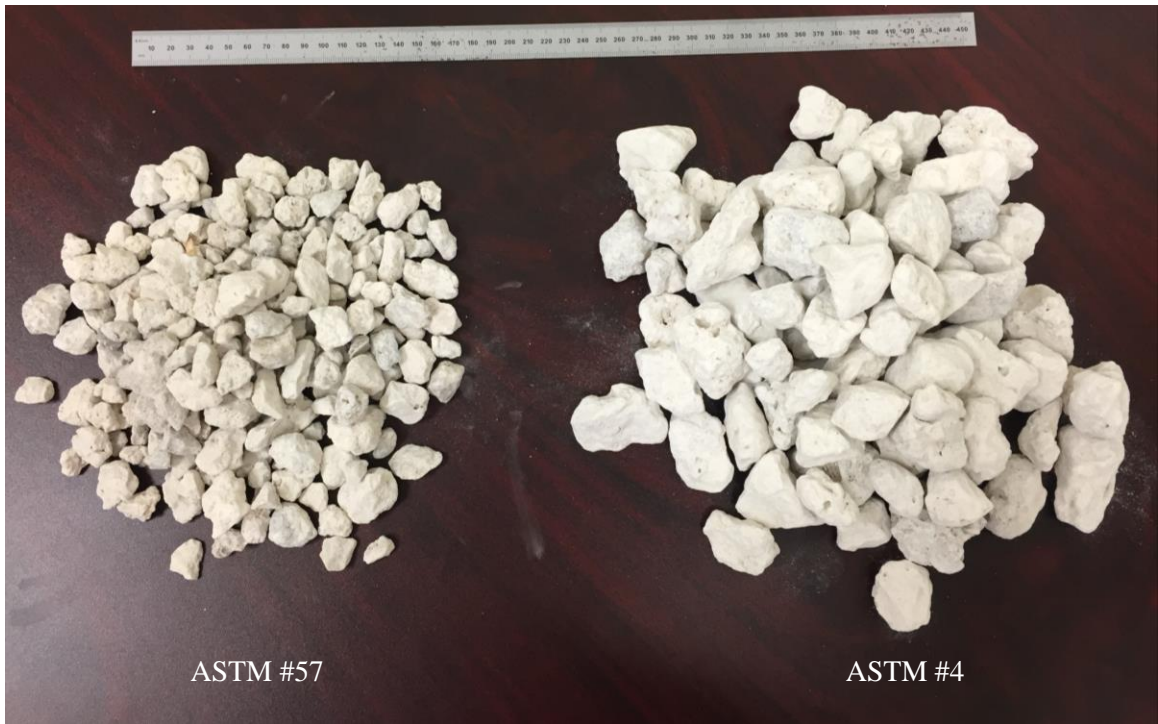


Figure 5.3. A total of 344 particles used to predict the 3D Sphericity distribution of the Florida limestone aggregate.

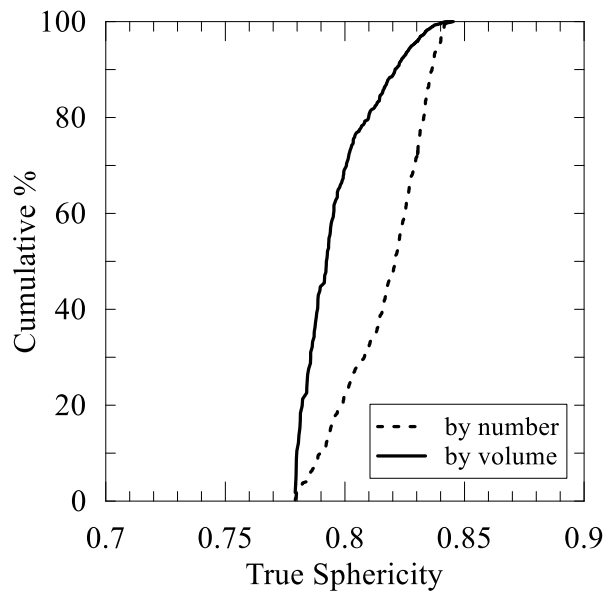


Figure 5.4. The 3D Sphericity distribution of the aggregate particles evaluated by both particle number and volume.

#### 5.4 Concluding Remarks

This study introduces a new framework that requires a minimal effort of 3D scanning to robustly estimate Wadell's true Sphericity that quantifies the 3D particle morphology. The true Sphericity requires three parameters to be measured, i.e., the surface area of sphere ( $A_s$ ), particle volume ( $V$ ), and particle surface-area-to-volume ratio ( $A/V$ ). For a given  $V$ , the computation of  $A_s$  in terms of  $V$  is straightforward, and the corresponding  $A/V$  is found from the power law relation between  $A/V$  and  $V$ , which is the key ingredient of the proposed 3D prediction framework. The power function can be identified with a minimal effort of 3D scanning, and  $V$  can be indirectly estimated by measuring the particle weight with the use of the specific gravity of solids. Therefore, the 3D Sphericity can be robustly predicted with the volume once the power function between  $A/V$  and  $V$  is identified.

In order to predict the  $M$  value, the measurement of size is necessary. Although measurement of size requires additional effort, but it also gives the complete two inter-related 2D spaces i.e.  $M$  vs  $L$  and  $A/V$  vs  $V$ . The advantage of sphericity prediction is that it is a quicker method since only one parameter (weight) is needed to be measured. However, since the size is not measured, sphericity distribution with respect to size is not known in this method. This study demonstrates that geometry analysis of a large number of particles can be rapidly and systematically performed, as the whole process only requires the particle weight to be measured for the estimation of volume. Therefore, this framework will facilitate the field inspection of aggregate as only a balance is needed to quantify the particle geometry.



## 6 CONCLUDING REMARKS AND RECOMMENDATION FOR FUTURE WORK

### 6.1 Concluding Remarks

This dissertation contributed in the field of multiscale mechanics of granular materials by systematically unraveling the inter-relation of geometry components that control the morphology at the grain-scale and demonstrating the correlation of morphology to macroscale properties of concrete and soil. It also provides quick and practical method to measure 3D geometry components for a large number of particles.

This dissertation systematically investigates how particle angularity influences the performance of CBM. Experiments have been conducted in controlled environment by properly controlling the mix proportion and quantifying aggregate morphology. These experiments validate three morphology-driven mechanisms of CBM. The experiments reveal that CBM with round aggregates have superior small-strain performance where CBM containing angular/crushed aggregates have superior large-strain performance. The outcome of this research shows that it is not always beneficial to use angular aggregates as they reduce the small-strain modulus by early micro-crack development, hence also affecting the durability.

This dissertation developing a systematic morphology characterization technique M-A-V-L. M-A-V-L characterization considers different 3D geometry components such as A, V and L and their interrelation. The characterization provides a two interrelated 2D space (M vs L and A/V vs V) where the interrelation of these components is graphically preserved. The two interrelated 2D spaces contain information about all the four morphology

components and how to obtain one component value from the other. Conventional method to describe particle morphology is to divide it into global form, local angularity and surface texture at three different length scales. How global form and local angularity were related and what fraction of contribution they each have in particle morphology was unclear. In reality, particle surface area, volume and size are intertwined and has to be considered together. M-A-V-L concept narrows down the number of grain-scale parameters to 4 (M, A, V, L). These 4 parameters are also interrelated. These 4 parameters can be leveraged to establish a link across scales.

This study shows experimental correlation of M with macroscopic direct shear strength. Four particles with known M values have been selected to conduct the experimental investigation. Experiments show accurate correlation of M with direct shear strength and corresponding vertical displacement. One of the most important finding of this study is the power law relationship between A/V vs V. This relationship is the key in predicting surface-area-to-volume-ratio from particle volume. Particle 3D volume is relatively easy to measure while there is no standard and easy method to obtain particle 3D surface area. The other major contribution of this dissertation is the quick and accurate measurement technique of particle 3D geometry. By leveraging the power law relationship between A/V and V, true sphericity distribution of a set of particles can be obtained very quickly by measuring just the weight of particle. This significantly improves the labor, computational and instrumentational cost of measuring accurate 3D geometry of a large number of particles which was not possible before. Particle morphology value can also be quickly estimated using just the particle weight and size.

## 6.2 Recommendation for Future Work

The present work can be expanded to investigate how 3D ‘true’ Sphericity and Morphology ‘distribution’ influence aggregate macroscale behavior. Triaxial compression tests can be performed on aggregate groups whose 3D Sphericity and Morphology distributions (e.g. well graded, uniformly graded with particles of varied morphology) are known beforehand. The validated test results can be further used to better understand and predict the behavior of aggregate groups with different morphology distribution. For example, it would be interesting to know how the mixed and near-spherical morphology groups behave differently in macroscale. This study can also be expanded to investigate how morphology influences other macroscale properties of soil and concrete such as durability, permeability, angle of repose, flowability etc.

Chapter 3 introduces two characteristics parameters of a morphology distribution  $\alpha$  (parameter describing morphologic heterogeneity) and  $\beta$  (parameter describing the representative morphology of the group). Chapter 4 experimentally obtains values of  $\alpha$  and  $\beta$  for Florida limestone. As part of a future research, these values should be measured for construction aggregates from different geographical regions with their inherent mineralogical and morphological features to obtain information about their morphology distribution. These  $\alpha$  and  $\beta$  value information could be used to prepare a particle morphology library which would facilitate research in particle morphology across the research community. Another area of investigation would be to assess the capability and accuracy of different 3D scanning techniques such as XRCT, laser scanning, SL scanning, photogrammetry etc. for different construction aggregates with mineralogical and morphological differences. This morphology index has also to be included in constitutive

modeling of soil and concrete to reflect the influence of particle morphology in stress-strain relationships.

## REFERENCES

- [1] Richard P, Nicodemi M, Delannay R, Ribiere P, Bideau D. Slow relaxation and compaction of granular systems. *Nat Mater* 2005;4:121–8. doi:10.1038\_nmat1300.
- [2] Kou B, Cao Y, Li J, Xia C, Li Z, Dong H, et al. Granular materials flow like complex fluids. *Nature* 2017;551:360–3. doi:10.1038/nature24062.
- [3] Cundall PA, Strack ODL. A Discrete Numerical Mode For Granular Assemblies. *Géotechnique* 1979;29:47–65.
- [4] Andrade JE, Baker JW, Ellison KC. Random porosity fields and their influence on the stability of granular media. *Int J Numer Anal Methods Geomech* 2008;32:189–213. doi:10.1002/nag.
- [5] Abbireddy COR, Clayton CRI. The impact of particle form on the packing and shear behaviour of some granular materials: an experimental study. *Granul Matter* 2015;17:427–38. doi:10.1007/s10035-015-0566-0.
- [6] Cho G-C, Dodds J, Santamarina JC. Particle Shape Effects on Packing Density, Stiffness, and Strength: Natural and Crushed Sands. *J Geotech Geoenvironmental Eng* 2006;132:591–602. doi:10.1061/(ASCE)1090-0241(2006)132:5(591).
- [7] Holubec I, D'Appolonia E. Effect of Particle Shape on the Engineering Properties of Granular Soils. *ASTM Spec Tech Publ* 1973.
- [8] Alshibli KA, Jarrar MF, Druckrey AM, Al-Raoush RI. Influence of Particle Morphology on 3D Kinematic Behavior and Strain Localization of Sheared Sand. *J Geotech Geoenvironmental Eng* 2016:04016097. doi:10.1061/(ASCE)GT.1943-5606.0001601.

- [9] Jerves AX, Kawamoto RY, Andrade JE. Effects of grain morphology on critical state: a computational analysis. *Acta Geotech* 2016;11:493–503. doi:10.1007/s11440-015-0422-8.
- [10] Rothenburg L, Bathurst RJ. Influence of particle eccentricity on micromechanical behavior of granular materials. *Mech Mater* 1993;16:141–52. doi:10.1016/0167-6636(93)90037-R.
- [11] Feng B, Hou W, Tutumluer E. Implications of Field Loading Patterns on Different Tie Support Conditions using Discrete Element Modeling: Dynamic Responses. *Transp Res Rec* 2019;2673:509–20. doi:10.1177/0361198118821936.
- [12] Indraratna B, Ngo NT, Rujikiatkamjorn C, Vinod JS. Behavior of Fresh and Fouled Railway Ballast Subjected to Direct Shear Testing: Discrete Element Simulation. *Int J Geomech* 2014;14:34–44. doi:10.1061/(ASCE)GM.1943-5622.0000264.
- [13] Moaveni M, Qian Y, Qamhia IIA, Tutumluer E, Basye C, Li D. Morphological Characterization of Railroad Ballast Degradation Trends in the Field and Laboratory. *Transp Res Rec J Transp Res Board* 2016;2545:89–99. doi:10.3141/2545-10.
- [14] Mehta PK, Monteiro PJM. *Concrete: Microstructure, Properties, and Materials*. 4th ed. McGraw-Hill; 2013.
- [15] Kuo C-Y, Freeman R. Image Analysis Evaluation of Aggregates for Asphalt Concrete Mixtures. *Transp Res Rec J Transp Res Board* 1998;1615:65–71. doi:10.3141/1615-09.
- [16] Kosmatka SH, Kerkhoff B, Panarese WC. *Design and Control of Concrete Mixtures*. 16th ed. Skokie, Illinois: Portland Cement Association; 2016.

- [17] PCI. PCI DESIGN HANDBOOK. 7th ed. 2010.
- [18] Indiana DOT. Standard Specifications 2018:1118.
- [19] Florida DOT. Standard Specifications for Road and Bridge Construction 2016.
- [20] Saouma VE, Broz JJ, Brühwiler E, Boggs HL. Effect of Aggregate and Specimen Size on Fracture Properties of Dam Concrete. *J Mater Civ Eng* 1991;3:204–18. doi:10.1061/(ASCE)0899-1561(1991)3:3(204).
- [21] Guinea G V., El-Sayed K, Rocco CG, Elices M, Planas J. The effect of the bond between the matrix and the aggregates on the cracking mechanism and fracture parameters of concrete. *Cem Concr Res* 2002;32:1961–70. doi:10.1016/S0008-8846(02)00902-X.
- [22] Li Q, Deng Z, Fu H. Effect of Aggregate Type on Mechanical Behavior of Dam Concrete. *ACI Mater J* · 2004;101:483–92.
- [23] Donza HA, Cabrera OA. The influence of kinds of fine aggregate on mechanical properties of high strength concrete. 4th Int. Symp. high-strength/high-performance Concr., Paris, France: 1996.
- [24] Giaccio G, Zerbino R. Failure Mechanism of Concrete: Combined Effects of Coarse Aggregates and Strength Level. *Adv Cem Based Mater* 1998;7:41–8. doi:10.1016/S1065-7355(97)00014-X.
- [25] Donza H, Cabrera O, Irassar EF. High-strength concrete with different fine aggregate. *Cem Concr Res* 2002;32:1755–61. doi:10.1016/S0008-8846(02)00860-8.
- [26] Piotrowska E, Malecot Y, Ke Y. Experimental Investigation of the Effect of Coarse Aggregate Shape and Composition on Concrete Triaxial Behavior. *Mech Mater* 2014;79:45–57.

- [27] Alexander M, Mindess S. *Aggregates in Concrete*. CRC Press; 2005.
- [28] Appa Rao G, Prasad BKR. Influence of type of aggregate and surface roughness on the interface fracture properties. *Mater Struct* 2004;37:328–34. doi:10.1617/13658.
- [29] Pan T, Liu Y, Tutumluer E. Microstructural Mechanisms of Early Age Cracking Behavior of Concrete: Fracture Energy Approach. *J Eng Mech* 2011;137:439–46.
- [30] Pan T, Tutumluer E. Quantification of Coarse Aggregate Surface Texture Using Image Analysis. *J Test Eval* 2007;35:100181. doi:10.1520/JTE100181.
- [31] Zampini D, Shah SP, Jennings HM. Early age microstructure of the paste-aggregate interface and its evolution. *J Mater Res* 1998;13:1888–98. doi:10.1557/JMR.1998.0268.
- [32] Yeggoni M. Influence of coarse aggregate size, shape and surface texture on rutting of hot mix asphalt concrete 1993.
- [33] Krumbein WC. Measurement and Geological Significance of Shape and Roundness of Sedimentary Particles. *J Sediment Petrol* 1941;11:64–72.
- [34] Wadell H. Sphericity and Roundness of Rock Particles. *J Geol* 1933;41:310–31.
- [35] Wadell H. Volume , Shape , and Roundness of Rock Particles. *J Geol* 1932;40:443–51.
- [36] Lees G. A New Method for Determining the Angularity of Particles. *Sedimentology* 1964;3:2–21. doi:10.1111/j.1365-3091.1964.tb00271.x.
- [37] Boggs S. Measurement of Roundness and Sphericity Parameters using an Electronic Particle Size Analyzer. *J Sediment Petrol* 1967;37:908–13.



- [38] Mora CF, Kwan AKH, Chan HC. Particle size distribution analysis of coarse aggregate using digital image processing. *Cem Concr Res* 1998;28:921–32. doi:[http://dx.doi.org/10.1016/S0008-8846\(98\)00043-X](http://dx.doi.org/10.1016/S0008-8846(98)00043-X).
- [39] Yudhbir, Abedinzadeh R. Quantification of particle shape and angularity using the image analyzer. *Geotech Test J* 1991;14:296–308. doi:10.1520/GTJ10574J.
- [40] Wadell H. Volume, Shape, and Roundness of Quartz Particles. *J Geol* 1935;43:250–80.
- [41] Zheng J, Hryciw RD. Traditional soil particle sphericity, roundness and surface roughness by computational geometry. *Géotechnique* 2015;65:494–506. doi:10.1680/geot.14.P.192.
- [42] Cruz-matías I, Ayala D, Hiller D, Gutsch S, Zacharias M, Estradé S, et al. Sphericity and roundness computation for particles using the extreme vertices model. *J Comput Sci* 2019;30:28–40. doi:10.1016/j.jocs.2018.11.005.
- [43] Terzaghi K, Peck RB, Mesri G. *Soil mechanics in engineering practice*. Wiley; 1996.
- [44] Lee KL, Seed HB. Drained Strength Characteristics of Sands. *J Soil Mech Found Div* 1967;93:117–41.
- [45] Rowe PW. The Stress-Dilatancy Relation for Static Equilibrium of an Assembly of Particles in Contact. *Proc R Soc A Math Phys Eng Sci* 1962;269:500–27. doi:10.1098/rspa.1962.0193.
- [46] Huang X, O’sullivan C, Hanley KJJ, Kwok CY. Discrete-element method analysis of the state parameter. *Géotechnique* 2014;64:954–65. doi:10.1680/geot.14.P.013.

- [47] Lee SJ, Hashash YMA, Nezami EG. Simulation of triaxial compression tests with polyhedral discrete elements. *Comput Geotech* 2012;43:92–100. doi:10.1016/j.compgeo.2012.02.011.
- [48] Hryciw RD, Zheng J, Ohm H-S, Li J. Innovations in Optical Geocharacterization. *Geo-Congress 2014 Keynote Lect. Geo-Characterization Model. Sustain.*, 2014, p. 97–116. doi:10.1061/9780784413289.005.
- [49] Al-rousan T, Masad E, Tutumluer E. Evaluation of image analysis techniques for quantifying aggregate shape characteristics 2007;21:978–90. doi:10.1016/j.conbuildmat.2006.03.005.
- [50] Rao C, Tutumluer E, Kim IT. Quantification of Coarse Aggregate Angularity Based on Image Analysis. *Transp Res Rec* 2002;1787:117–24. doi:10.3141/1787-13.
- [51] Sukumaran B, Ashmawy AK. Quantitative characterisation of the geometry of discret particles. *Géotechnique* 2001;51:619–27. doi:10.1680/geot.2001.51.7.619.
- [52] Yang J, Luo XD. Exploring the relationship between critical state and particle shape for granular materials. *J Mech Phys Solids* 2015;84:196–213. doi:10.1016/j.jmps.2015.08.001.
- [53] Altuhafi F, O’Sullivan C, Cavarretta I. Analysis of an Image-Based Method to Quantify the Size and Shape of Sand Particles. *J Geotech Geoenvironmental Eng* 2013;139:1290–307. doi:10.1061/(ASCE)GT.1943-5606.0000855.
- [54] Sympatec GmbH. QICPIC 2017.

- [55] Garboczi EJ. Three-dimensional mathematical analysis of particle shape using X-ray tomography and spherical harmonics: Application to aggregates used in concrete. *Cem Concr Res* 2002;32:1621–38. doi:10.1016/S0008-8846(02)00836-0.
- [56] Zhou B, Wang J, Zhao B. Micromorphology characterization and reconstruction of sand particles using micro X-ray tomography and spherical harmonics. *Eng Geol* 2015;184:126–37. doi:10.1016/j.enggeo.2014.11.009.
- [57] Zhang B, Lee SJ, Qian Y, Tutumluer E, Bhattacharya S. A Smartphone-Based Image Analysis Technique for Ballast Aggregates. *Int. Conf. Transp. Dev. 2016 Proj. Pract. Prosper. - Proc. 2016 Int. Conf. Transp. Dev., 2016*. doi:10.1061/9780784479926.057.
- [58] Mitchell JK, Soga K. *Fundamentals of soil behavior*. John Wiley & Sons; 2005.
- [59] ASTM C170. C170/C170M-09: Standard test method for compressive strength of dimension stone<sup>1</sup>. *Annu B ASTM Stand* 2011;1:9–11. doi:10.1520/C0170.
- [60] ASTM C150. ASTM C150/C150M - 18 Standard Specifications for Portland Cement 1999:1–9. doi:10.1520/C0150.
- [61] Kozul R, Darwin D. *EFFECTS OF AGGREGATE TYPE, SIZE, AND CONTENT ON CONCRETE STRENGTH AND FRACTURE ENERGY*. LAWRENCE, KANSAS: 1997.
- [62] ACI Committee 318. *Building Code Requirements for Structural Concrete (ACI 318-14)*. American Concrete Institute; 2014.
- [63] Rocco CG, Elices M. Effect of aggregate shape on the mechanical properties of a simple concrete. *Eng Fract Mech* 2009;76:286–98. doi:10.1016/j.engfracmech.2008.10.010.

- [64] He H, Courard L, Pirard E, Michel F. SHAPE ANALYSIS OF FINE AGGREGATES USED FOR CONCRETE. *Image Anal Stereol* 2016;35:159. doi:10.5566/ias.1400.
- [65] Garboczi EJ, Bullard JW. Shape analysis of a reference cement. *Cem Concr Res* 2004;34:1933–7. doi:10.1016/J.CEMCONRES.2004.01.006.
- [66] Holzer L, Flatt RJ, Erdoğan ST, Bullard JW, Garboczi EJ. Shape Comparison between 0.4-2.0 and 20-60  $\mu\text{m}$  Cement Particles. *J Am Ceram Soc* 2010;93:1626–33. doi:10.1111/j.1551-2916.2010.03654.x.
- [67] Neville AM. *Properties of Concrete*. 4th ed. 1996.
- [68] Mindess S, Young JF, Darwin D. *Concrete*. Prentice Hall; 2003.
- [69] Wong HS, Zobel M, Buenfeld NR, Zimmerman RW. Influence of the interfacial transition zone and microcracking on the diffusivity, permeability and sorptivity of cement-based materials after drying. *Mag Concr Res* 2009;61:571–89. doi:10.1680/mac.2008.61.8.571.
- [70] Autodesk. ReCap 2017.
- [71] Zhang B, Lee SJ, Qian Y, Tutumluer E, Bhattacharya S. A Smartphone-Based Image Analysis Technique for Ballast Aggregates. *Int. Conf. Transp. Dev.* 2016, Reston, VA: American Society of Civil Engineers; 2016, p. 623–30. doi:10.1061/9780784479926.057.
- [72] ASTM C33/C33M-16e1. *Standard Specification for Concrete Aggregates*. West Conshohocken, PA: ASTM International; 2016.
- [73] Wadell H. Sphericity and Roundness of Rock Particles. *J Geol* 1933;41:310–31.

- [74] Sukumaran B, Ashmawy AK. Quantitative characterisation of the geometry of discrete particles. *Géotechnique* 2001;51:619–27. doi:10.1680/geot.2001.51.7.619.
- [75] Tutumluer E, Rao C, Stefanski JA. Video Image Analysis of Aggregates 2000:161.
- [76] Bagheri GH, Bonadonna C, Manzella I, Vonlanthen P. On the Characterization of Size and Shape of Irregular Particles. *Powder Technol* 2015;270:141–53.
- [77] Moaveni M, Wang S, Hart JM, Tutumluer E, Ahuja N. Evaluation of Aggregate Size and Shape by Means of Segmentation Techniques and Aggregate Image Processing Algorithms. *J Transp Res Board* 2013;2335:50–9.
- [78] Fernlund JMR. Image analysis method for determining 3-D shape of coarse aggregate. *Cem Concr Res* 2005;35:1629–37. doi:10.1016/j.cemconres.2004.11.017.
- [79] Rother C, Kolmogorov V, Blake A. “GrabCut”: interactive foreground extraction using iterated graph cuts. *ACM SIGGRAPH 2004 Pap. - SIGGRAPH '04*, New York, New York, USA: ACM Press; 2004, p. 309. doi:10.1145/1186562.1015720.
- [80] OpenCV. Open Source Computer Vision Library 2017.
- [81] Selinger P. Potrace 2017.
- [82] Wenzel RN. Surface Roughness and Contact Angle. *J Phys Colloid Chem* 1949;53:1466–7. doi:10.1021/j150474a015.
- [83] ASTM. ASTM D7334 - Standard Practice for Surface Wettability of Coatings, Substrates and Pigments by Advancing Contact Angle Measurement. *ASTM Int* 2013;06.01. doi:10.1520/D7334-08R13.
- [84] ACI Committee E701. E4-12 Chemical Admixtures for Concrete. 2013.

- [85] ASTM. ASTM C127 - Standard Test Method for Relative Density (Specific Gravity) and Absorption of Coarse Aggregate. 2ASTM Int 2015;04.02. doi:10.1520/C0127-15.
- [86] ASTM. ASTM C496 / C496M - 11 Standard Test Method for Splitting Tensile Strength of Cylindrical Concrete Specimens. ASTM Int 2011;04.02:5.
- [87] ASTM. ASTM C39/C39M-17a Standard Test Method for Compressive Strength of Cylindrical Concrete Specimens. ASTM Int 2017;04.02:8.
- [88] ASTM C469-14. Standard Test Method for Static Modulus of Elasticity and Poisson's Ratio of Concrete in Compression. West Conshohocken, PA: ASTM International; 2014.
- [89] Slate FO, Hover KC. Microcracking in Concrete. In: Carpinteri A, Ingraffea AR, editors. Fract. Mech. Concr. Mater. Charact. Test., Martinus Nijhoff Publishers; 1984, p. 137–59.
- [90] Kosmatka SH, L. Wilson M. Design and Control of Concrete Mixtures. Portland Cement Association; 2011.
- [91] Quiroga PN, Fowler DW. THE EFFECTS OF AGGREGATES CHARACTERISTICS ON THE PERFORMANCE OF PORTLAND CEMENT CONCRETE. 2003.
- [92] Carpinteri A, A. R. Ingraffea. Fracture mechanics of concrete: Material characterization and testing. Martinus Nijhoff Publishers; 1984.

- [93] Garboczi EJ, Bullard JW. 3D analytical mathematical models of random star-shape particles via a combination of X-ray computed microtomography and spherical harmonic analysis. *Adv Powder Technol* 2017;28:325–39. doi:10.1016/j.apr.2016.10.014.
- [94] Barrett PJ. The shape of rock particles, a critical review. *Sedimentology* 1980;27:291–303. doi:10.1111/j.1365-3091.1980.tb01179.x.
- [95] Zhao B, Wang J. 3D quantitative shape analysis on form, roundness, and compactness with  $\mu$ CT. *Powder Technol* 2016;291:262–75. doi:10.1016/j.powtec.2015.12.029.
- [96] Lin CL, Miller JD. 3D characterization and analysis of particle shape using X-ray microtomography ( XMT ) 2005;154:61–9. doi:10.1016/j.powtec.2005.04.031.
- [97] Lim K-W, Kawamoto R, Andò E, Viggiani G, Andrade JE. Multiscale characterization and modeling of granular materials through a computational mechanics avatar: a case study with experiment. *Acta Geotech* 2016;11:243–53. doi:10.1007/s11440-015-0405-9.
- [98] Latham JP, Munjiza A, Garcia X, Xiang J, Guises R. Three-dimensional particle shape acquisition and use of shape library for DEM and FEM/DEM simulation. *Miner Eng* 2008;21:797–805. doi:10.1016/j.mineng.2008.05.015.
- [99] Asahina D, Taylor MA. Geometry of irregular particles: Direct surface measurements by 3-D laser scanner. *Powder Technol* 2011;213:70–8. doi:10.1016/j.powtec.2011.07.008.

- [100] Paixão A, Resende R, Fortunato E. Photogrammetry for digital reconstruction of railway ballast particles – A cost-efficient method. *Constr Build Mater* 2018;191:963–76. doi:10.1016/j.conbuildmat.2018.10.048.
- [101] Alshibli KA, Druckrey AM, Al-Raoush RI, Weiskittel T, Lavrik N V. Quantifying Morphology of Sands Using 3D Imaging. *J Mater Civ Eng* 2015;27:04014275. doi:10.1061/(ASCE)MT.1943-5533.0001246.
- [102] Kong D, Fonseca J. Quantification of the morphology of shelly carbonate sands using 3D images. *Geotechnique* 2017;1–13. doi:10.1680/jgeot.16.P.278.
- [103] Bullard JW, Garboczi EJ. Defining shape measures for 3D star-shaped particles: Sphericity, roundness, and dimensions. *Powder Technol* 2013;249:241–52. doi:10.1016/j.powtec.2013.08.015.
- [104] Santamarina J, Cho G. Soil behaviour: The role of particle shape. *Adv Geotech Eng Proc Skempton Conf* 2004;1–14. doi:[http://pmrl.ce.gatech.edu/tools/santamarina\\_cho\\_2004.pdf](http://pmrl.ce.gatech.edu/tools/santamarina_cho_2004.pdf).
- [105] Santamarina JC, Cho GC. Soil behaviour : The role of particle shape. *Adv. Geotech. Eng. Skempton Conf., The Institution of Civil Engineers*; 2004.
- [106] Lee SJ, Lee CH, Shin M, Bhattacharya S, Su YF. Influence of coarse aggregate angularity on the mechanical performance of cement-based materials. *Constr Build Mater* 2019;204:184–92. doi:10.1016/j.conbuildmat.2019.01.135.
- [107] Zheng J, Hryciw RD. An image based clump library for DEM simulations. *Granul Matter* 2017;19:26. doi:10.1007/s10035-017-0713-x.



- [108] Sun Q, Zheng Y, Li B, Zheng J, Wang Z. Three-dimensional particle size and shape characterisation using structural light. *Géotechnique Lett* 2019;9:72–8. doi:10.1680/jgele.18.00207.
- [109] Masad E, Fletcher. T. Aggregate imaging system (AIMS): basics and application. Texas Transp Inst 2005;Report 5-1.
- [110] Le Pen LM, Powrie W, Zervos A, Ahmed S, Aingaran S. Dependence of shape on particle size for a crushed rock railway ballast. *Granul Matter* 2013;15:849–61. doi:10.1007/s10035-013-0437-5.
- [111] Krumbien WC, Sloss LL. *Stratigraphy and Sedimentation*. W H Free Co San Fr USA 1951.
- [112] Bagheri GH, Bonadonna C, Manzella I, Vonlanthen P. On the characterization of size and shape of irregular particles. *Powder Technol* 2015;270:141–53. doi:10.1016/j.powtec.2014.10.015.
- [113] Zheng J, Hryciw RD. Particle shape analysis code 2017.
- [114] Mollon G, Zhao J. Generating realistic 3D sand particles using Fourier descriptors. *Granul Matter* 2013;15:95–108. doi:10.1007/s10035-012-0380-x.
- [115] Formlabs. Form 1+ 2014.
- [116] Watters MP, Bernhardt ML. Curing parameters to improve the mechanical properties of stereolithographic printed specimens. *Rapid Prototyp J* 2018;24:46–51. doi:10.1108/RPJ-11-2016-0180.
- [117] Zguris Z. How Mechanical Properties of Stereolithography 3D Prints are Affected by UV Curing. Formlabs White Pap 2016.

- [118] Su Y-F, Zhang B, Lee SJ, Sukumaran B. Parametric Sensitivity Study of Particle Shape Effect Through 3D Printing. In: Li X, Feng Y, Mustoe G, editors. DEM 2016 Proc. 7th Int. Conf. Discret. Elem. Methods, Springer; 2017, p. 593–600. doi:10.1007/978-981-10-1926-5\_61.
- [119] ASTM. ASTM D3080/D3080M—11 Standard Test Method for Direct Shear Test of Soils Under Consolidated Drained Conditions. ASTM Int 2011;9. doi:10.1520/D3080\_D3080M-11.
- [120] Qian Y, Lee SJ, Tutumluer E, Hashash YMA, Ghaboussi J. Role of initial particle arrangement in ballast mechanical behavior. Int J Geomech 2018;18:1–10. doi:10.1061/(ASCE)GM.1943-5622.0001074.
- [121] Maeda K, Sakai H, Kondo A, Yamaguchi T, Fukuma M, Nukudani E. Stress-chain based micromechanics of sand with grain shape effect. Granul Matter 2010;12:499–505. doi:10.1007/s10035-010-0208-5.
- [122] Abbireddy COR, Clayton CRI. Varying initial void ratios for DEM simulations. Géotechnique 2010;60:497–502. doi:10.1680/geot.2010.60.6.497.
- [123] Karatza Z, Andò E, Papanicolopoulos S-A, Viggiani G, Ooi JY. Effect of particle morphology and contacts on particle breakage in a granular assembly studied using X-ray tomography. Granul Matter 2019;21. doi:10.1007/s10035-019-0898-2.
- [124] Mollon G, Zhao J. 3D generation of realistic granular samples based on random fields theory and Fourier shape descriptors. Comput Methods Appl Mech Eng 2014;279:46–65. doi:10.1016/j.cma.2014.06.022.

- [125] Huang H, Tutumluer E. Image-Aided Element Shape Generation Method in Discrete-Element Modeling for Railroad Ballast. *J Mater Civ Eng* 2014;26:527–35. doi:10.1061/(ASCE)MT.1943-5533.
- [126] Rao C, Tutumluer E, Stefanski JA. Coarse Aggregate Shape and Size Properties Using a New Image Analyzer. *J Test Eval JTEVA* 2001;29:461–71.
- [127] Komba JJ, Anochie-boateng JK. Analytical and Laser Scanning Techniques to Determine Shape Properties of Aggregates. *Transp Res Rec J Transp Res Board* 2013;2335:60–71. doi:10.3141/2335-07.
- [128] Lansdown H. *Digital Modelmaking: Laser Cutting, 3D Printing and Reverse Engineering*. Crowood Press; 2019.
- [129] ASTM Standard C33/C33M. *Standard Specification for Concrete Aggregates* 2018. doi:10.1520/C0033.
- [130] Wu C. Towards linear-time incremental structure from motion. *Proc - 2013 Int Conf 3D Vision, 3DV 2013* 2013:127–34. doi:10.1109/3DV.2013.25.
- [131] Furukawa Y, Curless B, Seitz SM, Szeliski R. Towards internet-scale multi-view stereo. *Proc IEEE Comput Soc Conf Comput Vis Pattern Recognit* 2010:1434–41. doi:10.1109/CVPR.2010.5539802.
- [132] Cignoni P, Callieri M, Corsini M, Dellepiane M, Ganovelli F, Ranzuglia G. *MeshLab: An open-source mesh processing tool*. 6th Eurographics Ital Chapter Conf 2008 - Proc 2008.
- [133] Kazhdan M, Bolitho M, Hoppe H. Poisson surface reconstruction. *Eurographics Symp Geom Process* 2006:61–70. doi:10.1145/1364901.1364904.

- [134] Blender. Blender - a 3D modelling and rendering package 2019.
- [135] Semechko A. Exact minimum bounding spheres/circles 2019.
- [136] Rodriguez J, Edeskär T, Knutsson S. Particle Shape Quantities and Measurement Techniques - A review. *Electron J Geotech Eng* 2013;18:169–98.
- [137] Zheng J, Hryciw RD. Roundness and Sphericity of Soil Particles in Assemblies by Computational Geometry. *J Comput Civ Eng* 2016;30:04016021. doi:10.1061/(ASCE)CP.1943-5487.0000578.
- [138] Hewlett-Packard. HP 3D Structured Light Scanner Pro S3 2016.

## APPENDICES

**Appendix A – Geometry Parameter Values for Each of 100 Particles in Mixed and  
Near-Spherical Morphology groups**

Table A.1. Particle Geometry Data for Mixed Group.

Particle Number		Volume (V) (mm <sup>3</sup> )	Surface Area (A) (mm <sup>2</sup> )	Size (L) (mm)	Morphology (M)
Row number	Column number				
1	1	215.333	181.430	8.109	1.139
	2	280.709	214.140	8.719	1.109
	3	229.203	185.476	8.042	1.085
	4	326.946	232.899	8.912	1.058
	5	239.696	191.451	8.296	1.104
	6	112.634	122.463	6.954	1.260
	7	212.349	179.450	8.167	1.150
	8	277.643	209.486	8.587	1.080
	9	367.542	250.045	9.135	1.036
	10	334.526	234.685	9.101	1.064
2	1	47.538	78.938	5.920	1.639
	2	29.752	54.514	5.566	1.700
	3	92.344	112.758	6.850	1.394
	4	45.501	67.742	5.822	1.445
	5	93.016	105.239	6.915	1.304
	6	169.370	154.096	8.168	1.239
	7	189.581	164.399	8.201	1.185
	8	214.690	176.627	8.264	1.133
	9	239.175	188.767	8.395	1.104
	10	250.261	194.500	8.623	1.117
3	1	51.605	73.095	6.178	1.458
	2	102.953	112.975	7.395	1.352
	3	45.042	68.136	6.049	1.525
	4	26.632	49.764	5.119	1.594
	5	145.441	137.900	7.563	1.195
	6	87.994	98.683	6.853	1.281
	7	133.011	128.502	7.496	1.207
	8	338.957	237.502	8.941	1.044
	9	163.018	148.063	7.851	1.188
	10	217.531	179.324	8.458	1.162

Table A.1. Particle Geometry Data for Mixed Group (Continued).

Particle Number		Volume (V) (mm <sup>3</sup> )	Surface Area (A) (mm <sup>2</sup> )	Size (L) (mm)	Morphology (M)
Row number	Column number				
4	1	26.885	49.693	5.343	1.646
	2	32.129	60.506	5.886	1.848
	3	28.258	49.239	5.566	1.617
	4	139.842	136.088	7.850	1.273
	5	76.954	95.094	6.918	1.425
	6	112.388	119.050	7.398	1.306
	7	108.777	116.311	7.171	1.278
	8	172.970	155.490	8.041	1.205
	9	225.597	182.337	8.493	1.144
	10	122.314	124.135	7.787	1.317
5	1	26.491	50.013	6.082	1.914
	2	12.912	30.993	4.602	1.841
	3	18.141	38.324	5.083	1.790
	4	54.990	74.190	6.404	1.440
	5	39.403	63.365	6.307	1.690
	6	44.077	66.467	5.695	1.431
	7	50.702	72.311	6.339	1.507
	8	66.423	83.552	6.336	1.328
	9	64.001	82.663	6.499	1.399
	10	50.934	69.989	6.146	1.408
6	1	7.230	22.125	4.536	2.313
	2	13.243	32.024	4.861	1.959
	3	30.188	52.094	6.082	1.749
	4	28.180	49.453	5.408	1.582
	5	40.472	61.487	5.762	1.459
	6	83.874	97.987	7.205	1.403
	7	56.635	76.086	6.498	1.455
	8	66.989	84.967	6.952	1.470
	9	72.588	88.778	6.919	1.410
	10	53.201	74.190	6.855	1.593



Table A.1. Particle Geometry Data for Mixed Group (Continued).

Particle Number		Volume (V) (mm <sup>3</sup> )	Surface Area (A) (mm <sup>2</sup> )	Size (L) (mm)	Morphology (M)
Row number	Column number				
7	1	15.063	33.363	5.407	1.996
	2	4.773	16.676	3.802	2.214
	3	35.201	57.898	6.408	1.757
	4	43.895	65.607	6.497	1.618
	5	34.501	55.010	5.729	1.522
	6	47.109	68.489	6.402	1.551
	7	39.047	59.740	5.826	1.486
	8	29.239	49.233	5.405	1.517
	9	54.446	74.589	6.697	1.529
	10	38.581	59.936	6.146	1.591
8	1	5.276	17.737	4.116	2.306
	2	2.597	11.555	3.574	2.651
	3	9.023	24.742	4.668	2.133
	4	16.001	35.081	5.246	1.917
	5	8.434	23.937	4.444	2.102
	6	6.469	19.989	4.055	2.088
	7	15.734	33.572	4.796	1.706
	8	21.237	40.904	5.117	1.643
	9	32.661	53.479	5.762	1.572
	10	12.959	30.727	5.182	2.048
9	1	1.947	10.031	3.255	2.794
	2	3.501	13.132	4.057	2.537
	3	2.389	11.202	3.349	2.618
	4	14.242	32.749	5.147	1.972
	5	3.797	15.359	3.963	2.672
	6	10.122	26.494	4.862	2.121
	7	15.421	34.598	5.379	2.011
	8	11.399	28.206	4.827	1.991
	9	8.308	22.889	4.377	2.010
	10	6.324	19.457	4.314	2.212

Table A.1. Particle Geometry Data for Mixed Group (Continued).

Particle Number		Volume (V) (mm <sup>3</sup> )	Surface Area (A) (mm <sup>2</sup> )	Size (L) (mm)	Morphology (M)
Row number	Column number				
10	1	4.814	16.292	4.090	2.307
	2	4.550	16.156	4.379	2.591
	3	1.609	8.334	3.125	2.698
	4	1.384	7.839	3.252	3.069
	5	3.825	14.705	4.028	2.581
	6	2.386	10.920	3.607	2.751
	7	6.128	20.030	4.695	2.558
	8	3.797	14.148	3.738	2.321
	9	6.596	19.988	4.248	2.145
	10	8.845	23.615	4.571	2.034

Table A.2. Particle Geometry Data for Near-Spherical Group.

Particle Number		Volume (V) (mm <sup>3</sup> )	Surface Area (A) (mm <sup>2</sup> )	Size (L) (mm)	Morphology (M)
Row number	Column number				
1	1	327.290	232.718	8.984	1.065
	2	320.079	228.506	8.876	1.056
	3	322.706	228.806	8.830	1.043
	4	275.090	207.197	8.780	1.102
	5	285.101	211.747	8.726	1.080
	6	283.212	210.673	8.612	1.068
	7	271.628	204.718	8.604	1.081
	8	271.849	204.696	8.565	1.075
	9	288.523	212.411	8.501	1.043
	10	260.339	199.146	8.435	1.075
2	1	279.769	208.054	8.370	1.037
	2	283.699	211.156	8.365	1.038
	3	221.988	178.867	8.262	1.110
	4	256.509	196.280	8.130	1.037
	5	243.775	189.881	8.020	1.041
	6	229.494	182.857	8.020	1.065
	7	188.155	161.096	8.010	1.143
	8	220.458	178.369	7.996	1.078
	9	237.395	186.920	7.979	1.047
	10	211.951	173.829	7.870	1.076
3	1	196.139	165.054	7.843	1.100
	2	191.186	161.606	7.635	1.076
	3	207.783	171.059	7.601	1.043
	4	201.886	167.276	7.539	1.041
	5	193.269	162.905	7.499	1.053
	6	164.157	147.046	7.436	1.110
	7	169.398	150.063	7.383	1.090
	8	190.218	160.938	7.384	1.041
	9	150.141	138.827	7.379	1.137
	10	167.654	148.309	7.291	1.075

Table A.2. Particle Geometry Data for Near-Spherical Group (Continued).

Particle Number		Volume (V) (mm <sup>3</sup> )	Surface Area (A) (mm <sup>2</sup> )	Size (L) (mm)	Morphology (M)
Row number	Column number				
4	1	164.120	146.524	7.280	1.083
	2	150.721	138.425	7.267	1.112
	3	171.323	149.775	7.224	1.053
	4	156.489	141.858	7.161	1.082
	5	147.044	135.700	7.033	1.082
	6	148.238	136.005	6.976	1.067
	7	142.207	133.139	6.967	1.087
	8	138.474	130.285	6.871	1.077
	9	125.946	122.711	6.772	1.100
	10	112.798	113.789	6.740	1.133
5	1	126.178	122.993	6.741	1.095
	2	131.495	126.011	6.718	1.073
	3	123.382	121.169	6.717	1.099
	4	102.934	107.128	6.544	1.135
	5	116.915	116.542	6.527	1.084
	6	101.145	105.924	6.345	1.107
	7	97.509	103.161	6.314	1.113
	8	111.839	113.060	6.296	1.061
	9	102.983	106.821	6.050	1.046
	10	96.024	102.063	6.026	1.067
6	1	90.624	98.316	6.007	1.086
	2	86.386	95.043	5.954	1.092
	3	93.912	100.374	5.935	1.057
	4	82.631	93.016	5.931	1.113
	5	87.290	96.052	5.915	1.085
	6	74.343	86.582	5.861	1.138
	7	73.993	86.166	5.708	1.108
	8	69.564	82.545	5.695	1.126
	9	66.328	80.169	5.592	1.127
	10	77.360	88.307	5.484	1.043

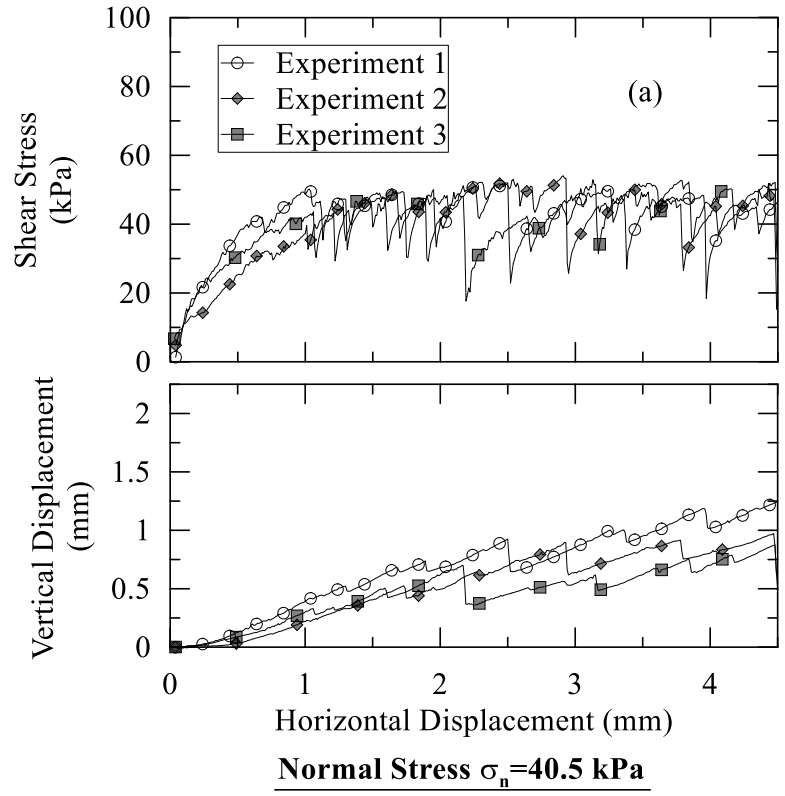
Table A.2. Particle Geometry Data for Near-Spherical Group (Continued).

Particle Number		Volume (V) (mm <sup>3</sup> )	Surface Area (A) (mm <sup>2</sup> )	Size (L) (mm)	Morphology (M)
Row number	Column number				
7	1	62.641	77.038	5.386	1.104
	2	63.249	77.885	5.343	1.097
	3	59.640	74.805	5.345	1.117
	4	56.097	71.986	5.265	1.126
	5	58.545	73.572	5.199	1.089
	6	52.423	68.262	5.170	1.122
	7	56.974	72.619	5.146	1.093
	8	60.920	75.246	5.113	1.053
	9	48.764	65.490	5.095	1.140
	10	48.031	64.445	5.058	1.131
8	1	48.640	64.995	5.034	1.121
	2	48.700	65.033	4.983	1.109
	3	50.783	66.997	4.967	1.092
	4	43.794	60.958	4.939	1.146
	5	44.003	60.977	4.878	1.127
	6	41.272	58.230	4.682	1.101
	7	38.539	55.780	4.687	1.131
	8	40.989	57.920	4.617	1.087
	9	31.321	48.455	4.445	1.146
	10	34.637	51.951	4.415	1.104
9	1	34.103	51.101	4.382	1.094
	2	35.363	52.397	4.343	1.072
	3	32.127	49.420	4.266	1.094
	4	28.530	45.526	4.153	1.105
	5	29.401	46.518	4.090	1.079
	6	27.282	44.314	4.074	1.103
	7	23.414	40.119	4.061	1.160
	8	25.368	42.016	3.832	1.058
	9	23.323	39.891	3.826	1.091
	10	21.462	37.783	3.824	1.122

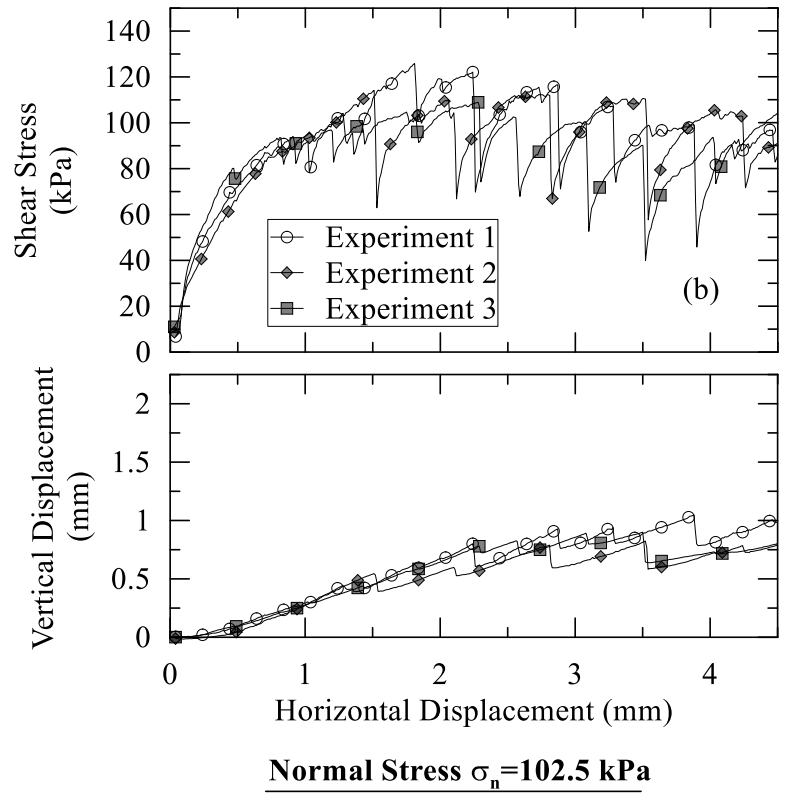
Table A.2. Particle Geometry Data for Near-Spherical Group (Continued).

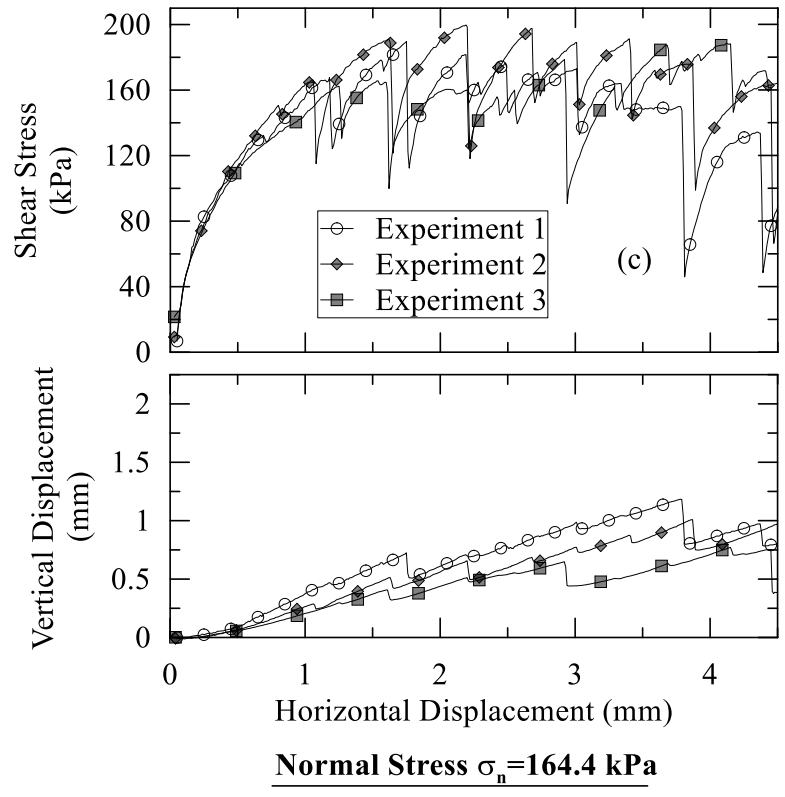
Particle Number		Volume (V) (mm <sup>3</sup> )	Surface Area (A) (mm <sup>2</sup> )	Size (L) (mm)	Morphology (M)
Row number	Column number				
10	1	19.034	34.795	3.749	1.142
	2	18.976	34.743	3.646	1.113
	3	19.418	35.187	3.610	1.090
	4	19.396	35.280	3.592	1.089
	5	20.709	36.784	3.597	1.065
	6	16.163	31.091	3.323	1.065
	7	14.222	28.597	3.285	1.101
	8	13.613	27.910	3.265	1.116
	9	12.838	26.798	3.252	1.131
	10	14.413	28.805	3.192	1.063

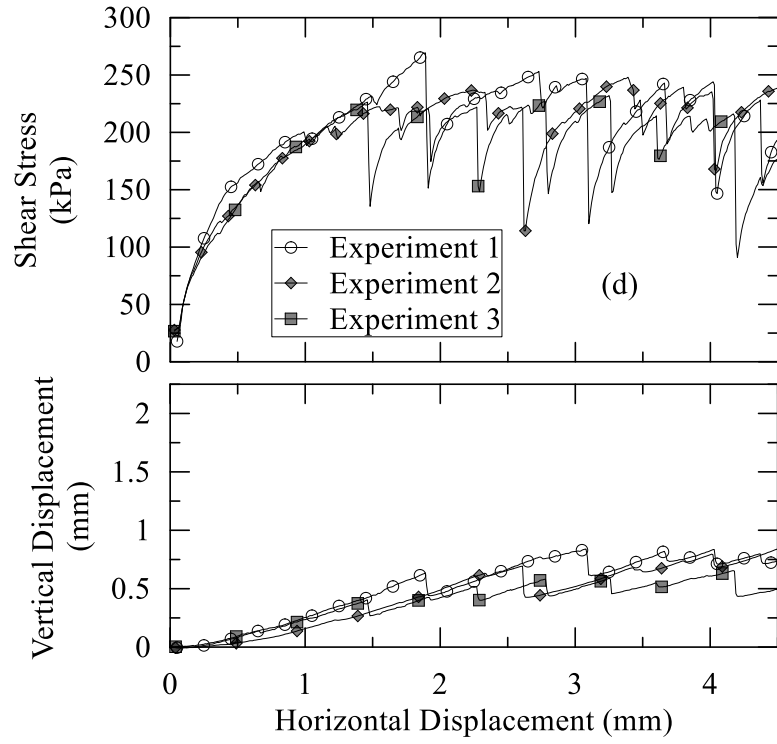
**Appendix B – Direct Shear Test Experimental Data on 3D-Printed Particles**





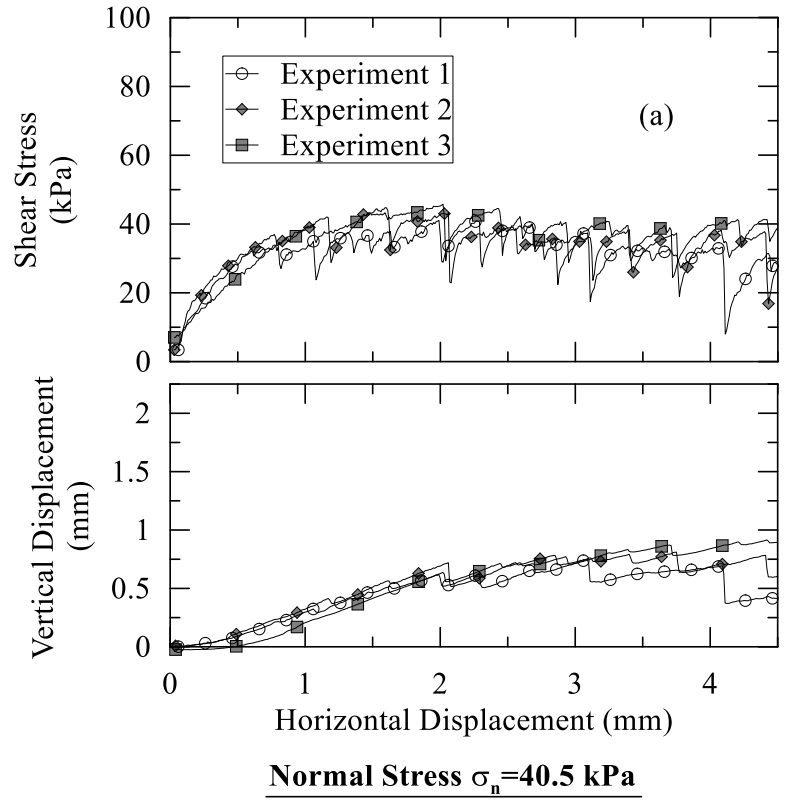


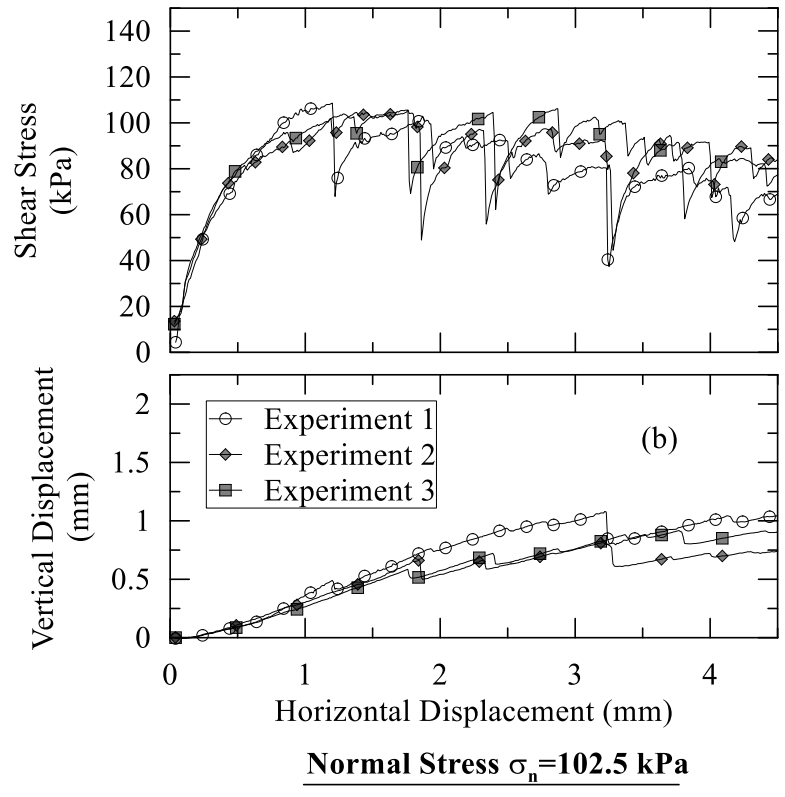


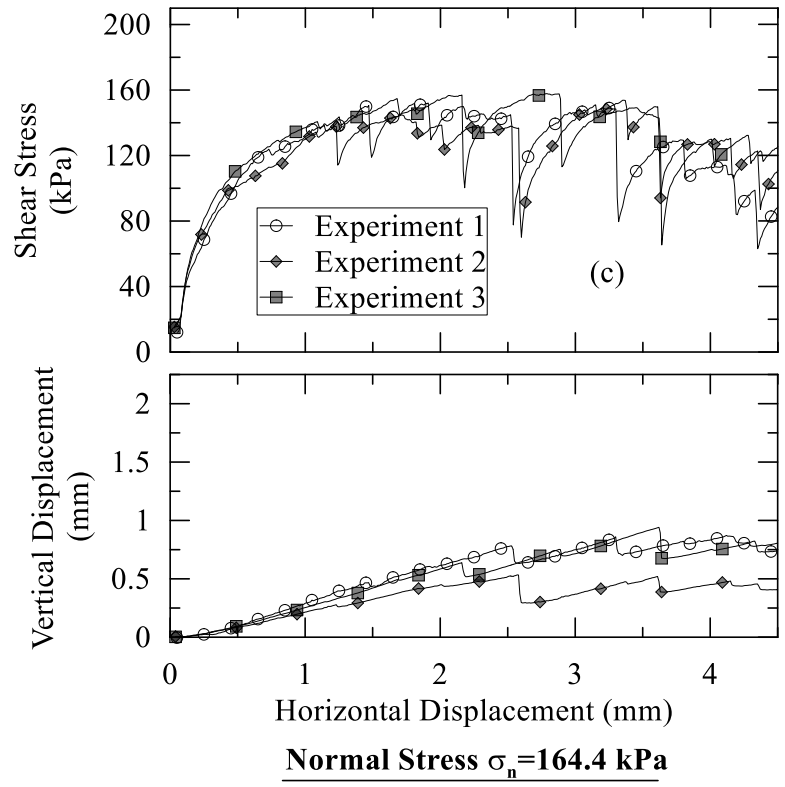


**Normal Stress  $\sigma_n=226.4$  kPa**

Figure B.1. Direct shear test results for particle 1-1.







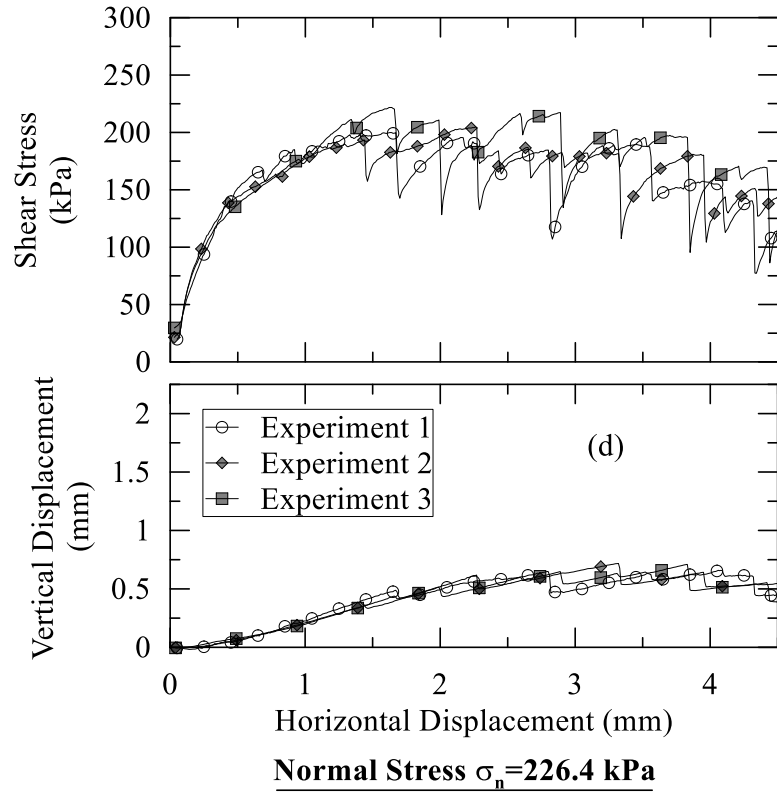
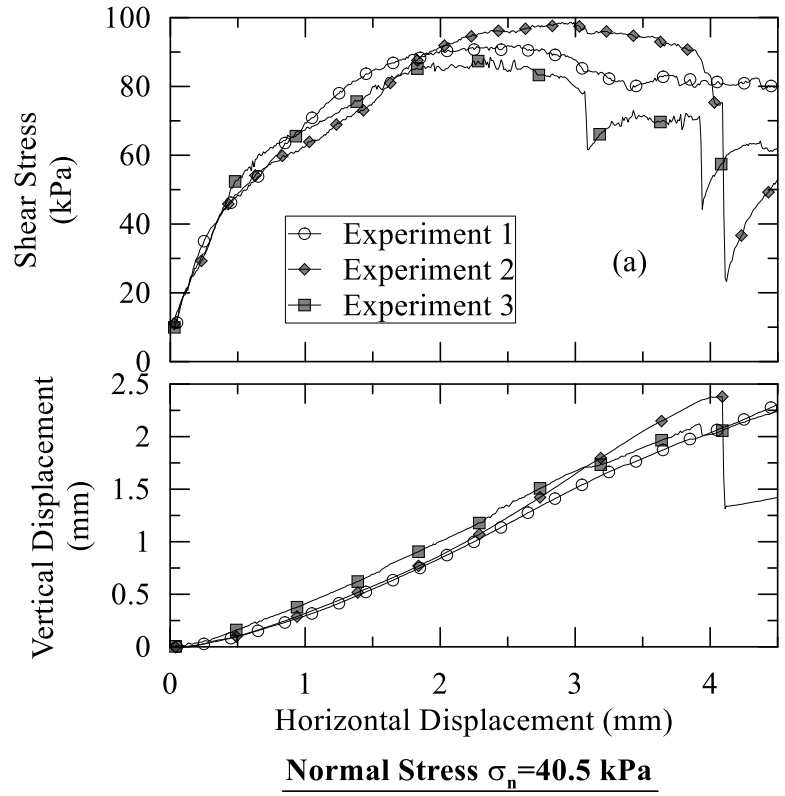
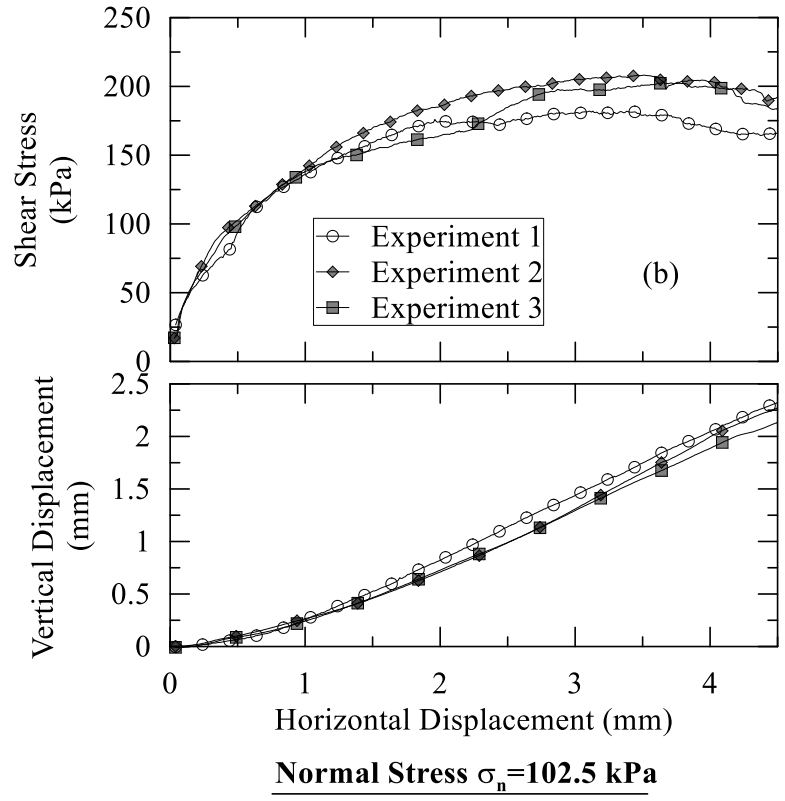
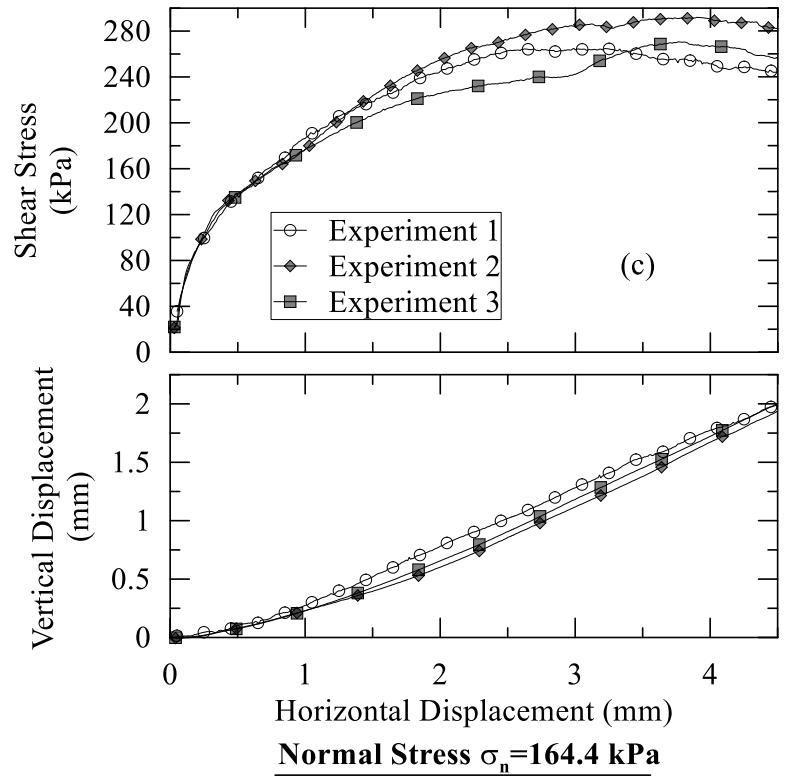


Figure B.2. Direct shear test results for particle 1-5.









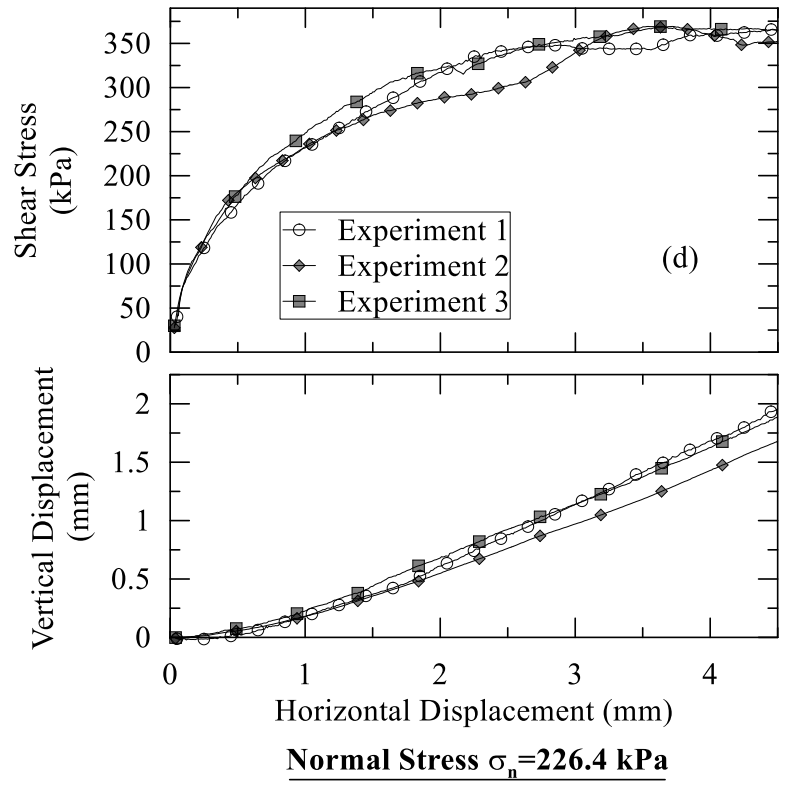
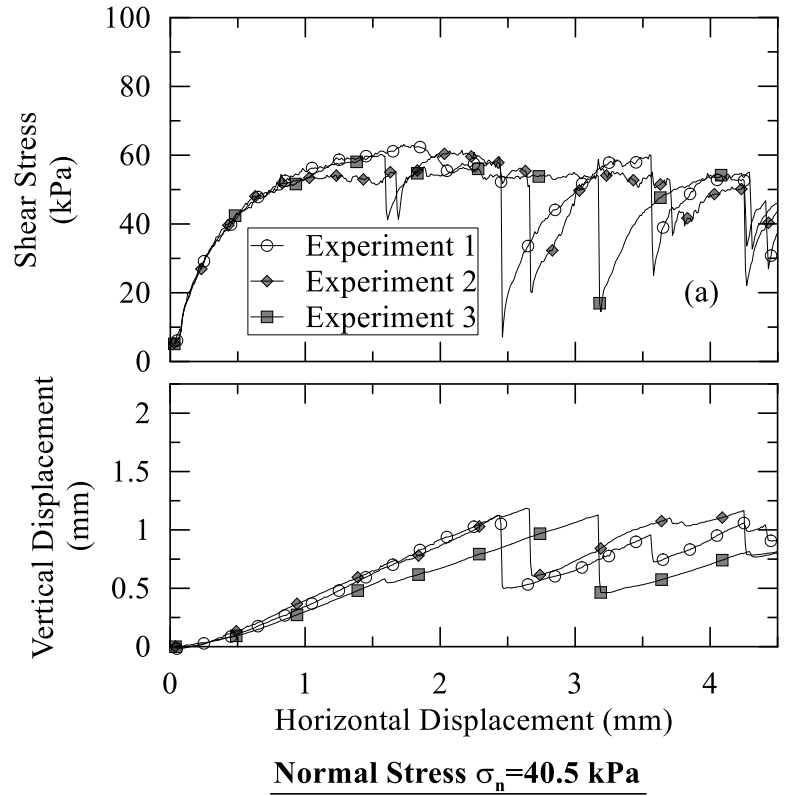
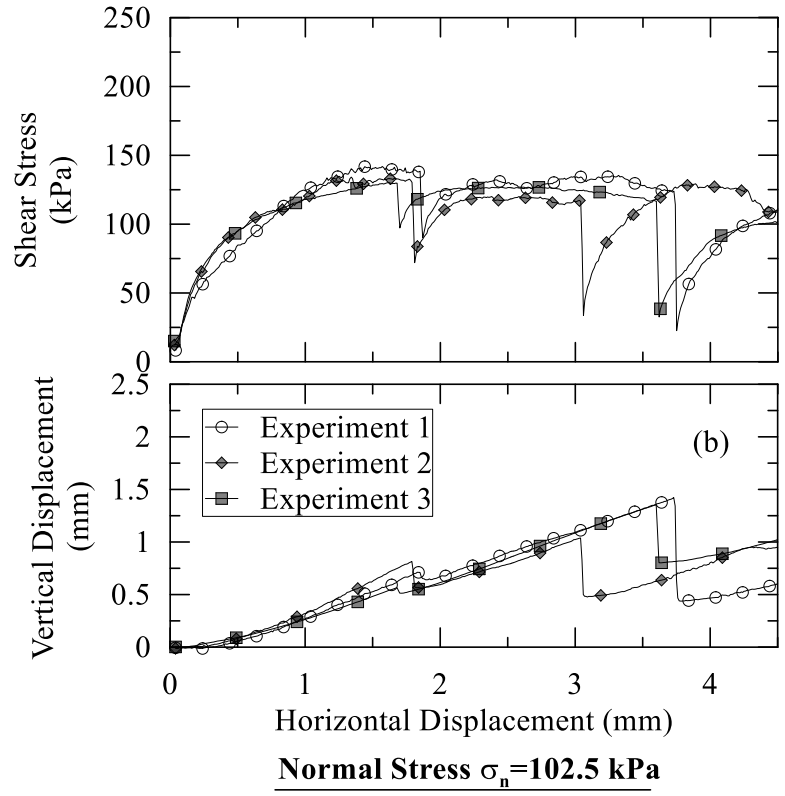
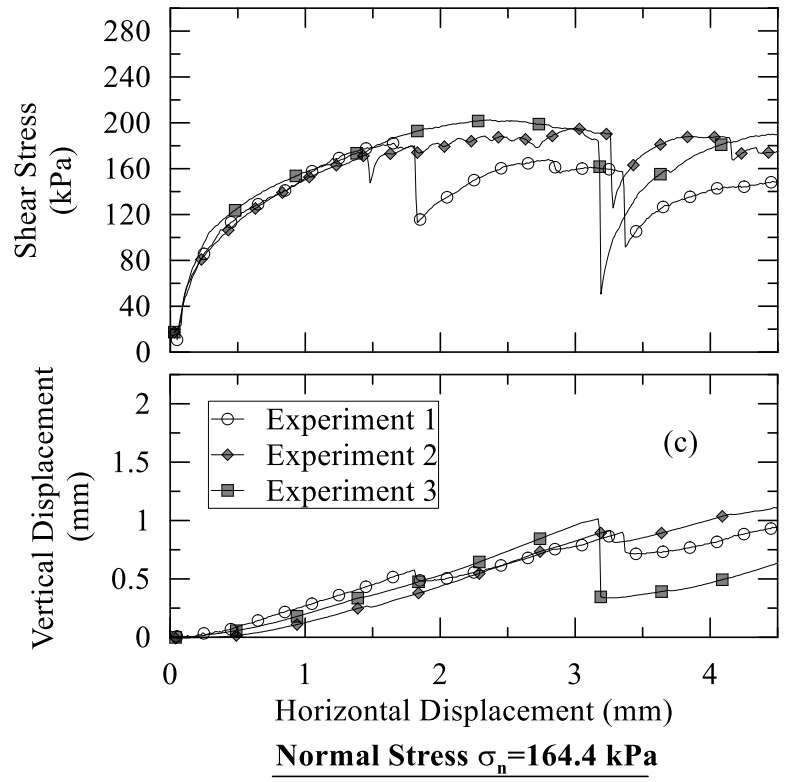


Figure B.3. Direct shear test results for particle 4-1.







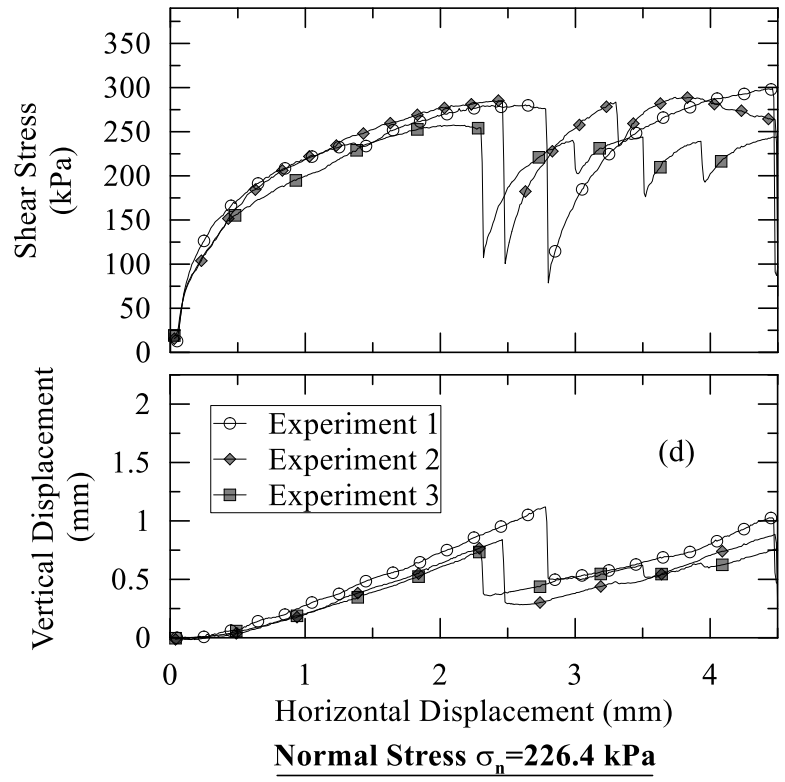


Figure B.4. Direct shear test results for particle 4-5.

**Appendix C – Limestone Particle 3D Scan Data**



Table C.1. Data for 60 particles SL scanned and 30 particles photogrammetry scanned.

Particle Number	Volume (V) (mm <sup>3</sup> )	SL Scanning		Photogrammetry	
		Surface Area (A) (mm <sup>2</sup> )	Size (L) (mm)	Surface Area (A) (mm <sup>2</sup> )	Size (L) (mm)
1	12603.3	3328.12	40.71	3149.64	40.28
2	20892.1	4643.45	54.37	4421.68	54.32
3	26555	5923.71	55.18	5298.34	54.45
4	19843.4	4508.16	50.94	4268.98	50.36
5	14158.5	3493.55	46.40	3397.63	46.47
6	14319.3	3535.13	43.64	3436.47	43.41
7	18801.1	4315.15	53.57	4195.39	53.66
8	11604.7	3196.94	44.98	3036.97	44.64
9	18709.6	4590.24	49.12	4389.98	49.04
10	11844.5	3060.13	42.67	3025.03	42.07
11	10871.4	2987.34	43.92	2968.41	45.47
12	14225.5	3615.68	42.59	3510.43	42.31
13	17489.7	4228.93	56.30	4156.05	56.66
14	13019.5	3337.45	42.31	3238.28	42.12
15	22581.2	5035.47	56.08	4896.54	55.63
16	8540.2	2512.12	39.68	2464.21	39.16
17	14068.6	3507.88	47.24	3448.09	46.65
18	11257.4	3043.69	40.56	2919.33	40.52
19	4030.3	1500.21	31.61	1441.90	31.42
20	3909.9	1542.7	30.11	1498.06	29.75
21	3368.4	1336.67	26.86	1299.73	26.46
22	4322.3	1548.09	30.31	1509.48	30.31
23	7704.3	2288.14	39.19	2218.34	39.09
24	8880.2	2578.11	36.16	2460.01	36.21
25	4609.1	1686.63	31.89	-	-
26	3380.3	1349.89	25.70	-	-
27	3910.3	1441.87	28.89	-	-
28	2826.5	1159.88	24.16	-	-
29	3846.7	1508.74	29.07	-	-
30	2909.3	1236.71	26.69	-	-

Table C.1. Data for 60 particles SL scanned and 30 particles photogrammetry scanned (Continued).

Particle Number	Volume (V) (mm <sup>3</sup> )	SL Scanning		Photogrammetry	
		Surface Area (A) (mm <sup>2</sup> )	Size (L) (mm)	Surface Area (A) (mm <sup>2</sup> )	Size (L) (mm)
31	2341.6	1091.12	25.08	-	-
32	5076.1	1739.03	29.27	-	-
33	2426.2	1114	27.94	-	-
34	3826.6	1482.6	27.94	-	-
35	3219.8	1301.67	27.31	-	-
36	2853.2	1189.22	29.02	-	-
37	3340.1	1377.34	30.31	-	-
38	23221.5	5015.71	48.93	-	-
39	13727.8	3403.72	41.71	-	-
40	7933	2505.49	41.15	-	-
41	4828.2	1759.89	38.61	-	-
42	2393.2	1085.33	28.52	-	-
43	3815.8	1405.32	26.76	-	-
44	2481.2	1080.94	27.00	-	-
45	2614	1123.28	25.15	-	-
46	1885	865.09	20.81	835.69	20.65
47	1969.1	909.88	23.26	864.55	23.22
48	2624.4	1072.79	22.95	1056.71	22.66
49	1902.4	931.63	23.79	915.57	23.64
50	1521.6	767.15	21.55	745.57	21.44
51	1632.6	828.24	24.29	812.80	24.81
52	1741.1	825.83	20.10	-	-
53	1882.4	914.85	22.30	-	-
54	1831.7	881.92	21.07	-	-
55	1375.3	705.44	19.26	-	-
56	1781.2	878.94	22.23	-	-
57	1016.5	591.44	18.82	-	-
58	1211.9	654.06	17.78	-	-
59	884.4	542.39	16.75	-	-
60	1176.3	648.02	18.57	-	-

Table C.2. Additionally sampled 8 particle SL scan data.

Particle Number	Volume (V) (mm <sup>3</sup> )	Surface Area (A) (mm <sup>2</sup> )	Size (L) (mm)
a	119.939	135.924	9.968
b	98.395	111.776	7.329
c	85.090	105.356	7.319
d	171.181	173.361	10.184
e	114.887	128.136	8.643
f	114.752	133.822	8.870
g	137.460	145.053	9.171
h	92488.695	12433.123	94.969

Table C.3. Particle Weight.

Particle Number	Weight (grams)
1	26.676
2	49.124
3	54.271
4	45.836
5	30.736
6	34.795
7	44.465
8	26.655
9	41.873
10	26.091
11	25.301
12	32.951
13	42.213
14	27.510
15	51.671
16	19.215
17	31.927
18	24.877
19	8.737
20	9.449
21	7.950
22	8.783
23	16.308
24	19.574
46	4.246
47	4.311
48	5.882
49	4.009
50	3.462
51	3.830

## VITA

### SUMANA BHATTACHARYA

2006-2010	B.E., Civil Engineering Jadavpur University, Kolkata, India
2013-2015	M. Tech., Civil Engineering National Institute of Technology, Rourkela, India
2015-2019	PhD, Civil Engineering Florida International University, Miami, Florida

### PUBLICATIONS AND PRESENTATIONS

- Lee, S. J., Lee, C.–H., Shin, M., *Bhattacharya, S.* & Su, Y.–F. (2019) “Influence of Coarse Aggregate Angularity on the Mechanical Performance of Cement-based Materials,” *Construction and Building Materials*, 204 (2019) 184-192
- Lee, S.J., *Bhattacharya, S.*, Lee, C. & Shin, M. (2019) “A New Interpretation of Three-Dimensional Particle Geometry: M-A-V-L,” ASCE EMI (Engineering Mechanics Institute) Conference 2019, Caltech, Pasadena, CA, June 18–21, 2019
- Lee S.J., Lee C., Shin M, *Bhattacharya S.* (2018) “Effect of Coarse Aggregate Morphology on Performance of Cement-based materials under cyclic loading” 11th US National Conference on Earthquake Engineering, Los Angeles, CA
- Lee, S. J., Shin, M., Lee, C. & *Bhattacharya, S.* (2018) “Morphology-driven Performance of Cemented Granular Materials,” ASCE EMI (Engineering Mechanics Institute) Conference 2018, MIT, Cambridge, MA, May 29– June 1, 2018
- Lee, S. J., *Bhattacharya, S.*, Shin, M., Lee, C. & Su, Y.–F. (2018) “Allometric Investigation of Granular Materials Behavior”, ASCE Engineering Mechanics Institute Conference 2018, MIT, Cambridge, MA, May 29–June 1
- Su, Y.–F., *Bhattacharya, S.*, Lee, C., Shin, M. & Lee, S. J. (2018) “Allometric Description of Granular Materials”, IS–Atlanta 2018: Geo–Mechanics from Micro to Macro in Research and Practice at *Georgia Tech*, Atlanta, GA, Sep. 9–12
- Lee, S. J., Lee, C., Shin, M. & *Bhattacharya, S.* (2018) “Microscopic Failure Mechanism of Cemented Granular Materials Driven by Particle Morphology”, IS–Atlanta 2018: Geo–Mechanics from Micro to Macro in Research and Practice, Georgia Tech, Atlanta on Sep. 9–12

- *Bhattacharya S.*, Lee SJ, Su Y-F, Lee C, Shin M (2018) “A New Particle Morphology Characterization to Account for Surface Angularity and Experimental Validation through 3D-Printing” 8<sup>th</sup> World Congress on Particle Technology, Orlando FL
- Zhang B, Lee SJ, Yu Q, Tutumleur E, *Bhattacharya S.* (2016) “Smartphone-Based Image Analysis Technique for Ballast Aggregate”. International Conference of Transportation and Development, Houston, Texas